Title
Controlling the Phase of Light by Nanostructuring of Materials

Author
Barth, David

Publication Date
2017

Peer reviewed|Thesis/dissertation

Controlling the Phase of Light by Nanostructuring of Materials

by

David Barth

A dissertation submitted in partial satisfaction of the

requirements for the degree of

Doctor of Philosophy

in

Engineering – Mechanical Engineering

in the

Graduate Division

of the

University of California, Berkeley

Committee in charge:

Professor Xiang Zhang, Chair
Professor Lydia Sohn
Professor Laura Waller

Summer 2017

Controlling the Phase of Light by Nanostructuring of Materials

Abstract

Controlling the Phase of Light by Nanostructuring of Materials

by

David Barth

Doctor of Philosophy in Engineering – Mechanical Engineering

University of California, Berkeley

Professor Xiang Zhang, Chair

The previous century was defined to a major extent by the digital revolution, which ushered in the information age. This rapid proliferation and improvement of electronic technology continues to have far-reaching effects on human existence. Similarly, advances in photonics have the potential to lead to technology that drastically changes our lives. So far, the vast potential of photonics, and especially nanophotonics, has not resulted in such sweeping societal change. While the laser, LED, and photovoltaic cell serve important, and increasing, functions, technological advances in photon control at the nanoscale are required for the full potential of photonics for computing, medicine, and energy to be realized. In this dissertation, we examine some methods and devices that can address these needs in photonics, particularly by exploiting the refractive index of materials, the phase of light, and the relation between the two.

The first chapter focuses on controlling the refractive index of silicon by inducing spatially varying porosity. This technique enables the fabrication of gradient index devices that can control light's propagation through the device to a degree that is not possible with traditional optical elements. By using the transformation optics design technique, it is possible to design a device with complete control over the path of light in the device, limited only by the material properties available. Using photoelectrochemical etching, we demonstrate the ability to control the refractive index of light in a range from 1.2 to 2.1 in devices that can be as large as centimeters, a combination not possible with other methods. This method is used to fabricate gradient index waveguides and Miñano concentrators, ideal optical concentrators, which are of particular interest in photovoltaics.

The next two chapters focus on using nonlinearity to manipulate light. First, the thermo-optic effect is used to design a dynamically self-assembled band structure in a distributed Bragg reflector, which exhibits reconfigurability of its transmission and reflection properties as well as self-healing to mitigate the effects of defects in the device structure. Next, a metasurface, a subwavelength array of resonant antennas is used to generate third harmonic frequency light and directly impart phase delays to it to control its reflection and refraction. Generalized laws of reflection and refraction for nonlinear harmonic generation at an interface

with phase discontinuities are developed and experimentally confirmed, and asymmetric transport, which is predicted by these laws, is demonstrated. Asymmetric transport is critical for the development of integrated photonics for computing applications.

In the final section, a technique for integrating quantum dots, nanoscale light sources, with other photonic components is demonstrated. The quantum dots are incorporated into electron beam resist materials in controlled concentrations and patterned with electron beam lithography, which can precisely control their location. Single quantum dots serve as non-classical emitters, capable of generating single photons necessary for quantum computing and many other emerging fields in quantum optics.

To my family

Contents

List of Figures

Acknowledgments

I would like first to thank my advisor, Professor Xiang Zhang, for his support of my research and education. He has honored me with his trust and encouraged my growth as a scholar with his creativity, passion for research, and deep insight into the important scientific challenges to be solved. He has assembled a group of outstanding scientists and engineers from all over the world and taught them to pool their intellectual resources to achieve unique results. I have benefited greatly from his strong emphasis on fundamental research through collaboration with the diverse experts that he has brought together.

I extend my thanks to Professors Lydia Sohn, Laura Waller, Tarek Zohdi, and Andrew Minor for their essential service on my qualification and dissertation committees as well as for their outstanding courses, which contributed greatly to my research. Professors Frank Fisher and Eui-Hyeok Yang, my undergraduate advisors at the Stevens Institute of Technology, helped me develop my interest in scientific research and encouraged me along this path, and I am thankful for their continued support and belief in me. Dr. Mario Zoccoli, in addition to being a great inspiration, has provided unwavering encouragement, optimism, and fascinating discussion.

I am very grateful to all of my collaborators, including Dr. Chris Gladden, whose mentorship greatly assisted my transition to graduate school, Dr. Alessandro Salandrino, Dr. Kevin O'Brien, Dr. Ziliang Ye, Dr. Michael Mrejen, Dr. Nir Shitrit, Dr. Jeongmin Kim, Dr. Chad Ropp, Dr. Nicolas Bachelard, Quanwei Li, and Dr. Carissa Eisler. I also want to thank Dr. Yuan Wang for his leadership and all of the postdoctoral fellows and graduate students of the group and the LMI EFRC, whose friendship, knowledge, and experience encouraged and assisted my own learning, especially Dr. Zi Jing Wong, Taiki Hatakeyama, and Mervin Zhao.

My parents, in addition to giving me life, love, and support, were also my editors, and it would be impossible to overstate my gratitude for everything they have done for me. My brother, my sister, and her husband have been unfailing in their support, encouragement, and example. Finally, and most importantly, my wife, Ellyn, is my greatest source of love, inspiration, and wise counsel. She brings out the best in me, and I am forever thankful to have her beside me as I continue this journey.

Chapter 1

Introduction

1.1 Nanotechnology and Nanophotonics

Since the invention of the transistor and the integrated circuit [1], nanotechnology has exploded as both a major driver of technological innovation and an area of vast scientific interest, leading to new understanding of the world around us. Similarly, advances in nanophotonics have also been critical to a variety of important technologies. Most visibly, the light emitting diode (LED), the semiconductor diode laser, and a variety of different photovoltaic cells have played an important role in industrial and societal development.

One of the early hopes of nanophotonics was that the miniaturization of optical components would allow photonic systems to replace or augment electronic ones at the chip scale [2]. Because photons are not charged, they interact with materials and with each other much less strongly than electrons. This can be both an advantage and disadvantage in designing photonic systems. This lack of interaction means that photonic systems suffer from less cross-talk and interference, can travel long distances with minimal losses. It also allows multiplexing, as photons of different wavelengths can use the same components and still be detected separately, enabling a powerful degree of freedom for design of such systems that is not available in electronics.

Despite the many advantages of optical systems over electronic ones, including multiplexing, higher speeds, and robustness to interference, they have not yet proven capable of replacing most electronic systems, especially at the chip scale. The main reason for this is also related to the weaker interactions of photons. Devices depend on these interactions to fulfill their function, and designing optical devices to meet all requirements of an integrated system has proven challenging. Plasmonics can help to alleviate this issue as well as spatially confine the light, an advantage to integration, but it also introduces losses, which can decrease efficiency and lead to problems in design [3]. In order for on-chip photonics to reach its envisioned potential, a toolkit of components including light emitters, photon control elements (e.g. modulators, multiplexers, waveguides, and filters) and photodetectors that can be integrated with electronic components is necessary. Much progress has been made

in recent years, but there is still much work to be done before we begin to see consumer products using these technologies [4–15].

1.2 Optical Fundamentals and Metamaterials

The primary focus of this dissertation is using metamaterials to control movement of light through materials by manipulating the light's phase. Light-matter interactions and their relation with phase and the refractive index can be understood through Maxwell's equations, the fundamental governing laws of classical electromagnetism [16].

$$\begin{aligned} \nabla \cdot \mathbf{D} &= \rho_f \\ \nabla \cdot \mathbf{B} &= 0 \\ \nabla \times \mathbf{E} &= -\frac{\partial \mathbf{B}}{\partial t} \\ \nabla \times \mathbf{H} &= \mathbf{J}_f + \frac{\partial \mathbf{D}}{\partial t} \end{aligned} \tag{1.1}$$

where $\mathbf{D}$ is the electric displacement field, ρ_f is the free charge density, $\mathbf{B}$ is the magnetic flux density, $\mathbf{E}$ is the electric field, $\mathbf{H}$ is the magnetic field, and $\mathbf{J}_f$ is the free current density.

If there is no free charge or current, we can apply several definitions and mathematical identities and arrive at the wave equations for the electric and magnetic field [17]:

$$\begin{aligned} \nabla^2 \mathbf{E} &= \mu_0 \varepsilon_0 \frac{\partial^2 \mathbf{E}}{dt^2} \\ \nabla^2 \mathbf{B} &= \mu_0 \varepsilon_0 \frac{\partial^2 \mathbf{B}}{dt^2} \end{aligned} \tag{1.2}$$

where μ_0 and ϵ_0 are the magnetic permeability and electric permittivity of free space respectively.

One solution to equation 1.2 takes the following form:

$$\begin{aligned} \mathbf{E}(\mathbf{r}, t) &= \mathbf{E}_0 \cos(\omega t - \mathbf{k} \cdot \mathbf{r} + \phi_0) \\ \mathbf{B}(\mathbf{r}, t) &= \mathbf{B}_0 \cos(\omega t - \mathbf{k} \cdot \mathbf{r} + \phi_0) \\ k = |\mathbf{k}| &= \frac{\omega n}{c} \end{aligned} \tag{1.3}$$

where $\mathbf{r}$ is the spatial coordinate, t is time, ω is the frequency, $\mathbf{k}$ is the wavevector, n is the refractive index, $n = \sqrt{\epsilon \mu}$, c is the speed of light, and ϕ_0 is the phase angle.

From equation 1.3 we can see that controlling the refractive index and directly imparting phase are two ways that light-matter interactions can be controlled. Phase and refractive

index are related by the concept of the optical path length ($OPL = \int n(s)ds$). Differences in OPL are directly related to phase differences between two light waves. Therefore, manipulating the refractive index of the medium through which a light wave travels to change its OPL is functionally the same as directly imparting the equivalent phase delay. This is illustrated in figure 1.1. Compared with the first case, where the light wave travels through a uniform medium, the other two situations result in phase shifts. In the second case the light enters a high index material and then exits it again. While it is in the high index material, the velocity decreases ($v = c/n$), so in order for the frequency to stay the same, the wavelength decreases. When it exits the high index material, the wavelength increases again, but the wave is now phase shifted from the wave in the uniform medium. In the third case, there is a phase discontinuity imparted to the light wave by a subwavelength element such as a metasurface, which we will discuss in chapter 4. In this case, the wavelength remains constant, but the discontinuity also results in a phase difference with the first wave.

Further understanding of the consequences of Maxwell's equations bring us to two more important concepts. The first is Fermat's principle of least time, whose modern version states that a ray of light follows a path such that an infinitesimal variation in the path yields an infinitesimal variation in the time for the ray to traverse it. Fermat's principle of least time can help us understand how light traverses materials with changing refractive index. Mathematically, this can be expressed by the eikonal equation, equation 1.4, derived from Maxwell's equations under a set of simplifications known as ray optics.

$$\frac{d}{ds}\left[n(\mathbf{r})\frac{d\mathbf{r}}{ds}\right] = \nabla n(\mathbf{r}) \tag{1.4}$$

where s is the parametric distance along the ray of light, and $\mathbf{r}$ is the vector describing the light ray's trajectory.

The other consequence of Maxwell's equations that will be important to understand this work is Fresnel's equations of reflection and refraction. These equations govern what happens at the interface between materials with different refractive indices, and are derived by applying the necessary boundary conditions for the electric and magnetic field at these interfaces. The effects of the boundary conditions change depending on the orientation of the electric field in relation to the interface of the two materials (called the light's polarization), so separate equations are derived for s-polarized light (named for the German word *senkrecht*, which means perpendicular), where the electric field is perpendicular to the plane of incidence, and p-polarized light, where the electric field is parallel to the plane of incidence. The Fresnel equations for s- and p-polarized light are given in equation 1.5 assuming the material is transparent and non-magnetic [18].

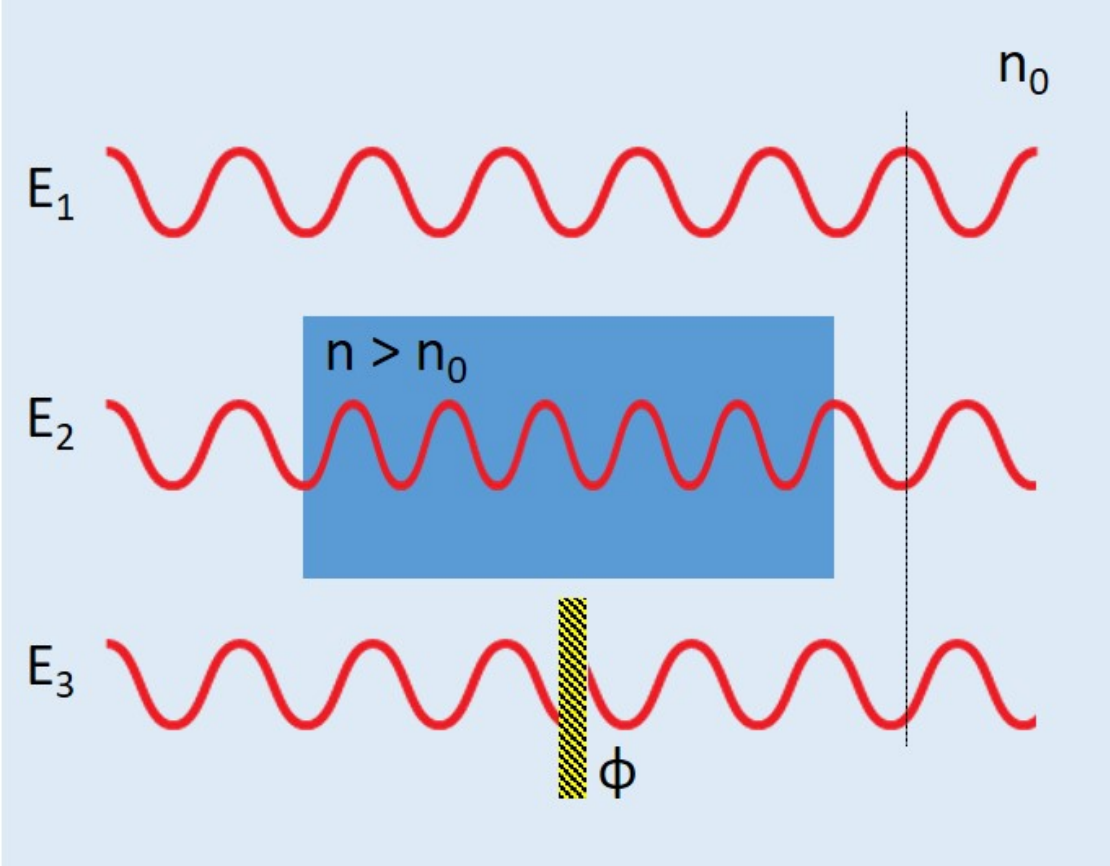

Figure 1.1: Illustration of light waves and how their phase can be affected. $\mathbf{E}_1$ travels through a single medium and is the reference for the other two cases. $\mathbf{E}_2$ enters a material with a higher refractive index and then exits it again. $\mathbf{E}_3$ passes through a thin subwavelength structure that imparts additional phase of ϕ to the wave. The dotted line shows that the final phase for each after traveling the same physical distance (but not the same OPL) is different for each wave.

$$R_s = \left| \frac{n_1 \cos\theta_i - n_2 \sqrt{1 - \left(\frac{n_1}{n_2}\sin\theta_i\right)^2}}{n_1 \cos\theta_i + n_2 \sqrt{1 - \left(\frac{n_1}{n_2}\sin\theta_i\right)^2}} \right|^2$$

$$R_p = \left| \frac{n_1 \sqrt{1 - \left(\frac{n_1}{n_2}\sin\theta_i\right)^2} - n_2 \cos\theta_i}{n_1 \sqrt{1 - \left(\frac{n_1}{n_2}\sin\theta_i\right)^2} + n_2 \cos\theta_i} \right|^2 \tag{1.5}$$

$$T_s = 1 - R_s$$

$$T_p = 1 - R_p$$

where R_s, R_p, T_s, and T_p are the reflectance and transmittance of s- and p- polarized light respectively, n_1 and n_2 are the refractive indices of the materials, and θ_i is the light's angle of incidence.

1.3 Objective

As we can see from these fundamental equations of optics, the refractive index, which is a material property that depends on the material's permittivity and permeability, is the key parameter affecting light-matter interaction. Much of metamaterials research focuses on manipulating these properties in ways that are not seen in nature, such as making both the permittivity and permeability negative, resulting in a negative refractive index [19]. Materials engineered in this way can also have a refractive index of 0, which leads to its own unique properties. Here we will define metamaterials functionally, but not rigorously, as materials whose nanoscale structure rather than atomic scale material properties, are responsible for their bulk properties. Some of the major achievements in metamaterials include negative refractive index materials [20–22] and super resolution imaging in the near [23, 24] and far field [25].

Recently, a large focus of metamaterials has been on dielectric metamaterials, which avoid the major problem of optical losses which the metamaterial field has struggled to mitigate, but which also lose some of the unique properties drew attention to them in the first place. Here, we will focus mainly on nanoscale engineering of standard dielectric materials, which have positive permittivity and permeability, and plasmonic materials, which have negative permittivity and positive permeability. The goal here is to use nanoscale engineering and the fabrication of metamaterials to make devices that control light in ways that are

difficult to achieve using conventional materials and techniques. The fabrication methods used are compatible with the ultimate goal of integrating nanoscale photonic components with electronic devices and fabrication methods.

In this work, we describe three methods of using nanomaterials in novel ways to control the movement and interaction of photons and one method of integrating nanoscale photon sources with convention nanoscale devices. The topics comprising this dissertation are outlined below:

- In chapter 2, we introduce *transformation optics*, a method that can be used to design optical devices that utilize gradients in refractive index, and *effective medium theory*, which allows us to estimate the bulk refractive index of composite materials whose components are much smaller than the wavelength of light, including porous materials, which are composites of air and solid material. We then introduce the technique of photoelectrochemical etching of silicon to fabricate porous silicon and silica with spatially controllable refractive index. We use this technique to fabricate a gradient index lens, an ideal optical concentrator, and a phase mask for imparting arbitrary phase to a light wave.

- In chapter 3, we design, simulate, and fabricate a distributed Bragg reflector and use the thermo-optic effect, a nonlinear process by which the refractive index of a material changes due to changes in its temperature, to cause the band structure of the Bragg reflector to exhibit properties of dynamic self-assembly. Dynamic self-assembly is a thermodynamically non-equilibrium process that allows devices to exhibit properties including reconfigurability and self-healing of defects.

- Chapter 4 covers the derivation of a generalized form of Snell's law of refraction that accounts for phase discontinuities introduced by an array of optical antenna called a metasurface, as well as nonlinear harmonic generation at the material interface. We fabricated a nonlinear metasurface that imparted a uniform phase gradient to the light wave while generating the third harmonic to the exciting frequency, and used this metasurface to confirm the derived equation. We tested and confirmed a major prediction of the equation, that certain polarizations of light could exhibit asymmetric transport through the metasurface.

- In chapter 5, we develop a method to incorporate luminescent quantum dots into standard fabrication processes by spin-coating and electron beam lithography. We control the location and density of quantum dots and isolate individual dots to detect single photons, which is necessary for quantum computing and other areas of quantum optics. This technique could be used to integrate photon sources with a variety of optical components including those discussed in previous chapters.

- Chapter 6 contains a summary of the works discussed and a brief discussion on future areas of research that build on the techniques and devices demonstrated as well as a broader outlook on the field.

Chapter 2

Gradient Index Optical Devices

2.1 Transformation Optics and Gradient Index Materials

Transformation optics [26, 27] provides a powerful tool for controlling electromagnetic fields and designing novel optical devices based on the form invariance of Maxwell's equations under coordinate transformations, meaning that changing the coordinate system does not change the form of Maxwell's equations, but only the constants [28]. As a result, we can understand the way light behaves in an artificially distorted space by applying a mathematical transformation that equates this distorted space to undistorted space with spatially varying optical properties, illustrated in figure 2.1. Figure 2.1a shows light propagation through untransformed space, and figure 2.1b shows the effect of the transformation on the behavior of light and the refractive index of the material. In this simple one dimensional example, the coordinates are quadratically compressed in the x direction, meaning the light rays traversing the space bend more than they would in uncompressed space. It can be helpful to imagine the coordinate space and the light rays drawn on a sheet of rubber. As the rubber is stretched and compressed, the light rays bend, because they are fixed to the coordinate system. The mathematical transformation then allows the material properties of the physical medium required for the light to behave as though they were in the virtual deformed space. The application of this method allows the design of many novel and potentially useful devices including perfect lenses, which have imaging resolution better than the diffraction limit, [29] and invisibility cloaks [30, 31].

In practice, devices designed by this method often require material optical properties that cannot be achieved at visible or near IR light wavelengths. In particular, transformation optics can result in device designs that require the relative magnetic permeability, μ, to have a value other than 1. Since no natural materials exhibit a magnetic response at optical wavelengths, this requires the use of specially designed resonant metamaterials such as split ring resonators. These devices are both difficult to fabricate and impractical due to large optical loss. The conformal transformation technique [32–34] can relax this requirement to

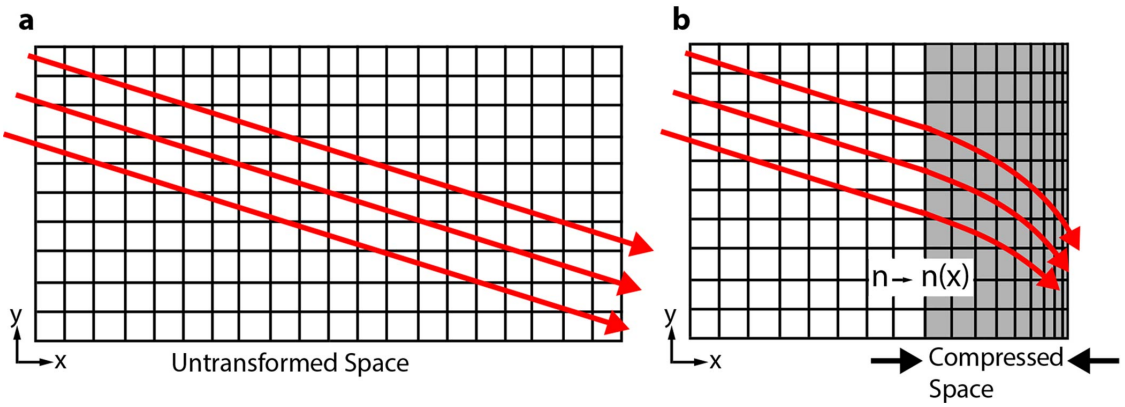

Figure 2.1: A simple 1D transformation, which gives the optical properties required for light in real space to behave as designed in transformed space. a) Light propagation through untransformed space. b) Light propagation through transformed space.

isotropic dielectrics with gradient refractive indices, which means resonant metamaterials are not necessary. However, there are few effective methods for achieving large arbitrary refractive index gradients at large scales, so the limitation for building transformation optical devices is still in the fabrication. Nanofabrication techniques such as electron beam lithography or focused ion beam milling have been demonstrated to achieve large control of refractive indices for a carpet cloak [35–39], a multifunctional optical Janus device [40], and a Luneburg lens [41, 42], but those devices are limited to small sizes on the order of hundreds of micrometers and are very expensive and time consuming to produce. These fabrication techniques are intrinsically unscalable to volume production or macro scale devices. Because they are serial "writing" type fabrication methods, the writing speed is the major limiting factor in the throughput. The speed varies based on the exact requirements of a process, but speeds on the order of tens of seconds per square μm are typical. Also, because these methods require a beam of charged particles focused to the nanometer scale, the total field size is restricted by the ability to keep the beam in focus, and even in the most advanced tools, is only on the millimeter scale.

For large scale optical devices, standard fabrication techniques do not allow engineered refractive index profiles to be patterned into optical media with the precision and range required for transformation optics. Doped glasses, the current industry standard engineered materials for gradient index optics, are limited to relatively modest gradients and variations as well as restricted geometries [43, 44]. The reported maximum index variation is 0.27, and is more commonly 0.1 or less [45, 46]. Recent work shows that similar flexibility and large scale patterning can be achieved using photopolymers. However, they are limited to a refractive index variation of less than 0.003 [47], which is three orders of magnitude smaller than we demonstrate. Similar capabilities have also been demonstrated using interference lithography [48] and direct laser writing [49], but these are also limited to smaller refractive index variations, as they ultimately control refractive index by exposing photosensitive

polymers.

Effective Medium Theory

Bulk material properties can be controlled through the nanostructure of materials according to effective medium theory, whose basic concept is that the an inhomogeneous material's bulk properties are some average of the properties of the homogeneous components. Although it is not yet possible to predict the exact values of these bulk properties, effective medium theory allows us to develop approximations that are useful for the design of such materials. The exact calculation of effective properties is less important than the concept that we can use nanoscale structuring to control bulk properties.

For optics in particular, it may seem counterintuitive that features at length scales far smaller than the diffraction limit can affect the light-matter interactions, but in fact, this size difference is critical. Because the inhomogeneity is an order of magnitude or more smaller than the wavelength of the light interacting with it, the light cannot "see" and interact with the individual components. Instead the material affects the light as though it were a homogeneous material with the average properties defined by the effective medium. This is how, for instance, engineered materials can achieve a negative refractive index by combining two different nanoscale building blocks, one with negative permittivity, and the other with negative permeability, both of which do occur naturally. As long as, in the effective medium, the negative value from one component is stronger than the positive value from the other, the bulk material will exhibit both negative permittivity and permeability. A simpler form of metamaterial enabled by effective media is a porous dielectric. If the pores are much smaller than the wavelength of light, the composite of air and the material will behave as an effective medium with an index between the two. By spatially controlling the porosity, the refractive index can also be spatially controlled within a material, thus allowing the design of devices with refractive index gradients, which can be used to produce a variety of useful effects.

There are many effective medium approximations, varying from theoretical upper and lower bounds with very few assumptions to empirical formulas for specific types of composites. The Hashin-Shtrikman bounds, which have been derived for a broad range of material properties, including refractive index, are the tightest bounds possible on the effective properties of a two-phase material, assuming only that the two component materials are isotropic and isotropically distributed. One useful model for predicting the refractive index of porous materials is the Maxwell-Garnett theory. Figure 2.2 shows the effective permittivity of a composite as calculated by the Hashin-Shtrickman bounds and the Maxwell-Garnett theory as a function of the porosity of the composite. In this case, because the permeability of most materials at optical frequencies is 1, the refractive index is related to the permittivity by $n = \sqrt{\varepsilon}$.

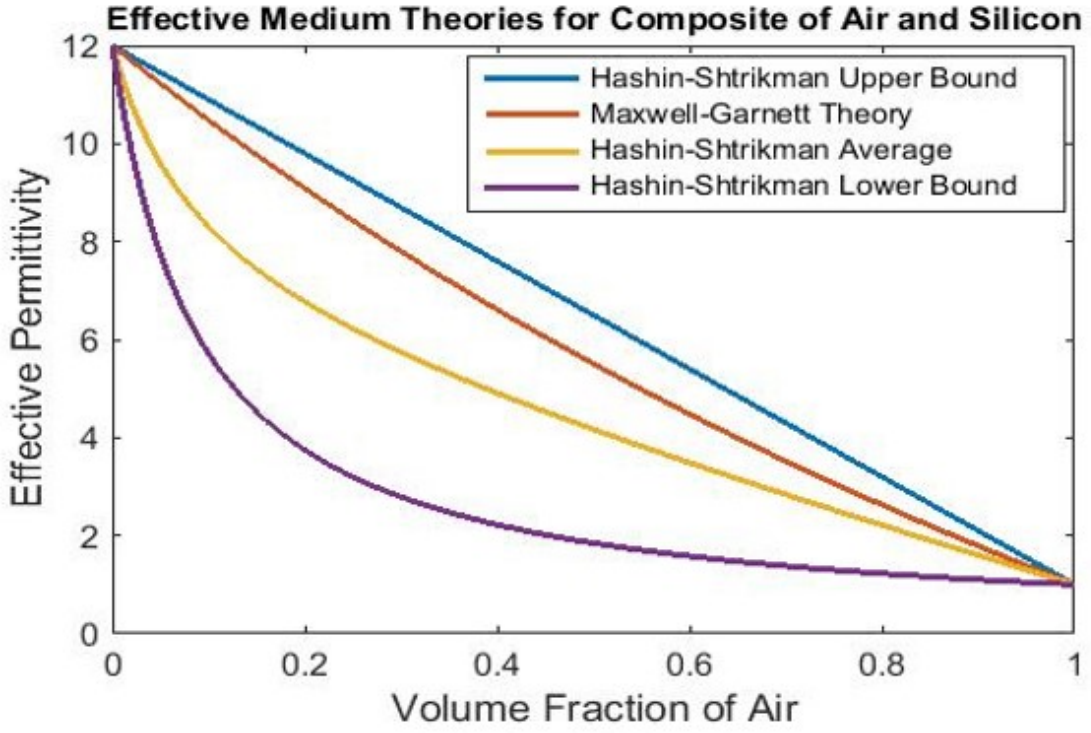

Figure 2.2: Effective medium approximations to estimate refractive index of composites of air and silicon. Hashin-Shtrikman upper and lower bounds, the tightest theoretical bounds on the effective properties, are shown, along with the average of the Hashin-Shtrickman bounds, which is often used as a rough estimate for the actual value. A more specific model, the Maxwell-Garnett theory is also shown. The Maxwell-Garnett theory is used here to approximate the porosity of samples from their measured refractive index.

2.2 Electrochemical Etching

Porous silicon produced by electrochemical etching [50, 51] can have a large variation of refractive index achieved by forming an effective medium with a network of nanoscale pores [52]. The density of the pores and thus the effective refractive index can be controlled by changing etching conditions. The etching process can be considered a two step electrochemical reaction, where silicon is first electrochemically oxidized and the oxidized silicon is then chemically dissolved by hydrofluoric acid, as shown in equation 2.1.

$$\begin{aligned} Si + 2H_2O + 2h^+ &\rightarrow SiO_2 + H_2 + 2H^+ \\ SiO_2 + 6HF &\rightarrow SiF_6^{2-} + 2H_2O + 2H^+ \end{aligned} \tag{2.1}$$

Bragg mirrors and other one dimensional multilayer optical devices with index variations in the perpendicular direction (z direction) have been demonstrated in porous silicon by peri-

odically adjusting the etching current with time [53–55]. In these devices the etch conditions vary during the etching process, and as a result, the refractive index in the z-direction can be controlled. This technique is effective as an alternative to optical thin film deposition, but in order to extend this technique to two-dimensional devices it is necessary to impose lateral (x-y plane) gradients. This has been demonstrated by using electrodes designed to shape the electric field in the electrochemical cell during etching [56]. However, the refractive index profile is determined by the designed electrode, which limits the flexibility of the technique, as each different design will require a new, precisely machined electrode. This technique has only been used for simple, symmetric index patterns. For more complicated devices, electrode design would be difficult.

Another recent work used deep reactive ion etching (DRIE) to prepattern silicon before electrochemical etching and selective-area ion doping to passivate certain surfaces of the prepatterned structures, which helped control the pore direction and minimize internal interfaces between pores forming in different directions [57]. This allowed the fabrication of devices such as birefringent microlens arrays. This interesting technique could be complementary to the photoelectrochemical etching method described in this chapter, as it has superior spatial resolution, but is limited by symmetry requirements in the index pattern.

2.3 Photoelectrochemical Etching

Photoelectrochemical (PEC) silicon etching is a technique that provides a practical and effective way to fully control the macro scale profiles of refractive indices by structuring the porous silicon on the nanoscale. We demonstrate continuous index variation from n = 1.1 to 2, a range sufficient for many transformation optical devices [58].

Our PEC etching is a flexible and powerful method for fabrication of porous silicon that uses light projected onto the surface of the silicon, rather than modulation of current density during the etching, to spatially control the material properties [59, 60]. This process depends directly on the charge carrier concentration in the material. The light absorbed at the surface of the silicon locally modulates the carrier density distribution in the silicon, which affects the pore formation rate and thus the effective refractive index.

The PEC silicon etching process is sensitive to illumination as well as to dopant type and concentration. The chemical reaction requires the presence of holes, so n-type silicon does not etch in the dark, requiring illumination to generate the necessary holes. The required illumination and sensitivity to illumination intensity permits optical control of etching in n-type porous silicon. However, n-type porous silicon tends to have high scattering, non-uniform pore size, and strong photoluminescence, making it a poor material for optical devices. P-type silicon, because of the abundance of holes, etches well in the dark and is typically much more sensitive to current density during the etch process than to illumination. The resulting structure has more uniform pores and is more optically transparent than n-type porous silicon, making it suitable for one dimensional optical devices [61, 62], with etch depths on the scale of the wafer thickness. However, optical patterning has not previously

been demonstrated in p-type silicon, making the fabrication of two or three dimensional devices difficult.

This work is, to our knowledge, the first time light has been used to control porosity in p-type silicon. As a demonstration, we fabricated in-plane gradient index devices using our PEC etching method. Figure 2.3 illustrates the chemistry of the PEC method and electron micrographs of the resulting structures. The applied current in the electrochemical cell causes holes to drift toward the surface of the silicon, while electrons drift in the opposite direction. When two holes react with a surface silicon atom, the atom becomes oxidized, and can be dissolved by hydrofluoric acid (HF). As pores form, it becomes unlikely for holes to diffuse all the way to the external silicon surface, so etching is restricted to the interface between the porous and bulk silicon. When light is absorbed by the silicon, an exciton, an electron-hole pair, forms near the surface. For low intensity illumination, the number of charge carriers generated by light absorption is not large enough to significantly affect the electrochemical reaction. However, when the light intensity becomes strong enough, the charge carrier density due to photoexcitation can approach or exceed the carrier density due to the doping. This can change the effect of the doping, which is one of the most important parameters affecting porous silicon formation. This results in p-doped silicon behaving as though it were less heavily doped as illumination increases, which inhibits etching. The balance of charge carriers controls pore formation, resulting in lower porosity and therefore higher refractive index in more strongly illuminated areas. Using a low etching current and high illumination intensity, we increase the influence of illumination on the etching process, allowing us to spatially control the porosity using light. The opposite effect is seen in n-type silicon, where absorbed light provides the necessary holes and enables etching.

This process allows us to pattern the porosity of the p-type silicon by projecting an image on the surface of the silicon using a digital micromirror device (DMD) during the etching process. Any grayscale image can thus be projected onto the chip during etching, meaning there is no symmetry requirement. Any arbitrary pattern can be etched. This new technique unlocks extreme flexibility in gradient index pattern control for making transformation optical devices. While we did not explore the limits of patterning resolution in this work, we were able to demonstrate patterned features smaller than 1 mm. The ultimate resolution is likely not caused by the diffraction limit of the optical system used to project the pattern, but the diffusion length of photogenerated charge carriers in the silicon, which is on the order of tens of micrometers [59].

PEC Process

A silicon chip approximately 2.5 cm^2 was placed in a custom-built Teflon electrochemical cell in contact with an aluminum bottom electrode. The cell was then filled with 6.5 mL of electrolyte, prepared with 1 part 49% HF solution to 3 parts ethanol by volume. The top electrode, a ring of platinum wire, was placed in the cell so it was just covered by the electrolyte. An illumination pattern was then projected onto the chip using a DMD projector and 3 lenses to focus and resize the image to 2 cm^2. The optical power density

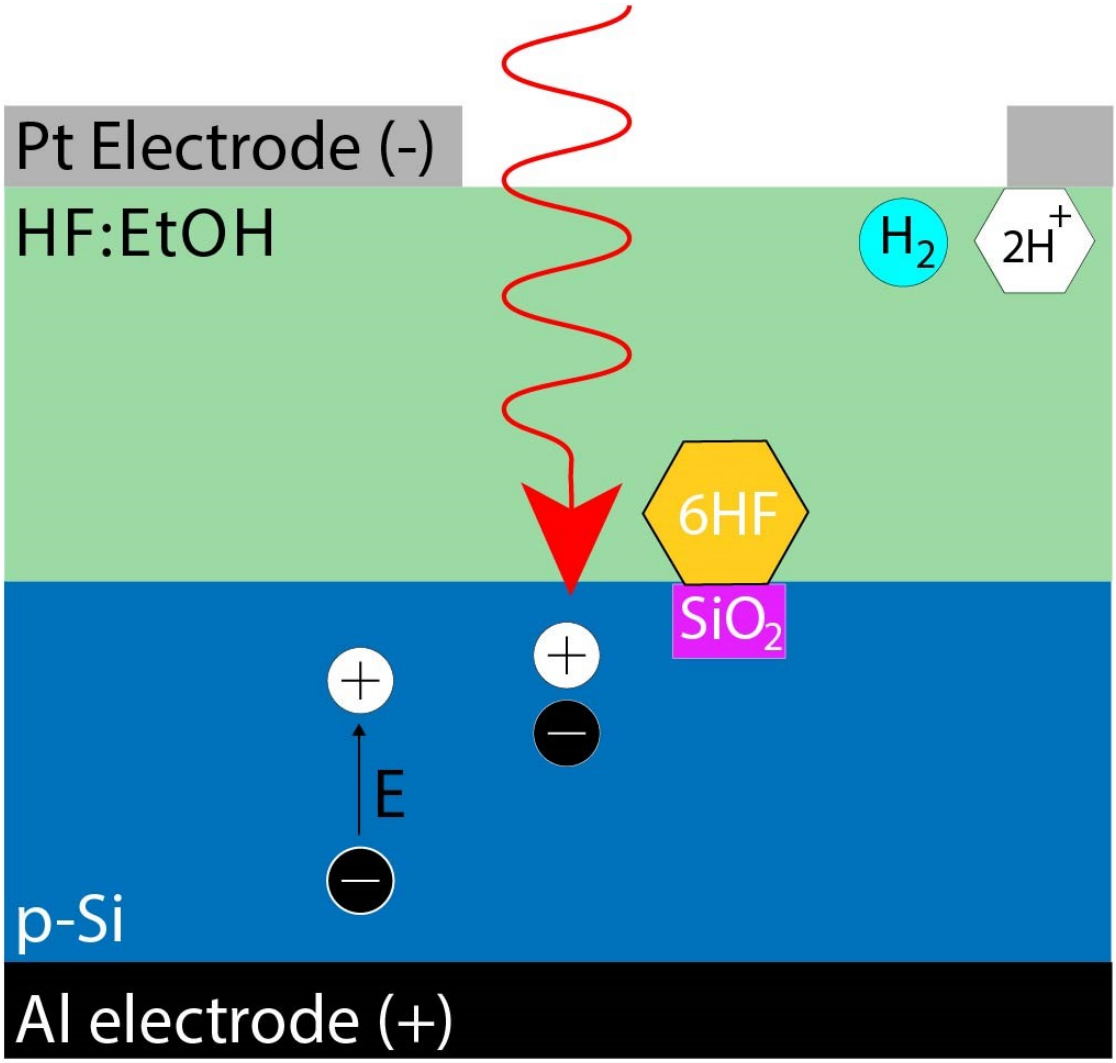

Figure 2.3: PEC etching for p-type porous silicon. Electrochemical dissolution of silicon in HF and the effect of optical excitation are shown.

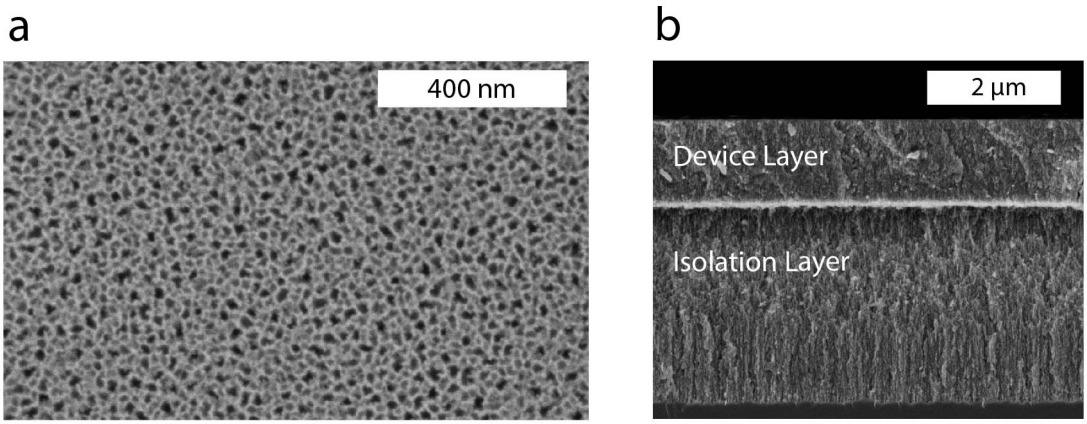

Figure 2.4: SEM micrographs of gradient index porous silicon device. a) Top view. b) cross-sectional view showing high index device layer and low index isolation layer.

of the projected light ranged from 50 W/m^2 to 5500 W/m^2. A constant current of 10 mA was applied for four minutes, resulting in a constant etching rate of approximately 0.35 μm/minute. The effect of illumination and etch depth on etch rate was minimal. The pores are approximately cylindrical, and the pore diameters range from approximately 10 to 30 nm. The pore length is equivalent to the etching depth. Figure 2.4a shows the scanning electron micrograph of top view of the fabricated porous silicon. To access a lower index range, some porous silicon samples were then placed in a rapid thermal annealer under 15 μmol/s oxygen gas at 300° C for 5 minutes and then at 800° C for 8 minutes to form porous silicon oxide.

In order to make a waveguide, with light traveling in a high index medium between two lower index materials, an additional etching step was required. Because porous silicon has a lower index than bulk silicon, a layer of porous silicon on top of bulk silicon will not confine light. The material underneath the gradient index material must have a lower index. In this etching process, the etching occurs from the interface between silicon and electrolyte. Unlike in typical thin film deposition in which subsequent layers deposit on top of previous ones, the first etched layer is on top and subsequent etching proceeds downwards as etching always occurs at the interface beween the porous and bulk silicon without affecting previously etched porous silicon. This occurs because once the material is etched and becomes porous, it will no longer react due to the increased electrical resistance of the porous layer, which inhibits the electrochemical etching process. The top to bottom nature of this etching process allows us to form an isolation layer by performing a second electrochemical etch before removing the wafer from the electrochemical cell. For this step, the current was increased to 50 mA and a cover was placed on the cell to keep it in the dark. The sample was etched for an additional four minutes. The higher current resulted in a layer of porous silicon with a larger average pore size and thus a lower effective refractive index below the device layer. The isolation

layer below and air above form a complete waveguide. Figure 2.4b shows the layers of the waveguide in cross section. The top layer contains the gradient index device, which is 1.4 μm thick. The next layer is the low index isolation layer with a refractive index of 1.2, which is 3.0 μm thick. Below the isolation layer is the bulk silicon substrate, approximately 500 μm thick.

Refractive Index Characterization

The refractive index of the resulting film was characterized by Fourier transform IR (FTIR) reflectance interferometry. The spectral reflectance of the porous silicon film on top was measured. Due to interference between light reflected from the top and bottom surface of the porous silicon, the reflectance spectrum has sinusoidal interference fringes. These fringes are used to calculate the refractive index. The film thickness was measured manually by cross-sectioning the sample and imaging in SEM. By calculating the reflectance of films of that thickness while varying the refractive index and optical absorption, the FTIR spectrum could be fitted to a theoretical curve and optimized to determine the index of the film as well as its optical absorption.

We demonstrate the ability to spatially vary the effective refractive index of porous silicon between 1.4 and 2.0, shown in Figure 2.6, at near infrared wavelengths by projecting a spatially varied light intensity pattern onto the surface of the silicon in the electrochemical cell. Increasing illumination intensity inhibits pore formation, resulting in a less porous material and a higher effective refractive index. The device can then be thermally oxidized, converting the structure to SiO_2, reducing the index and allowing the device design to extend to visible wavelengths of light. After oxidation, the refractive index ranges between about 1.1 and 1.4. Figure 2.6a shows the refractive index of porous silicon and porous silicon oxide as a function of illumination intensity. The intensity values correspond to the position along the x direction of the sample shown in Figure 2.6b, on which a linear gradient was etched in order to measure the refractive index for different illumination intensities.

Index measurements were performed in a wavelength range from 1.2 to 2.3 μm. The index variation due to material dispersion across this range is about 0.04, small enough to allow broadband devices to be designed in the near IR. The graph in figure 2.6a shows the average index across this wavelength range for each point. The wavelength dependent index variation is far smaller than the index variation due to the porosity gradient in the material, so it is acceptable to use this as the approximate index for the whole wavelength range. This range of achievable refractive index variation is sufficient for many transformation optical devices. For example, for the Luneberg lens, the required relative refractive index range is from 1 to 1.41. The required refractive index for carpet cloaks depends on the design, but a larger refractive index gradient allows a larger feature to be cloaked in a smaller total cloak area.

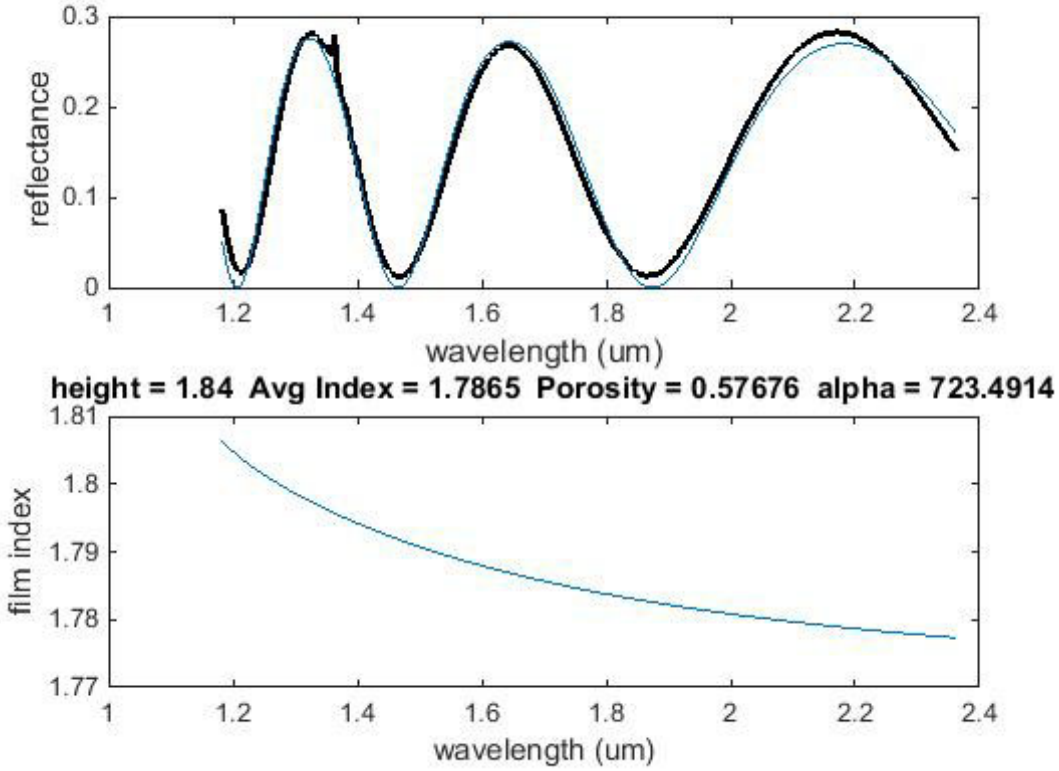

Figure 2.5: FTIR reflectance spectrum for a porous silicon thin film. The thick black line is the measured reflectance, and the thin blue line is the theoretical fit. Maxwell-Garnett effective medium theory is used to calculate the porosity based on the index. The lower graph shows the dispersion of the refractive index, calculated using silicon's dispersion and the Maxwell-Garnett theory.

2.4 Gradient Index Lens

As an example, we used this PEC etching technique to demonstrate a gradient index parabolic lens with the refractive index $n = n_0\left(1-k\frac{r^2}{2}\right)$ where n_0 is the base index at the center of the lens and k the gradient constant. In order to couple light into and out of the waveguide, electron beam lithography followed by dry etching with carbon tetrafluoride (CF_4) gas was used to fabricate gratings directly in the porous silicon. The gratings consist of ten periods of 1 μm each with a depth of approximately 500 nm, and were optimized for a light wavelength of 1.5 μm. SEM micrographs of the gratings are shown in figure 2.7, and figure 2.8 illustrates each step of this fabrication process.

To observe light propagation through the waveguide, a supercontinuum light source (Fianium, Southampton, UK) was focused on the input grating to couple broadband IR light

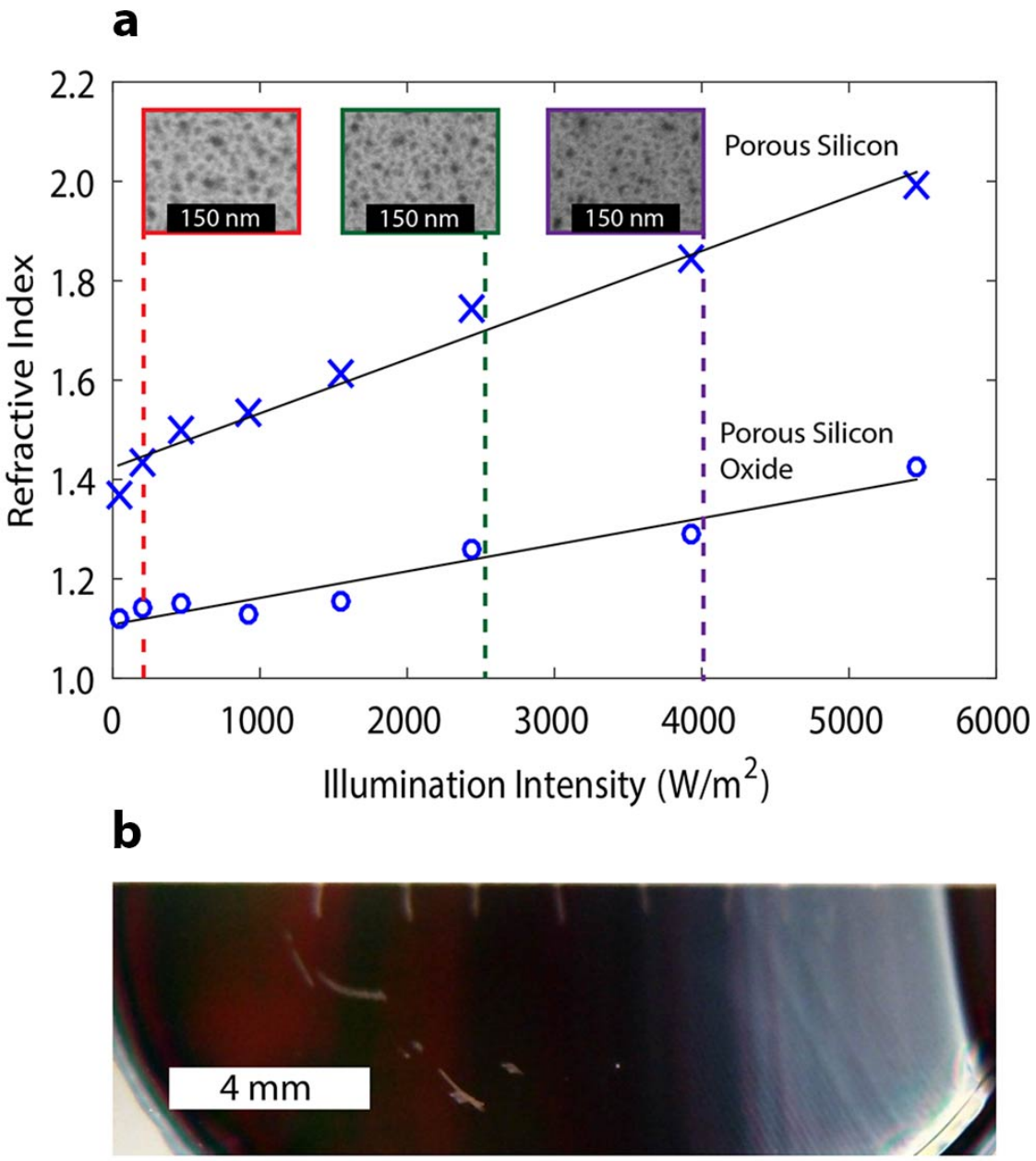

Figure 2.6: The effective refractive index of porous silicon. A smooth gradient in refractive index can be achieved over an index range of 1.4 to 2.0 for porous silicon and 1.1 to 1.4 for porous silicon oxide. a) Refractive index distribution as a function of light intensity projected during etching. Lower curve shows refractive index of the same material after oxidation by rapid thermal annealing. The insets are scanning electron micrographs of the porous silicon at illumination intensity 200 W/m2, 2500 W/m2, and 4000 W/m2, respectively. b) Porous silicon sample with a smooth gradient for index measurement.

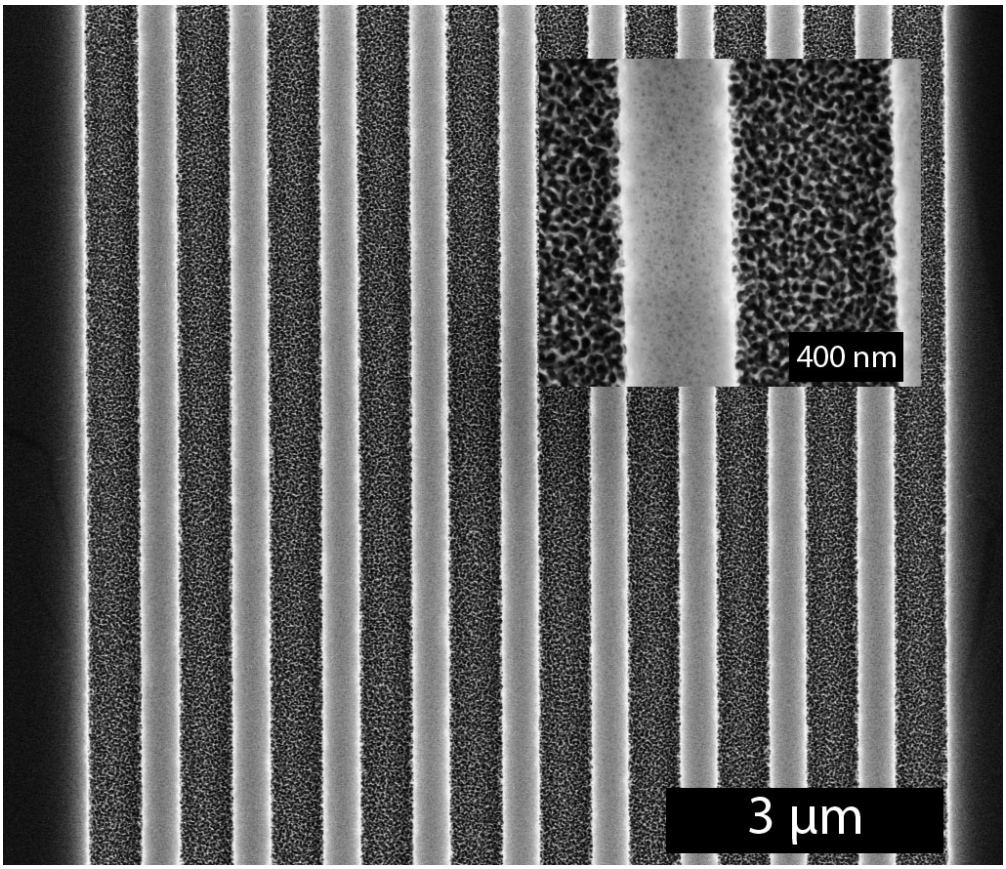

Figure 2.7: SEM micrograph of gratings etched into porous silicon gradient index lens. Ten grating periods were etched with each period 1 μm. Increasing the number of periods increases the coupling efficiency but also decreases their operating bandwidth, which is a disadvantage in a broadband device. Inset shows a magnified image of a single period of gratings.

into the device, and the device was imaged with an infrared charge-coupled device (CCD) as shown in figure 2.9. The sample was attached to a micrometer stage, which was translated to move the laser spot along the grating. We observed light scattered from within the waveguide as well as light coupling out from the gratings to determine the propagation path of light in the device. Light propagation through the devices was simulated using a custom ray tracing program written in Mathematica, which used a form of the eikonal equation to determine optical paths within the device. The simulation, matching a well-known result in gradient index optics, shows that light inside the parabolic gradient index waveguide follows a sinusoidal pattern.

Figure 2.11 shows a device designed to contain one half period of the sinusoidal oscillation. A half period lens images an object from its front surface to its back surface with a magnification of -1, meaning that a focused spot on the left side of the lens above the lens's

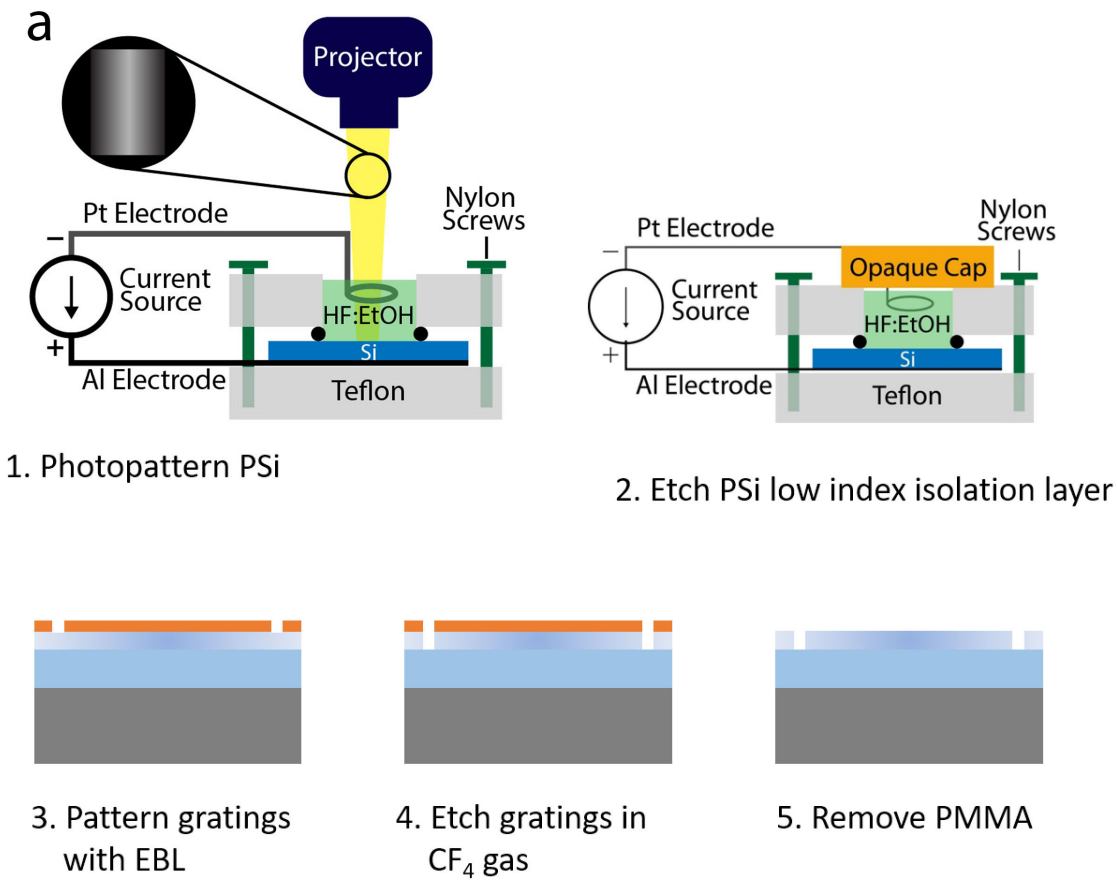

Figure 2.8: Device fabrication by PEC etching. a) Process steps showing optical control of refractive index, etching of isolation layer, and fabrication of coupling gratings. b) Photograph of gradient index waveguide fabricated by this process.

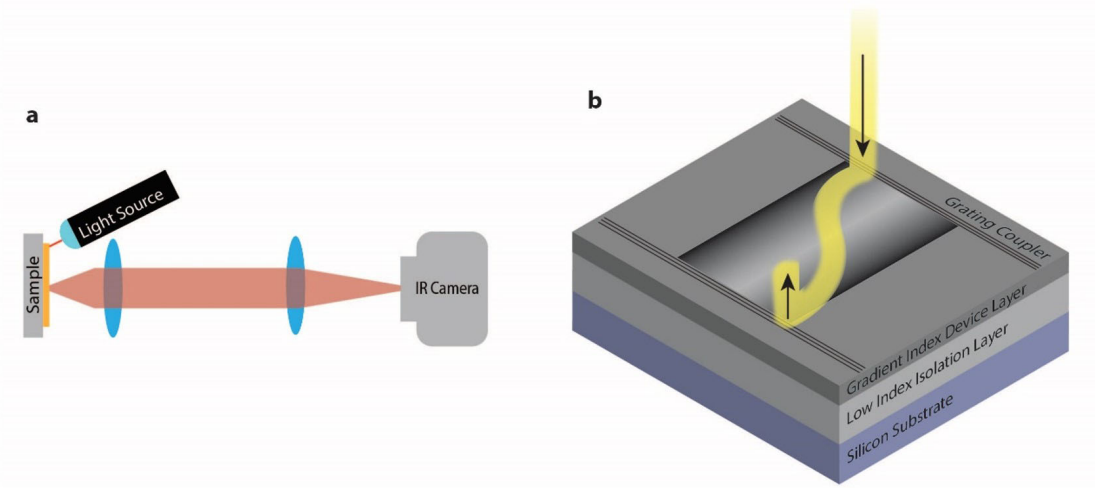

Figure 2.9: Schematic of the setup for measuring light propagation through a gradient index lens. a) 4f system for imaging propagation of light through porous silicon gradient index lens samples. b) Schematic of gradient index lens sample showing light bending as it passes through the device.

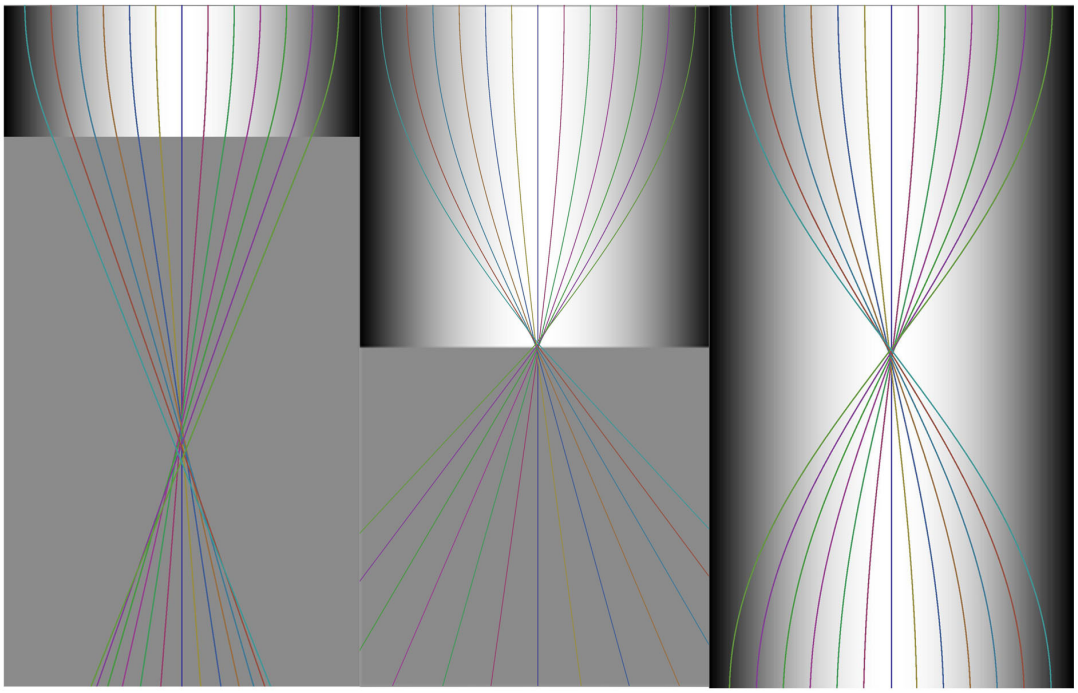

Figure 2.10: Ray traces for parabolic lenses with the same index gradient and three different thicknesses. (Left) Thin lens. (Center) Quarter-period lens. (Right) Half-period lens.

axis is imaged to a point of identical size on the right side mirrored about the axis, so the spot appears below the axis as illustrated in figure 2.11. From the period of the sinusoidal pattern, $\Lambda = 12.3$ mm, we can calculate the gradient constant $k = \left(\frac{2\pi}{\Lambda}\right)^2 = 0.26$. This agrees with the theoretical value of k from the design of the lens, which is 0.27. We also designed and fabricated waveguides of one quarter period and one eighth period with the same refractive index gradient. The focal lengths of all of these devices match closely with the predictions of the ray tracing model.

2.5 Optical Concentration with Porous Silicon

Optical Concentration for Photovoltaics

As solar energy becomes increasingly important in the global energy economy, new ways to increase photovoltaic (PV) efficiency and decrease cost are needed. Concentrator photovoltaics (CPV) is one such strategy. By using optics to concentrate sunlight to a small area, the PV efficiency can increase, and the module cost decreases, as the amount of material required for the solar cell is much less. Lenses and mirrors are commonly used to direct light onto these smaller solar cells, but these have inherent disadvantages in efficiency that cause additional losses, resulting in decreased PV module efficiency. Nonimaging optics can overcome these problems by designing optical elements that only transfer light from the one place to another and do not form an image of the source. The Miñano design method is one technique for designing nonimaging optical devices. Unlike other methods, it can be used to design gradient index optics, allowing greater design flexibility. The Miñano concentrator, an ideal concentrator designed using this method, can be fabricated with a much smaller aspect ratio compared with traditional ideal concentrators by increasing the index gradient of the device.

Porous Silicon Miñano Concentrators

Although the Miñano method allows the design of many useful gradient index optical devices including the Miñano concentrator, the difficulty in fabricating gradient index materials means that the method has so far seen limited use. Porous silicon, with its easy fabrication and large index contrast, is a promising material for the realization of these devices.

Miñano concentrators with aspect ratios of 2 and geometric concentration ratios ranging from 3 to 100 were fabricated using the PEC etching method described previously. Due to fabrication challenges, the devices do not have perfectly reflective sidewalls as the design requires. Instead, the outside of the device consists of low index porous silicon in order to maximize reflectivity due to total internal reflection. The optical performance of fabricated devices was compared with a slab waveguide. The concentrator should show a much smaller output aperture than the waveguide, higher peak intensity, and the same integrated intensity. Some concentration is clearly visible but is confounded by high scattering losses in the optical

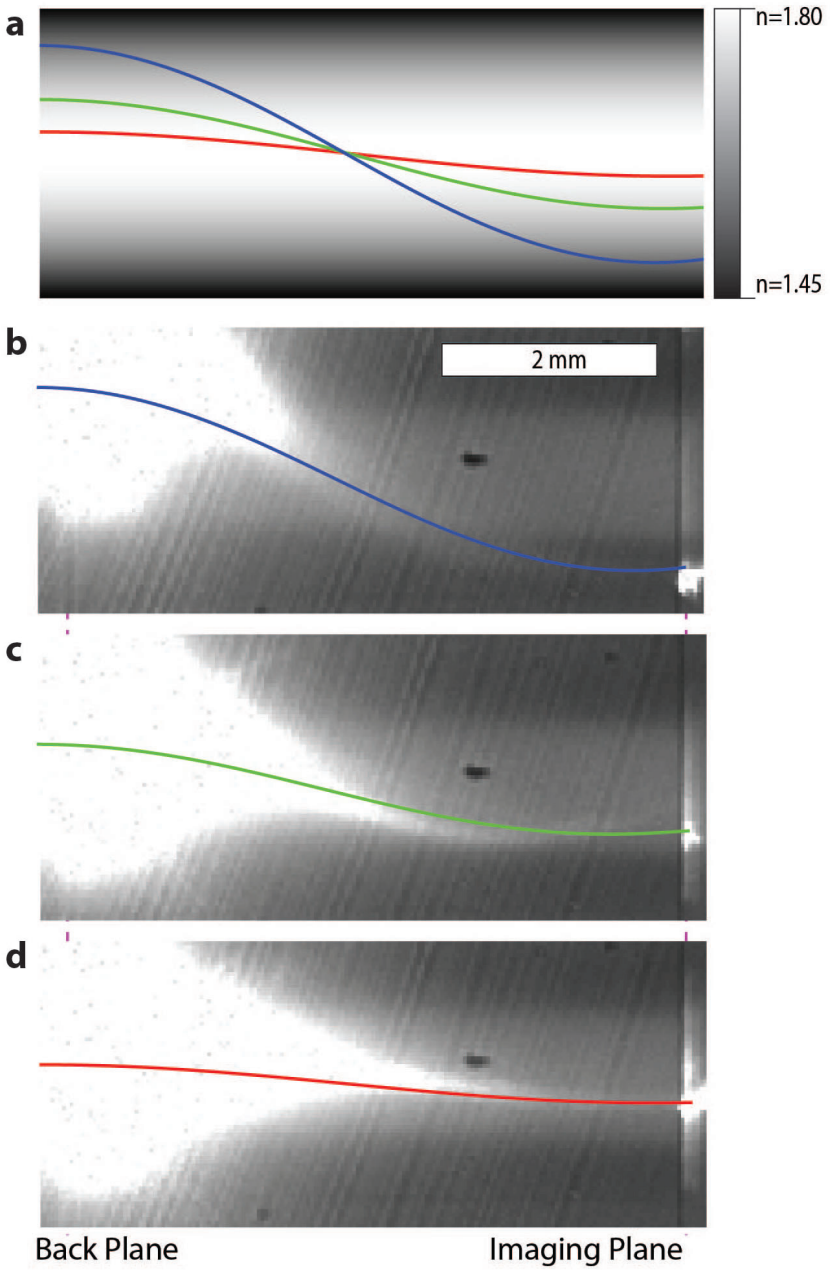

Figure 2.11: Simulation of light propagating through a parabolic lens and comparison with experimental results. a) Simulated ray trace of light (solid line) traveling through a parabolic lens at three locations. The refractive index at the center is 1.80 and decreases gradually to 1.45 at the edge. b-d) The images taken using the 4f system show the propagation of light through the parabolic lens. Experimental results given by the white traces closely match the theoretical ray trace results (solid lines).

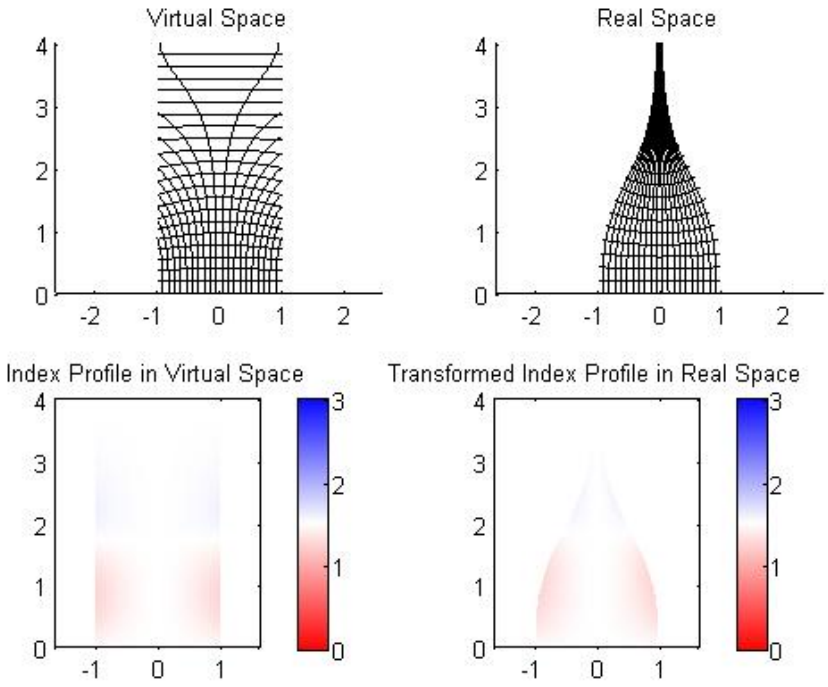

Figure 2.12: Design of a Miñano concentrator with an aspect ratio of 2 and a geometric concentration factor of 20. The top two figures show the concentrator design in real and transformed space, and the bottom images show the index profile required in real and transformed space. This concentrator requires an refractive index gradient of 0.35.

system. These losses could be reduced by oxidizing the samples to porous silicon oxide using the previously described method at the cost of decreased index contrast, which would require lower concentration ratios and higher aspect ratios. It is also important to note that these measurements were only performed at normal incidence, where the effect of the sidewall reflectivity is minimized. The angular response of the concentrators would be much worse than ideal due to imperfect reflection. We can see in figure 2.14 that even for small angles, total internal reflection is not enough to prevent many rays from exiting the device. This ray trace cannot be used to calculate the expected intensity of such a concentrator compared to an ideal concentrator because it cannot account for partial reflections. In this model, if a ray is not totally internally reflected, it is shown as exiting the device. In order to fabricate samples with a high quality reflective boundary, a technique such as metal assisted chemical etching could be used to define the sidewalls of the device, which would greatly improve its angular performance.

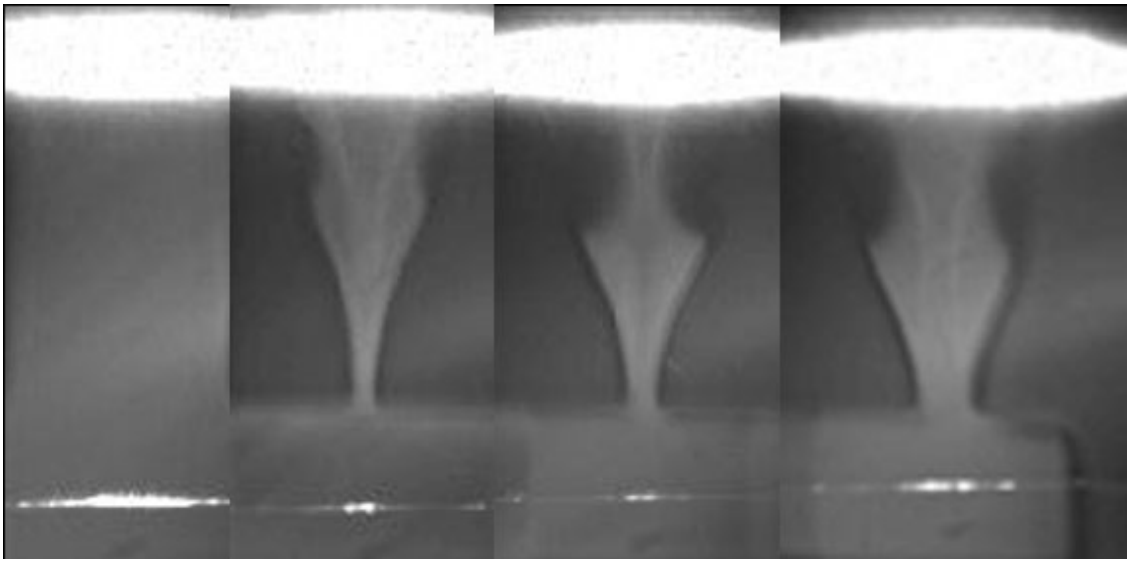

Figure 2.13: Measurement of optical concentration by three Miñano concentrators with different geometric concentration ratios. The right image is a slab waveguide, and the next three from left to right are Miñano concentrators with concentration ratios of 20, 10, and 5. The results show a clear concentration effect.

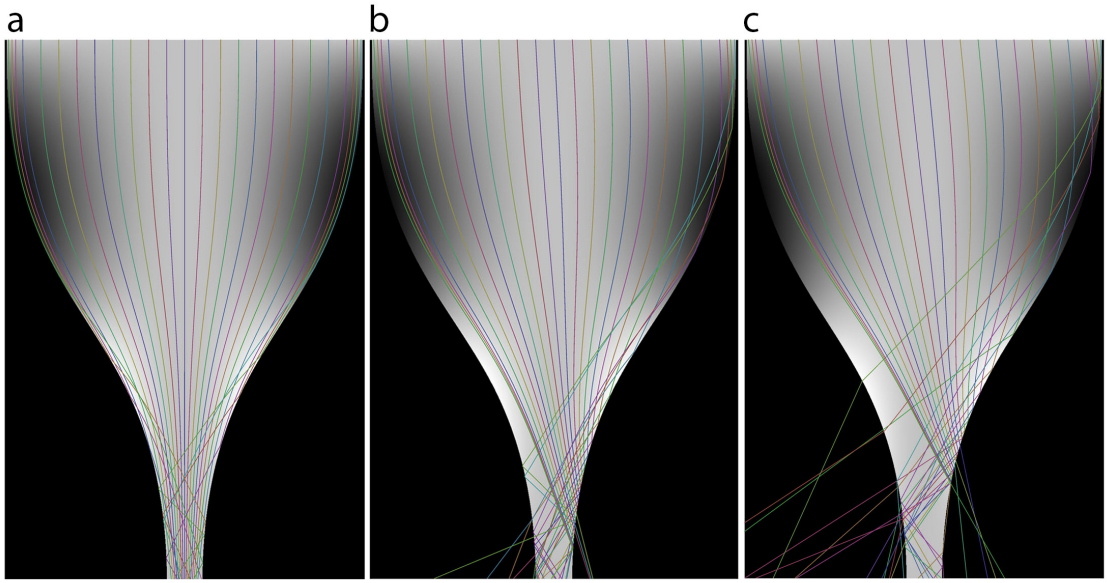

Figure 2.14: Ray tracing for light entering a Miñano concentrator without reflective sidewalls at different angles, with the angle measured from perpendicular to the inlet. a) Normal incidence. b) 50 mrad. c) 100 mrad.

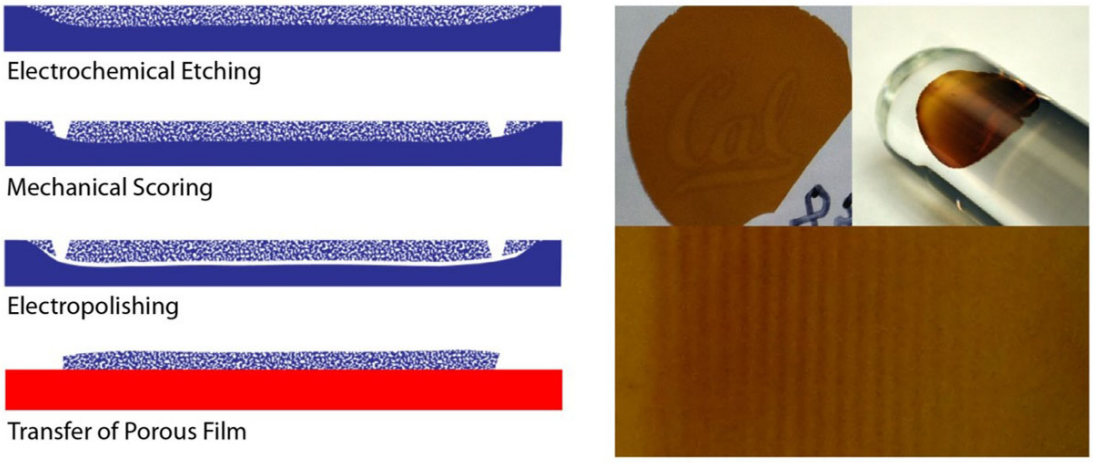

Figure 2.15: Substrate transfer method for porous silicon thin films. (Left) Schematic of process of transferring porous silicon thin films to arbitrary substrates. (Right) Three samples transferred to different substrates, demonstrating transfer of patterned films and transfer to curved surfaces.

2.6 Porous Silicon Phase Elements

After etching, the patterned porous film could be removed from the bulk silicon and transferred to another substrate. This was achieved by electropolishing, a process similar to the electrochemical etching used to form porous silicon. For electropolishing to occur, the concentration of HF in the electrolyte was reduced, allowing the interface between the porous silicon and bulk silicon to be fully electrochemically oxidized before it was dissolved by the HF. To release the porous film, first a porous film was etched by the previously described method. The electrolyte solution was then removed, and the film was mechanically scored around its edge to aid in the release from the substrate. A new electrolyte solution of 1 part 49% HF and 20 parts ethanol was added, and the sample was returned to the electrochemical cell and etched in the dark at at constant potential of 30 V for 1 minute. At lower HF concentration, the rate of dissolution of the silicon dioxide becomes much slower than its production by the electrochemical oxidation. This allows the oxidation to spread across the pores, so the entire boundary between porous and bulk silicon becomes oxidized. The silicon dioxide subsequently dissolves in the HF electrolyte, releasing the porous film. The electrolyte was then removed and the sample was flooded with ethanol. The sample floated on the ethanol, allowing it to be mechanically transferred onto any other material. After transfer, the sample was then dried in hexane to improve adhesion and minimize damage to the film. The silicon substrate from which the film was transferred could then be reused. Figure 2.15 shows this process and samples transferred onto various surfaces, including curved surfaces.

For particularly delicate samples, such as multilayer samples with large index differences

between the layers or highly porous samples, a different method for drying and transferring the samples was used. In this case, after electropolishing, the sample was rinsed in ethanol and then placed in isopropyl alcohol without drying. The sample, with the porous film sitting on top of the bulk silicon substrate but no longer attached, was then placed in a critical point dryer (CPD). In the CPD process, the sample was placed in a pressure chamber and covered with about 50 mL isopropyl alcohol. The chamber was then sealed and cooled to 0° C with liquid CO_2. The chamber was then filled with liquid CO_2 and purged several times to wash away the solvent and fully replace it with CO_2 pressurized to above 700 psi. The chamber was then heated until the CO_2 in the chamber exceeded its critical point. The supercritical CO_2 could then be removed from the chamber without ever subjecting the sample to stresses due to the surface tension of evaporating solvent. The dried sample can then be transfered to another substrate by putting the new substrate in direct contact with the released porous silicon film and then removing the original silicon substrate. The porous silicon film adheres to the new substrate. For thicker samples, it can be beneficial to spin a thin layer of PMMA or other polymer onto the new substrate prior to transfer to aid in adhesion.

This ability to removed patterned films of porous silicon from the bulk silicon substrate makes porous silicon a promising material for low cost large scale phase masks. A phase mask consists of a transparent material which, when light passes through it, causes the light to experience a different phase delay in different areas of the mask. This can then be used directly as an optical component such as a lens, placed at the Fourier plane of an optical system in order to modify the point spread function of the system, or used to generate a hologram.

Point Spread Function Engineering

The point spread function (PSF) of an imaging system is the output of the system from imaging a single point from the object plane to the image plane. In a typical $4f$ system, this is equivalent to taking the Fourier transform at the Fourier plane of the imaging system. If the extent of the imaging system was infinite, then the PSF would simply be a point. However, because all real imaging systems must be truncated, a typical imaging system has a PSF that is a Gaussian with an Airy pattern. As the imaging plane deviates from the focal point of the lens, the size of the PSF expands rapidly. This can be used in 3D imaging systems, particularly super resolution imaging techniques that depend on localization of fluorophores on a sample. Since each fluorophore is essentially a point source of light, and only its location is important for the imaging, the shape of the imaged points gives information about height of the fluorophore (i.e. its distance from the focal plane of the imaging system). However, the nonlinear response of the PSF of a standard imaging system to defocusing makes it difficult to accurately determine its position in the z dimension, resulting in inaccurate localization. By engineering the PSF, it is possible to make systems where the defocus of one fluorophore is much easier to determine, allowing localization in the z direction as precise as 10 nm [63].

In order to engineer the PSF in this way, it is necessary to impose an arbitrary phase profile at the Fourier plane of the imaging system. This is most often done using a spatial

light modulator. These devices have the advantage of being reconfigurable, but they are expensive and can be difficult to incorporate in a microscope. A cheap method of producing an arbitrary phase mask could be advantageous for such systems.

Computer Generated Holography

Holography, originally invented as a method for improving the resolution of electron microscopy in 1949 [64], is an imaging method that captures the full light field in a storage media as an interference pattern. The full 3D image can then be reconstructed. Holography has seen niche applications in mainstream technology, but so far has not lived up to its potential. Advances in holographic storage media could lead to improvements in 3D imaging devices, computer memory, microscopy, and many other areas [65, 66]. In computer generated holography (CGH), instead of recording the light field of an actual object, the phase profile required to produce a particular image is calculated (often by iterative computational methods) and a phase mask is directly fabricated to produce the desired image. Typically photosensitive polymers or etched glass are used for these phase masks, but they suffer from low index contrast or expensive and unscalable fabrication. Metasurfaces have also been used as phase masks, though the difficulty in large scale fabrication limits their practical applications [67]. A porous silicon phase mask fabricated by photoelectrochemical etching has the potential to address these issues, bringing the potential of CGH into the mainstream.

Phase Measurements

The phase delay of light passing through a material can be directly measured by interferometry. In a Mach-Zehnder interferometer, light passes through a beam splitter and is separated into two different paths. In the reference path, the light simply reflects off a mirror to a second beam splitter and then to a detector. In the other path, the light passes through the sample before hitting the mirror and the second beam splitter where it is superimposed with the reference beam. The path lengths can be adjusted by moving the mirrors. When the light from the two paths converges, the two beams are at slightly different angles, resulting in an interference pattern consisting of sinusoidal fringes. Changing the phase delay between the two paths causes the fringes to shift. These fringes can be seen as long as the difference in optical path length between the two paths is shorter than the coherence length of the light source. For highly coherent sources such as lasers, this requirement is not difficult to meet. Since it is generally not practical to know the exact differential path length of the interferometer, it is often most reasonable to measure the relative phase delay between different phase objects with a fixed reference.

The porous silicon phase samples measured consisted of a low index background with stripes of increasingly higher index patterned within. The porous silicon film was transfered onto a glass coverslip 150 μm thick. The sample was placed on a micrometer stage on one path of the Mach-Zehnder interferometer whose light source was a fiber coupled supercontinuum light source. The output of the interferometer was coupled to a spectrometer, so the

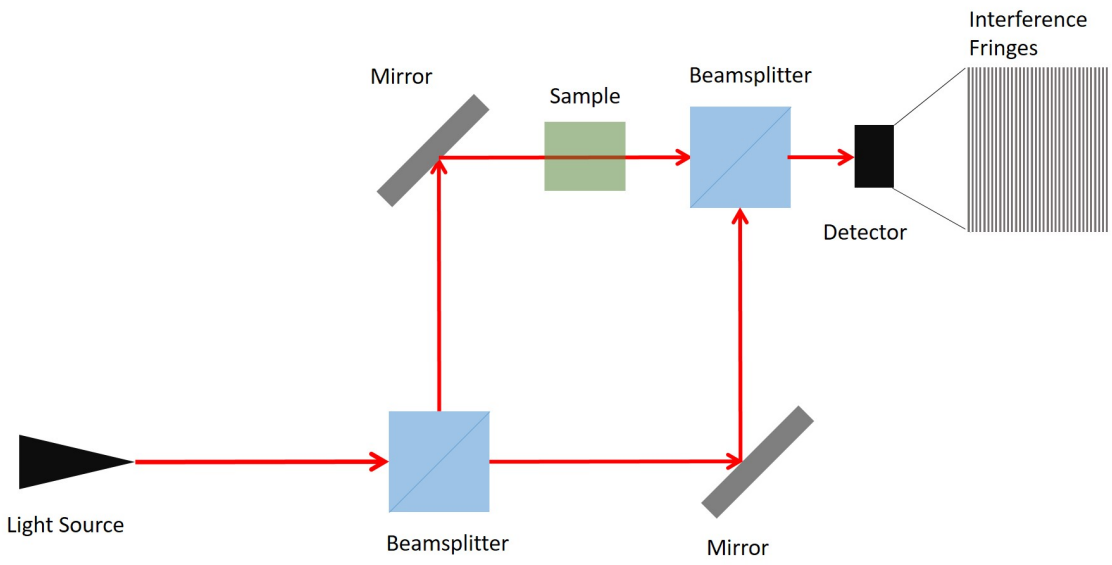

Figure 2.16: Schematic of Mach-Zehnder interferometer. Light is split into two equal paths, where one path contains the sample. The light is then recombined with a beam splitter and a detector measures the intensity. Interference between the two paths causes a sinusoidal intensity pattern at the detector. The phase delay caused by the sample can be calculated by the interference fringes.

interference at many wavelengths could be measured simultaneously. As the spectrometer recorded data, the sample was manually scanned with the micrometer so that the patterned stripes traveled perpendicular to the beam, passing through the beam. Because the rate of translation of the sample is not constant, it is not possible to directly correlate the interferometric data with a particular location on the sample, but as can be seen in figure 2.17, the approximate location and phase delay of these features is apparent. We see in figure 2.17 that the porous silicon sample is capable of imparting phase delays greater than 2π radians with phase resolution of about 0.5 radians. This could meet the requirements for phase masks for many applications, including CGH and point spread function engineering for microscopy.

2.7 Thermal Properties of Porous Silicon

We also studied the thermal properties of porous silicon [68], which are important for optoelectronic applications, novel thermoelectrics, and other unique applications such as dynamic self-assembled photonic structures discussed in chapter 3. Porous silicon's thermal properties are interesting because the porosity serves as a tool to modify silicon's thermal properties with a lesser effect on its electrical properties. For thermoelectrics, a materials

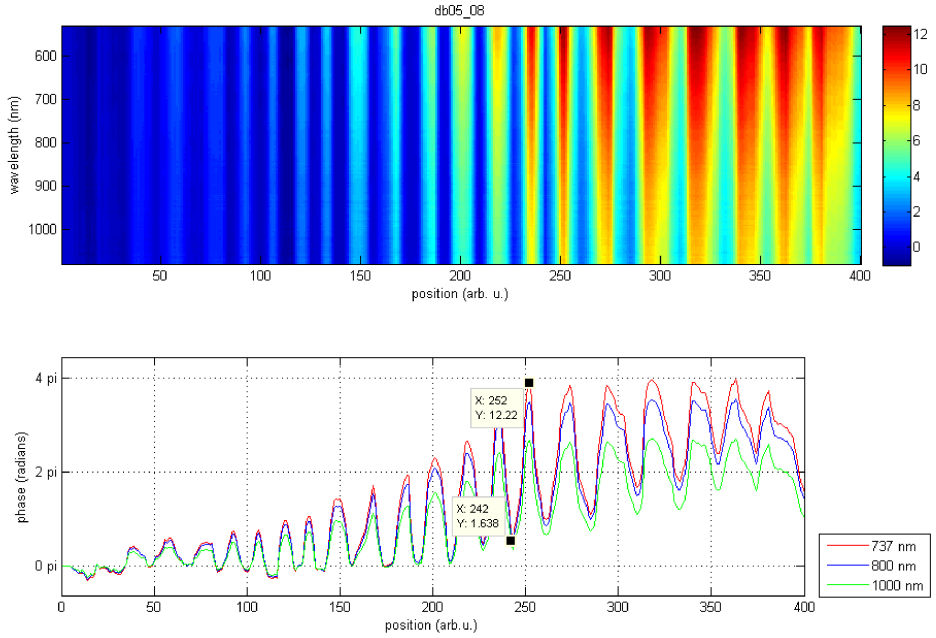

Figure 2.17: Phase measurements performed with a Mach-Zehnder interferometer using a supercontinuum light source on porous silicon samples with lines of varying porosity. The position of the sample is scanned manually with a micrometer to measure the entire 1 cm sample.

efficacy is described by its thermoelectric figure of merit, which is related to the ratio of its electrical conductivity and its thermal conductivity. Good thermoelectric materials conduct electrons much better than they conduct heat. Unfortunately, most materials that are good electrical conductors are also good thermal conductors, so it is difficult to find materials that meet these criteria to improve their thermoelectric performance. Previous research has shown that porous silicon at high porosities experiences a sharp drop in thermal conductivity and an improvement in its thermoelectric figure of merit.

In this study, we propose a model for the reduction in thermal conductivity in porous silicon based on phonon scattering at pore boundaries. We directly measure the thermal conductivity of samples with different porosities, and compare the results to the model.

The porous silicon samples were fabricated using the previously described method at a constant current of 3.53 mA/cm^2 with a uniform illumination of 450 W/m^2. Different samples were etched for 4, 8, and 12 minutes, corresponding to porous layer thicknesses of approximately 1, 2, and 3 μm respectively. The sample thickness was used to control the porosity, as a longer etch time causes a slight increase in the porosity. The porosity of these samples, measured by FTIR, ranges from 52% to 58%. This effect has been reported in previous literature [69, 70], which agreed with the measurements here. To measure the

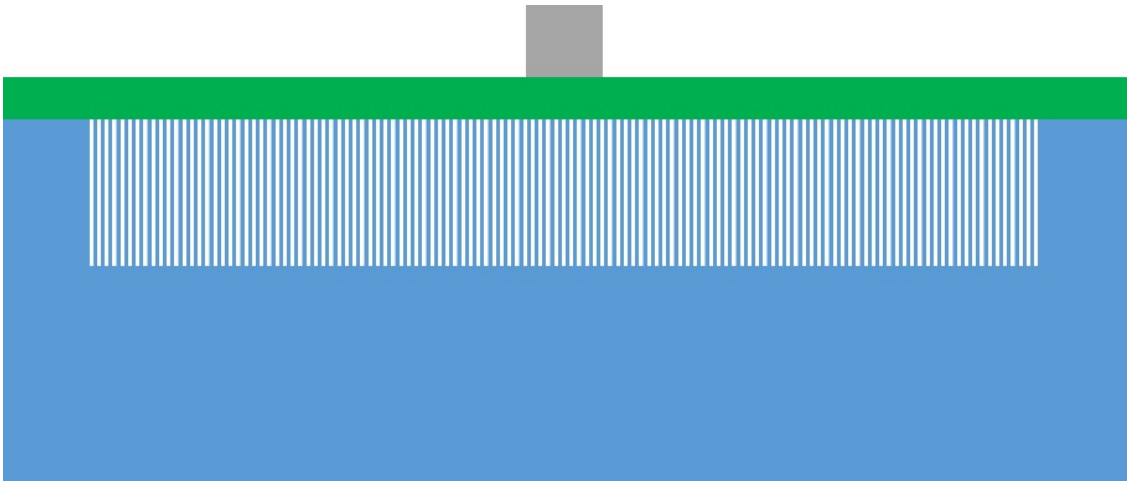

Figure 2.18: Schematic of sample for thermal conductivity measurements. Al_2O_3 was deposited on top of the porous silicon by atomic layer deposition, and a platinum electrode was deposited on top for both heating and temperature measurement.

thermal conductivity of these samples, additional fabrication steps were then required. An aluminum oxide film 250 nm thick was deposited by atomic layer deposition on top of the porous silicon, followed by strips of platinum 200 nm thick patterned photolithographically to serve as electrodes.

The thermal conductivity of these samples was measured using the 3ω method [71]. In this method the electrode serves as both the heater and thermometer. AC current is used to heat the electrode by Joule heating. The heating causes a change in resistance, which results in a small voltage oscillation that is temperature dependent, in the third harmonic of the driving voltage. Measuring the temperature a a function of frequency allows the calculation of the thermal conductivity.

The measured thermal conductivity was then compared to models based on phonon scattering. The first model assumed cylindrical pores, which did not accurately reflect the trends shown in the data. This is thought to be due to the complexities of the actual pore geometry. The pores are predominantly cylindrical, but there are also smaller pores that branch from the main cylindrical pores. This geometry was better represented by a model with hexagonally ordered spherical pores. Measured values of thermal conductivity from this as well as from other reported works fall between these two models, suggesting that the true pore morphology falls somewhere in between these models.

Neither of these models account for the large decrease in thermal conductivity as the porosity increases. The cylindrical and hexagonal model expect a decrease in thermal conductivity of 17% and 19%, respectively, when the porosity increases from 52% to 58%. The measured decrease in refractive index was 40%. More research is required to determine the cause of this discrepancy, but one possible explanation is elastic softening. The Young's modulus of silicon decreases with its porosity, which in turn decreases the phonon group

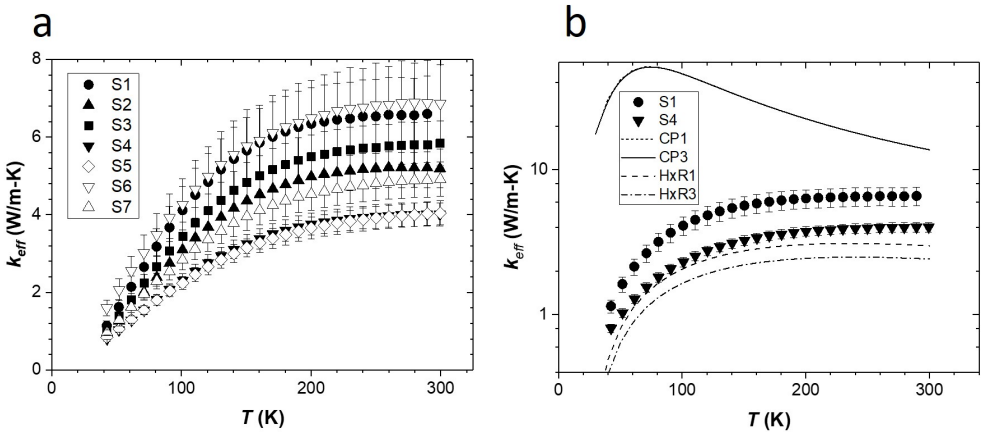

Figure 2.19: Thermal conductivity measurements. a) Thermal conductivity of seven samples with porosities ranging from from 52% to 58%. b) Thermal conductivity of two samples with porosities of 52% and 58% compared with calculated values by models assuming cylindrical pores and hexagonal pores.

velocity, an important component in the model used.

2.8 Conclusion and Future Work

In this chapter, we demonstrated a technique of photoelectrochemical etching of silicon capable of generating refractive index gradients on the order of $\Delta n = 1$ with an arbitrary 2D profile, addressing a longstanding problem that the ability to design gradient index optical devices for many applications far outstrips the ability to fabricate such devices. We used this method to fabricate waveguide devices including a gradient index lens and an ideal optical concentrator. Devices such as these could have applications as photon control elements in on-chip photonics and in photovoltaics. This technique can also be extended to three dimensions by adjusting the etching parameters temporally as well as spatially, potentially enabling a variety of devices that could otherwise not be fabricated.

By removing patterned porous silicon films from the bulk silicon substrate, we were able to form thin phase masks with arbitrary phase profiles. We demonstrated a phase delay of 2π radians, which is equivalent to delaying the wave by a full cycle. This is necessary for the design of phase masks to be used in point spread function engineering for microscopy and computer generated holography.

These techniques could also be combined with recent work that used atomic layer deposition to fill the pores in porous silicon or porous silicon oxide with titanium dioxide, which has a refractive index of 2.7 at a wavelength of 500 nm [72]. The higher index of TiO_2 compared with SiO_2 means that oxidized, and therefore transparent to visible light, devices

could be fabricated with a much higher refractive index than possible with SiO_2 alone. The paper demonstrated an index range from 1.6 to 2.0 at visible light frequencies for infilled porous silica, and a total index range from 1.2 to 2.0 by fabricating devices that combined layers that were not infilled with those that were using a liftoff technique similar to the one described previously in this chapter. Using this technique, devices with higher index gradients as well as better mechanical stability could be fabricated.

Chapter 3

Dynamic Self-Assembly for Photonics

Self-assembly, which we will broadly define as the spontaneous organization of systems from a collection of disordered units, is critical to the formation of complex structures in nature, and is increasingly being used as a tool for the fabrication of nanostructures. In nature, self-assembly is seen at length scales ranging from nanometers to light-years, with structures as diverse as DNA, cells, coral reefs, flocks of birds, weather systems, solar systems and galaxies. Self-assembly in artificial systems has not approached the diversity and complexity of its natural counterpart, but it is becoming a useful and flexible tool in the fabrication of nanostructures. Recently, DNA has been a major focus of self-assembly research, allowing the self assembly of complex 2D and 3D structures and even enabling logical computation [73–76]. DNA origami, by enabling fast computational design and programmability, has further pushed the limits of artificial self-assembly [77–79]. Recent work using DNA in structures called spherical nucleic acid provides design rules for fabricating hybrid organic-inorganic crystals with a variety of useful properties [80]. Compared with traditional fabrication methods, self-assembly has advantages including access to smaller length scales, the ability to bridge the gap between nano and meso length scales, and the lack of strict environmental limitations such as vacuum and substrate requirements among others.

3.1 Static Vs. Dynamic Self-Assembly

One major limitation of artificial self-assembly compared to self-assembly in nature is reconfigurability. A cell is able to respond to its environment in many ways, while even the most complex structure formed by techniques such as DNA origami is essentially a crystal. Its structure is fixed after assembly. The vast majority of artificially self-assembled structures do not possess any reconfigurability, while it is extremely common on the natural world [81, 82]. The fundamental difference between dynamic and static self-assembly is best understood through thermodynamics [83–86]. A static system is at thermodynamic equilibrium. Often (but not always) energy input is required initially to overcome an energy barrier, but subsequently the system achieves equilibrium and does not require the addition

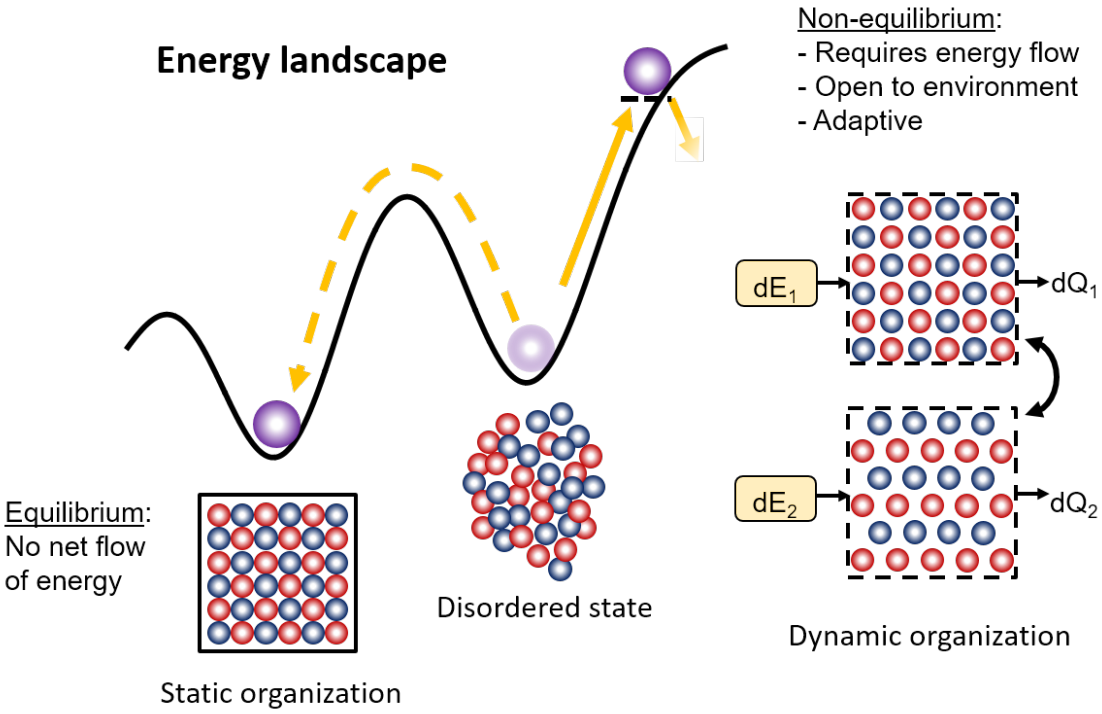

Figure 3.1: Thermodynamic description of static versus dynamic self assembly.

of any energy to maintain this state. A dynamic system exists in a non-equilibrium steady-state, requiring continual input of energy to maintain. Order emerges as a consequence of the balance between incoming energy and dissipative losses in the system. When the energy input ceases, the system becomes disordered again. The effect of this is that in addition to requiring energy, a dynamic system also responds to the energy input and can change itself based on changes to the energy input. A well designed system could exist in many ordered non-equilibrium states and dynamically switch between them when the energy entering the system changes. Most works demonstrating dynamic self assembly have used magnetic forces [87] or forces from fluid flow [88] to supply energy to the system. A recent work demonstrated the formation of a pseudo-crystal with a phononic bandgap due to the force from acoustic waves [89], but dynamic self-assembly to manipulate light waves has not been demonstrated.

3.2 Designing a Dynamic Band Structure

The concept of a device with dynamically self-assembled band structure begins with the distributed Bragg reflector (DBR). A DBR consists of multiple layers of (usually two) materials with different refractive indexes. The layer thicknesses and indices are designed such that the reflected waves from each interface at the desired wavelength interfere construc-

tively, making it reflect strongly at a particular wavelength. Because of the nature of the design, DBRs are dispersive and angle sensitive. The transmissivity of a DBR as a function of wavelength can be considered analogous with a semiconductor band structure, with the photonic band gap being the region of strong reflectivity in the DBR.

Tunable DBRs have been demonstrated by using strain to change the layer spacing and index [90] and the thermo-optic effect [91]. Sensors based on Bragg reflectors fabricated from porous materials including porous silicon have been demonstrated, where the working principle is that when the analyte infiltrates the pores, they change the effective index of the DBR and thus change its optical properties [92–95]. In these cases, the photonic band structure of the DBR is modified using an external stimulus, such as applying strain or using an electrical heating element to heat the entire device. A dynamically self assembled band gap means that the energy of the light wave interacting with the DBR causes it to dynamically reconfigure itself, thus changing how it interacts with the light wave. In this case, the thermo-optic effect is used to cause this feedback, but the method and results are quite different from previous works. The layers of the DBR are thermally isolated, so the temperature of each layer is independent. The optical absorption of the high index layer should be significantly higher than that of the low index layer. When light hits the DBR, it causes the individual layers to heat up, particularly the high index layers. The thermal isolation of the layers means that each layer can be at a different temperature. As layers heat up, their index changes due to the thermo-optic effect. This causes the band structure to change and evolve in response to the illumination. Because the transmissivity of the DBR is wavelength dependent, different layers absorb different amounts of light. As the band structure of the DBR changes the transmission, a feedback loop occurs in which the heating due to optical absorption causes the band structure to evolve, leading to some interesting and unexpected effects. Figure 3.2 shows the numerical simulation of a system of five layers separated by vacuum when hit with a 1064 nm laser. The separate but interrelated evolution of the temperature in each individual fin can be seen.

Although this may not meet certain strict definitions of self-assembly, in which the aggregation of particles into an ordered structure is required, the mechanism and thermodynamics of this situation lead us to believe that this system should be considered dynamic self-assembly. Here, we assemble the optical phase instead of spatially assembling particles. One might say that there is no fundamental difference between this work and shifting the band gap of a DBR by heating the entire device. However, this ignores some of unique consequences of mechanism at work, which match very well with the thermodynamic description of dynamic self-assembly and result in desirable device properties not available in a simple tunable DBR. One particular example of this is the consequences of starting with a disordered system. If the spacing of the layers in a DBR includes some disorder (there is some random deviation from the designed spacing) the performance of the DBR will dramatically suffer. If the whole device is heated, the transmission spectrum will still certainly change, but it will not effect the overall device performance, and it may not change in a particularly useful or regular way. However, in the system we describe, the complex relation between absorption and dissipation in each fin means that the device performance will be more like

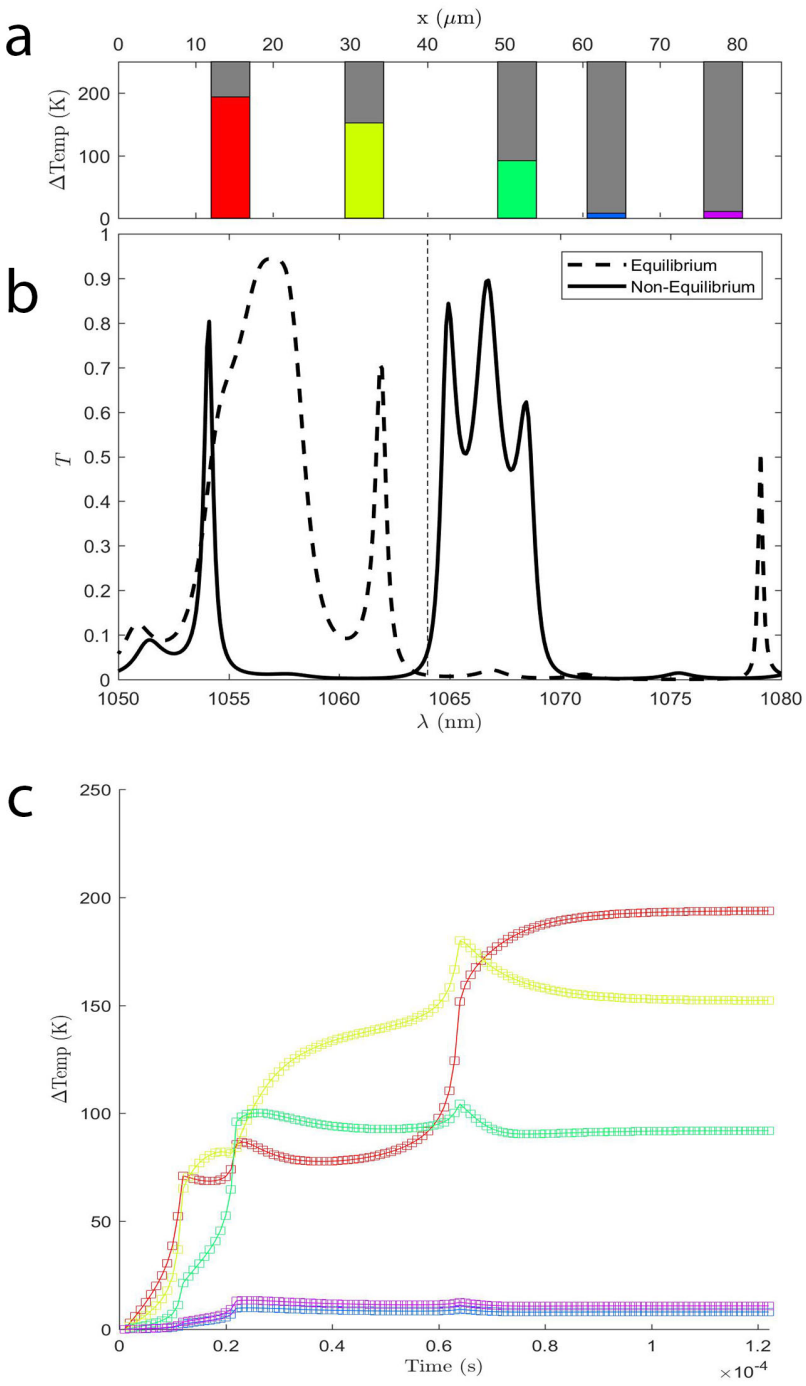

Figure 3.2: Numerical simulation of thermal evolution in five layer DBR. a) Physical schematic of structure with 5 fins with irregular spacing (i.e. a DBR with a defect). Colored bars within fins show the calculated temperature of each fin at steady-state after illumination with a 1024 nm laser. b) Calculated transmission spectrum of structure at the same time as in (a). c) Temperature of each fin as a function of time, showing the temperature of each fin evolves individual as the structure's properties change. Colors correspond to particular fins in (a).

a perfect DBR (i.e. the structure becomes more ordered). The DBR tuning in this device, instead of just changing arbitrarily due to heating, is locked to the laser frequency due to the feedback mechanism, which can make it useful as a tunable filter and photon control mechanism, rather than just a sensor, where any detectable change is acceptable. It is also important to note that the increase in order is entirely dependent on the continued addition of energy (it is a nonequilibrium process) and will cease as soon as energy is no longer added and the fins return to thermal equilibrium.

3.3 Device Design

Two device designs were explored. In the first, the DBR was fabricated by electrochemically etching silicon to form a porous silicon superlattice. Changing the current during the etching process allowed discrete switching between high porosity and low porosity etching in order to form a DBR. Porous silicon has extremely low thermal conductivity, which is required for the dynamic self assembled band gap. However, FEM simulations of heat flow in such a structure indicate that even with the low thermal conductivity of porous silicon, thermal crosstalk between layers would be too high to allow the dynamic self assembly effect. The nature of heat conduction in porous silicon, where conduction mostly occurs through the silicon nanowires, not the pores, means that even evacuating the air from the sample would not significantly reduce the thermal conductivity.

To address this issue, a design with air (or vacuum) as the low index layer of the DBR is required. The difficulty in fabricating multilayer suspended membranes with the thicknesses required makes such a design nonviable, so another approach was required. The design chosen uses multiple fins etched perpendicular to the substrate with air in between as the layers of the DBR. This approach simplifies fabrication compared to other methods which might be able to yield a DBR with air as one layer, but it does make optical measurements more difficult, as the sample is oriented perpendicular to the substrate, making transmission and reflection measurements much more challenging.

3.4 Fabrication

The samples were fabricated on silicon-on-oxide (SOI) wafers consisting of 25 microns of single crystalline silicon on top of 5 microns of silicon oxide on a bulk silicon substrate. The DBR structure is fabricated in the 25 micron device layer with the oxide providing thermal insulation to minimize thermal crosstalk through the attached ends of the fins.

Fabrication of the fin DBR consists of photolithographic patterning of the SOI substrate followed by pattern transfer by deep reactive ion etching (DRIE). In order to couple light into the DBR through an objective, the fins must be very close to the edge of the wafer. If the fins are further from the edge, they must be taller. Otherwise, the focused light from the objective will be shadowed by the edge of the wafer and will not be able to couple into

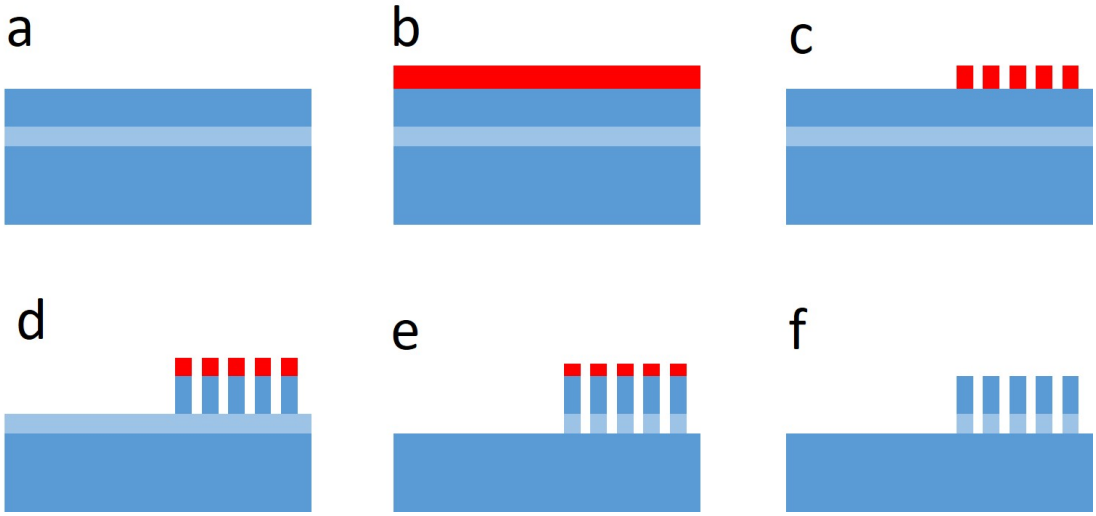

Figure 3.3: Process for fabricating a DBR with a dynamically self-assemblyed band structure with fins perpendicular to the substrate. a) Use commercial silicon-on-insulator substrate with 25 μm silicon device layer and 5 μm oxide layer. b) Spin ma-P positive photoresist. c)Expose and develop photoresist. d) Etch through silicon device layer by DRIE. e) Etch oxide layer by inductively coupled plasma reactive ion etching f) Use oxygen plasma to strip photoresist and etch residue.

the structure. Because the fin height is limited by the silicon thickness on the SOI wafer, fabricating the structure within a few tens of microns from the wafer edge is necessary. In order to do this, photoresist was spun onto a large wafer, which was then cleaved into smaller chips. Photoresist was not spun directly onto the smaller chips as edge effects during the spinning process result in uneven resist thickness, decreasing the accuracy of the lithography and also making the resist less effective as an etch mask.

Photolithography was performed using ma-P positive photoresist (Microchem) with a thickness of about 2 μm. This photoresist was chosen because positive resist makes alignment easier, and this particular resist was found to be a particularly effective etch mask, with selectivity greater than 20:1. Using a mask aligner the patterns could be precisely aligned within a few microns of the edge of the chip. After alignment, the chip and mask were placed in vacuum contact and exposed for 3 seconds in broadband UV illumination with intensity of 14 mW/cm^2. Exposed samples were developed in an aqueous alkaline developer solution for 2 minutes.

The samples were then attached to an oxide coated 6 inch silicon wafer using thermal release tape, which was placed in the DRIE etching machine (Surface Technology Systems). This tool uses the Bosch process, consisting of a two step etch. The first step is an etch in SF_6 gas for 7 seconds, and the second is sidewall passivation by depositing fluoropolymer from C_4F_8 gas precursor, which takes 5 seconds. Each cycle etches approximately 350 nm

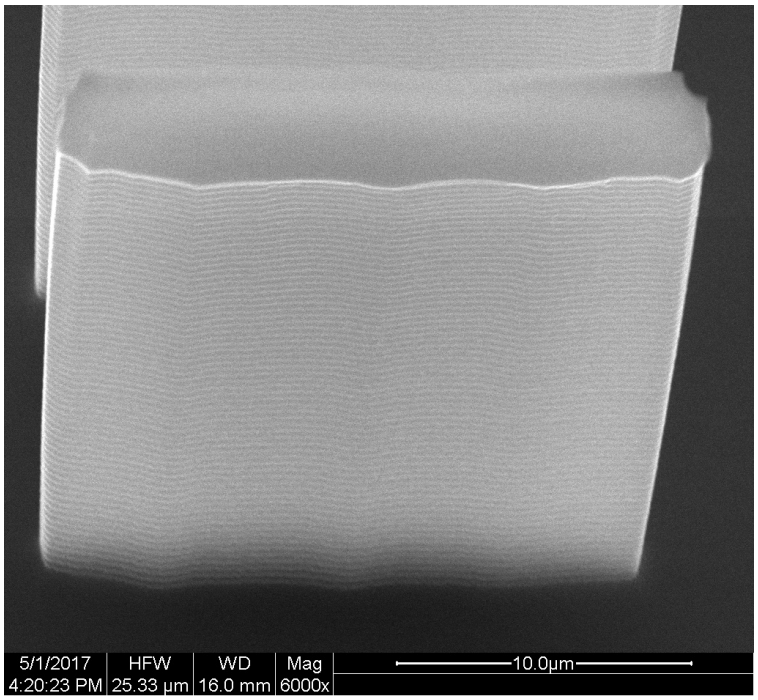

Figure 3.4: SEM micrograph showing scalloping effect on the face of a single 20x20 micron fin. Image was taken in an FEI Quanta 200 SEM with the sample viewed at a 30° tilt along the long axis of the fin.

of silicon. This recipe is optimized to minimize scalloping of the sidewalls at the expense of etch speed and selectivity. Scalloping occurs due to the two step process and gives sidewall roughness on the order of 100 nm deep with a period of 350 nm, the same as the etching depth per cycle.

The sample was then removed from the etcher and released from the handle wafer by heating on a hotplate for 1 minute at 140° C. It was reattached to another 6 inch silicon handle wafer and placed in another etching tool (Surface Technology Systems) for deep oxide etching. This is an inductively coupled plasma etcher using C_4F_8 gas for highly anisotropic oxide etching at a rate of approximately 300 nm per minute. After etching, the sample was removed from the handle wafer and placed in a parallel plate reactive ion etching tool (Plasmatherm) and exposed to oxygen plasma at 200W for 5 minutes to remove any remaining photoresist and deposited fluorocarbons from the DRIE etch.

3.5 Optical Measurements

To measure light transmission through the device, the sample was mounted vertically on a microscope stage. A 1 W quasicontinuous laser at 1064 nm was coupled into the microscope through a fiber and focused through a low NA objective onto the front fin of one

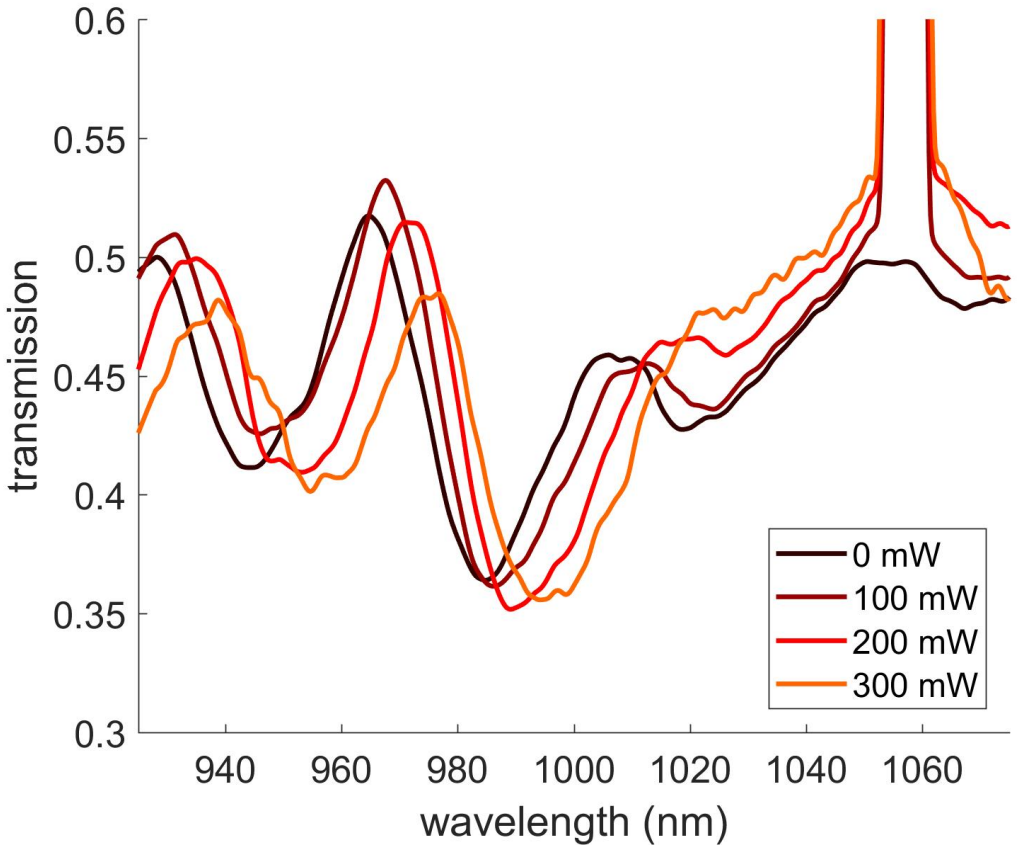

Figure 3.5: Transmission spectra for a single fin at different pump powers. Because there is only one fin, there is no band gap, but the interference due to reflections off of the front and back surface of the fin can be seen. As the pump power increases, the temperature of the fin also increases, and the index change due to the thermo-optic effect can be seen in the shift of the transmission spectrum as the power is increased.

DBR. Simultaneously, a low power white light was focused on the sample and coupled to a spectrometer in order to measure the transmission spectrum of the DBR. As the high power laser heats the silicon fins that comprise the DBR, their refractive index shifts, changing the transmission spectrum. For a single fin, this shift in transmission has been measured as seen in the figure. Work is ongoing to measure the effect in a full DBR structure and to demonstrate the predicted feedback between layers and self-healing effect.

Chapter 4

Nonlinear Phase Gradient Metasurfaces

Metasurfaces have recently become a popular method of controlling the phase of light. Metasurfaces have been demonstrated as replacements for traditional optical components, for digital holography, optical wavefront shaping, and many other applications. Although there is no universally accepted definition of a metasurface, they generally consist of a single subwavelength layer of subwavelength optical antennas in a spatially varying array. By introducing a discreet phase discontinuity at the interface, metasurfaces can impart an arbitrary phase profile on incident light [96]. There are two main mechanisms for introducing this phase discontinuity. In the first, phase delay is caused by the optical dispersion due to the resonance of an antenna [97]. Metal antennas utilizing plasmonic resonance are most common, but dielectric antennas utilizing Mie resonance have also been demonstrated [98]. In these cases, the spatial variation comes from an array of antennas with different shapes and thus different dispersions. In the second, Pancharatnam-Berry phase (also called geometric phase) is introduced by the interaction between circularly polarized light and the antenna [99]. Pancharatnam-Berry phase is introduced due to cyclic processes. In this case, antennas with identical shapes but different orientation are used to introduce the spatial phase variation.

One of the key properties of a metasurface is that the introduction of phase discontinuities at an interface results in changes to the way light refracts at the interface. Refraction, caused by the phase delay from light entering a material with a different refractive index, is described by Snell's law (equation 4.1), which was originally derived in the 10th century C.E. by Ibn Sahl in Baghdad, but was rediscovered by Western scientists in the 17th century due to the work of Willebrord Snellius, among others who independently did similar work.

$$n_i sin\theta_i = n_t sin\theta_t \tag{4.1}$$

Where n_i and n_t are the refractive indices of the two media and θ_i and θ_t are the angle of incidence and angle of refraction respectively.

Snell's law cannot account for changes in the refraction due to discrete phase discontinuities, such as phase introduced by a metasurface. One of the seminal works in the field of metasurfaces addressed this issue and derived a generalized Snell's law (equation 4.2), which includes phase discontinuities and can be used to calculate the refraction of light caused by arbitrary phase elements [100].

$$sin(\theta_t)n_t - sin(\theta_i)n_i = \frac{\lambda_0}{2\pi}\frac{d\Phi}{dx} \tag{4.2}$$

Where λ_0 is the free space wavelength of the light and $\frac{d\Phi}{dx}$ is the constant phase gradient at the interface.

Recently, metasurfaces have been used to demonstrate an ultrathin invisibility cloak [101], efficient holograms [102, 103], a laser cavity [104], and control of quantum emitters [105] among many other applications. Using metasurfaces to induce and control nonlinear effects has also been a major research focus recently [103, 106–110]. Metasurfaces are attractive for nonlinear optics because they enable strong optical interactions without requiring long propagation lengths, and because they eliminate the phase matching problem common in traditional nonlinear optics. Nonlinear metasurfaces have been used to induce giant nonlinear circular dichroism for sensing applications and to spatially control the phase using both split ring resonators and Pancharatnam-Berry phase to control the nonlinear harmonic without affecting the fundamental wave. Looking at equation 4.2, it is evident that this generalized Snell's law does not apply for nonlinear metasurfaces, as the free space wavelength is not constant through the device, and the interaction between the higher harmonic and both the bulk material and phase elements must be accounted for.

4.1 Nonlinear Optics

Nonlinear optics can refer to any of a number of phenomena in which a materials optical properties change in response to an applied field. Because the optical properties are no longer constant, the output of the system dos not scale linearly with the input, which is why all of these very different effects are grouped under the term nonlinear optics. In chapter 3, we utilized one such nonlinearity, the thermo-optic effect, in which the refractive index of the material was changed by changing the temperature.

Here, we will focus on optical nonlinearity caused by the electromagnetic field of the light itself. The cause of this nonlinearity is the polarization of a material in response to the electromagnetic field [111]. This is governed by the susceptibility, χ, of the material. At low electromagnetic field strength, polarization is related to the electric field by equation 4.3:

$$\mathbf{P} = \varepsilon_0 \chi \mathbf{E} \tag{4.3}$$

Where $\mathbf{P}$ is the polarization, $\mathbf{E}$ is the electric field, and χ is related to the relative permittivity of the material by $\chi = \varepsilon_r - 1$. However, this relation breaks down when the electromagnetic

field is very strong. In that case, we can expand the polarization as a Taylor series in the following form:

$$\mathbf{P} = \varepsilon_0\chi^{(1)}\mathbf{E} + \varepsilon_0\chi^{(2)}\mathbf{E}^2 + \varepsilon_0\chi^{(3)}\mathbf{E}^3 + ... + \varepsilon_0\chi^{(n)}\mathbf{E}^n \tag{4.4}$$

Higher order terms of χ are extremely small in most materials, so in order for their effects to make a significant contribution to the polarization, the electric field must be very strong. Because of this, this type of optical nonlinearity was not observed until the invention of the laser, which provide such light intensities.

Using this property of materials, many phenomena can be observed. The most common of these are a variety of different effects collectively called frequency mixing processes. These include second harmonic generation (SHG), third harmonic generation (THG), sum and difference frequency generation, optical parametric oscillation, and many others. Another important third order nonlinear effect is called the optical Kerr effect, which leads to self focusing of a beam of light due to the nonlinear index change effectively turning the medium through which the light travels into a lens.

Here, we derive and experimentally verify a generalized nonlinear Snell's law, which can accurately predict the refraction of light at an interface containing phase discontinuities which affect both the fundamental frequency as well as higher harmonics. We use this nonlinear metasurface to demonstrate asymmetric transport, in which the refraction of light through the device in one direction is not equivalent to the time-reversed refraction of light. Asymmetric transport in electrical devices such as the diode is critical to electronics, and similar optical devices could be an important component of a complete toolkit for on-chip photonics. While asymmetric transport is a common application for bulk scale nonlinear optics, this usually requires large pieces of nonlinear crystal materials and is not compatible with integrated photonics [112–118]. Other recent work has also demonstrated asymmetric transport of acoustic waves [119]. This work is the first demonstration of asymmetric transport using metasurfaces, which are inherently well suited to chip-scale devices and integration due to their deep subwavelength size in both lateral dimensions and thickness.

4.2 Generalized Nonlinear Laws of Reflection and Refraction

As with the classical Snell's law, we begin the derivation using Fermat's principle of least time, whose modern version is that a ray of light follows a path such that an infinitesimal variation in the path yields an infinitesimal variation in the time for the ray to traverse it. By summing the time derivative of all parts of the path, including any phase delay at the interface, and setting the sum equal to zero, we can derive the path of least time, from which the angle of refraction can be solved. For the nonlinear case, it is also necessary to account for the frequency conversion at the interface. These components of the optical path are illustrated in figure 4.1.

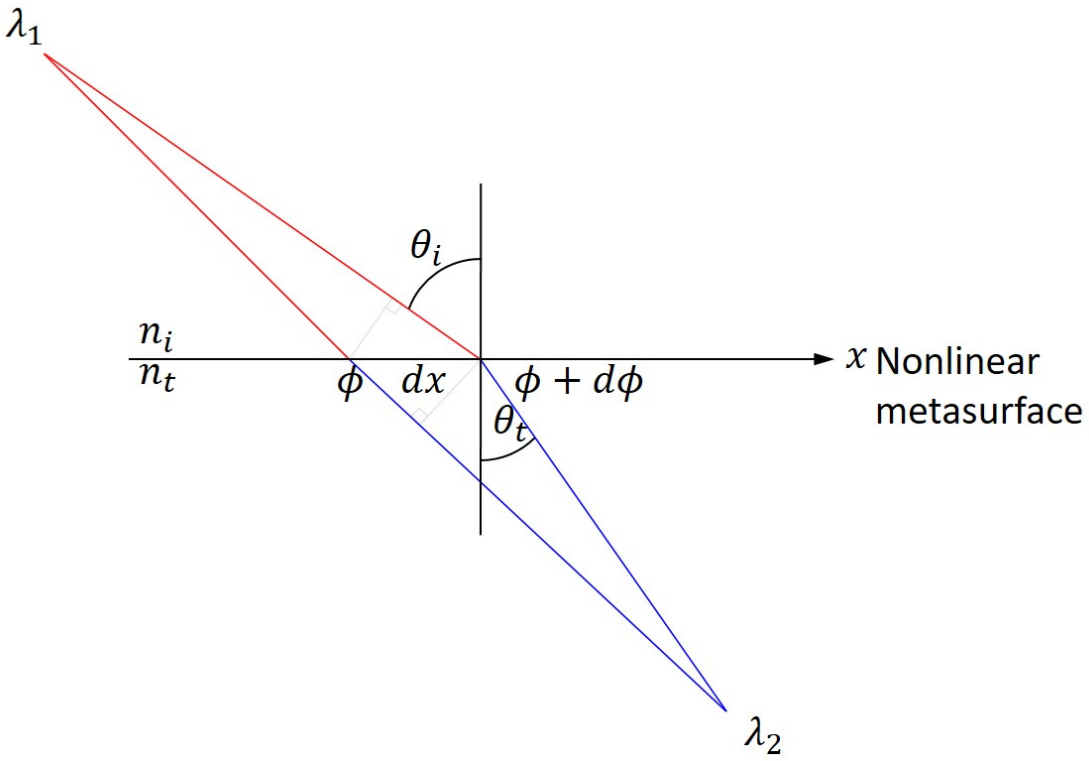

Figure 4.1: Diagram of differential optical paths for rays of light passing through a nonlinear metasurface.

By summing these components we obtain the equation:

$$\frac{2\pi}{\lambda_1} n_i sin\theta_i dx - \frac{2\pi}{\lambda_2} n_t sin\theta_t dx + d\phi + \frac{2\pi}{\lambda_2}\frac{c}{n_i}\frac{n_i sin\theta_i dx}{\frac{c}{n_i}} - \frac{2\pi}{\lambda_1}\frac{c}{n_i}\frac{n_i sin\theta_i dx}{\frac{c}{n_i}} \tag{4.5}$$

which simplifies to:

$$n_t sin\theta_t - n_i sin\theta_i = \frac{\lambda_2}{2\pi}\frac{d\phi}{dx} \tag{4.6}$$

Following a similar approach for the reflected ray, we can also derive a generalized nonlinear law of reflection, given in equation 4.7.

$$sin\theta_r - sin\theta_i = \frac{\lambda_2}{2\pi n_i}\frac{d\phi}{dx} \tag{4.7}$$

4.3 Fabrication of Nonlinear Metasurfaces

The devices consist of a quartz substrate with a 60 by 60 μm array of gold nanobars with a local periodicity of 400 nm in the x and y directions on top. Coating the nanobars is

poly(9,9-di-n-octylfluorenyl-2,7-diyl) polymer (PFO), a light emitting polymer with a strong nonlinear response. In addition to the nonlinearity directly from the PFO film, it has also been demonstrated that the nonlinear response from a gold nanoantenna embedded in PFO is orders of magnitude greater than that of either on their own [106].

Fabrication of Gold Nanobars

Gold nanobars were fabricated on the quartz substrate by electron beam lithography followed by a liftoff process. First, A2 PMMA was spun onto a 1.5 cm square quartz chip at 2000 rpm and heated at 180° C on a hotplate for five minutes to drive off any remaining solvent. The chip was then placed in the vacuum chamber of an electron beam evaporator (CHA). When the chamber pressure reached 9×10^{-7} Torr, 5 nm of chromium was evaporated at 0.01 nm/s. The chromium is necessary to allow a conductive path for electrons to be removed from the surface and prevent charging of the sample during electron beam lithography. The more traditional method to achieve this would have been to deposit a few nm of a transparent conductive oxide such as indium tin oxide (ITO) before coating the substrate with PMMA and leaving it on the sample. However, ITO itself is known to have a nonlinear response, so in order to eliminate this possible source of confusion in experimental results, an alternative technique that did not require any additional material to remain on the sample was used. This does result in greater variance in nanobar size as well as edge roughness due to electron scattering from the chromium layer during electron beam lithography. This likely causes a broader resonance and weaker absorption in the nanobar arrays, but it is not a major effect and the resonance is still easily strong enough for the purpose of this experiment. SEM images in figure 4.2 show the effects on the nanobar structure of the two fabrication techniques.

Electron beam patterning was performed in a 50 kV electron beam writing tool (Crestec: Tokyo, Japan). The patterns consisted of rectangles 55 nm by 205 nm at various orientations. A single unit cell consisted of the same rectangle rotated 180 degrees in 6, 8, 12, or 16 steps depending on the sample, with each bar separated by 400 nm. This unit cell was then repeated to fill the 60 by 60 micron array. Control samples with all bars oriented vertically and all bars oriented at 45° were fabricated on the same chip.

After the lithography was completed, the chip was dipped in CR-7 chromium etchant for five seconds to remove the chromium film. The chip was then developed in a 3:1 mixture of isopropyl alcohol and methyl isobutyl ketone (4-methylpent-2-one), which was placed in an ice water bath to maintain a uniform temperature of 0° C, for five minutes.

The chip was then returned to the evaporator and coated with 2 nm of chromium followed by 30 nm of gold. After the evaporation, it was placed in a vertical sample holder and immersed in acetone on a hot plate set at 75° C for five hours. Due to heat loss and inaccuracy in the set point of the hot plate, the actual temperature of the acetone bath was just below its boiling point of 56° C. A pipette was then used to to spray jets of acetone over the surface of the sample while it was still immersed in acetone to help remove the excess

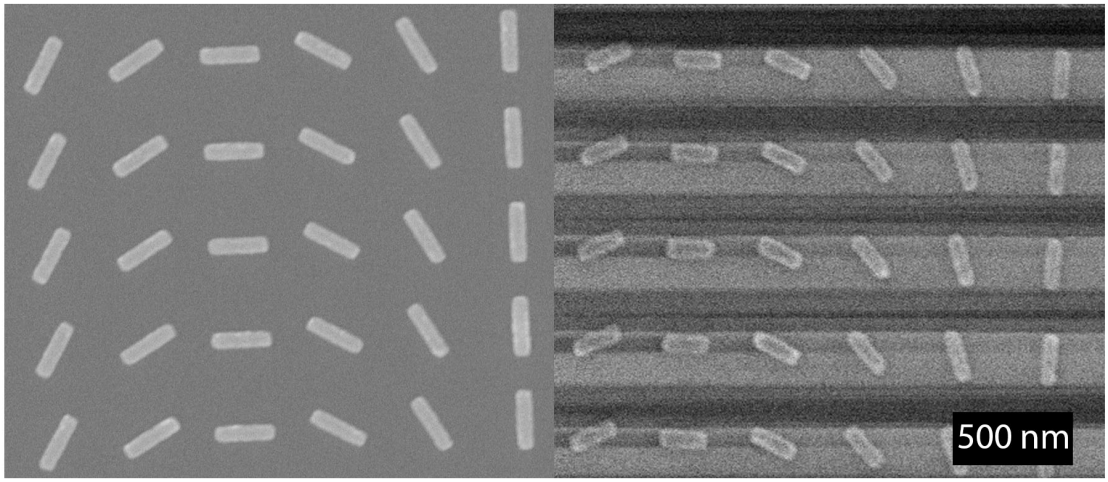

Figure 4.2: SEM micrographs showing similar samples fabricated with different conductive layers for electron beam lithography. (Left) Sample fabricated with 2 nm ITO underneath PMMA resist. (Right) Sample fabricated with 5 nm chromium on top of PMMA resist and subsequently removed. Feature size broadening and increased edge roughness can be seen on the right sample. Image quality is also drastically affected by the presence or absence of the conductive layer, as charging artifacts strongly affect the SEM imaging in the right micrograph. These can be eliminated by metalization of the sample, but this would also make the sample unusable for experimental measurements.

material. The sample was then removed from the acetone, rinsed with isopropyl alcohol, and dried with a nitrogen gun.

The samples were imaged and measured using SEM, which showed that the nanobars were consistently 10-20 nanometers larger than the design. This did not depend on the location of a nanobar within the pattern, so the proximity effect was not the cause. The same pattern was written on a quartz substrate with 2 nm of ITO sputtered on top before the PMMA resist. In this case, the size of the nanobars was within a few nanometers of the designed size, indicating that the cause of this feature broadening is the chromium layer on top of the resist. This makes sense, as the polycrystalline metal film is likely to cause electron scattering, which would increase feature size. By fabricating a series of nanobar arrays with different designed sizes, it was determined that there is a linear relationship between the designed size and the actual size. A series of nanobars with a range of designed sizes was fabricated, and a linear regression was used to determine the pattern required to achieve the desired nanobar size. Because the important metric in this case is the resonant frequency of the nanobars, each sample was measured in FTIR to determine its resonant frequency. The resonance was then plotted as a function of designed length, and the necessary length to achieve the desired resonance was calculated by the linear relationship between resonance and designed length. The design with the desired resonance of 1250 nm required writing

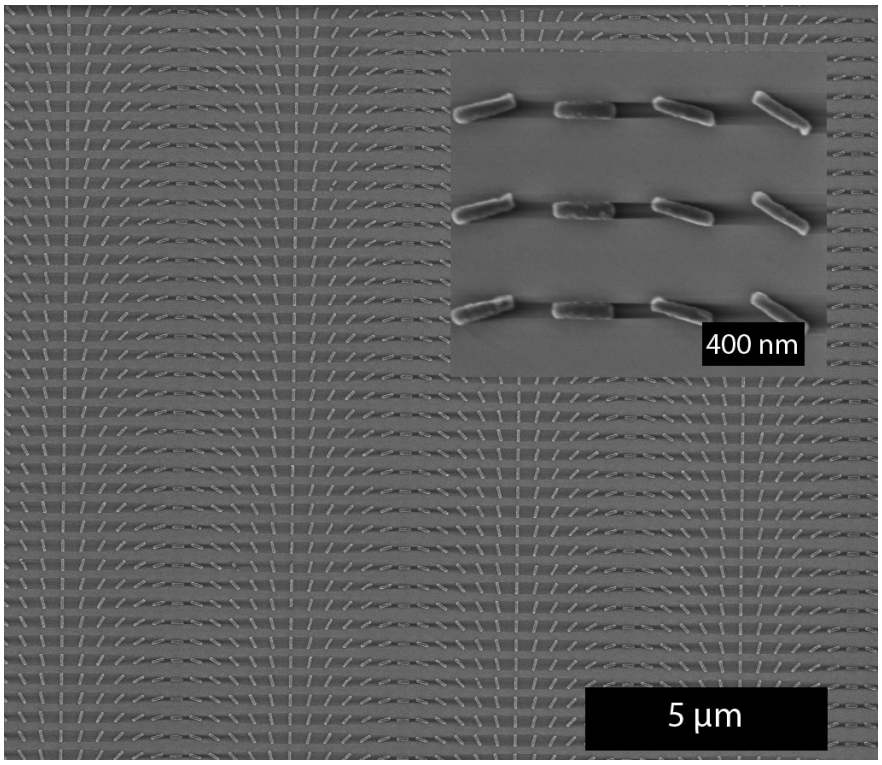

Figure 4.3: SEM micrographs showing the sample with 12 nanobars at different angles in each unit cell. Inset shows a close up view of the same sample. The discolored bands near the nanobars are imaging artifacts due to charging caused by accumulation of electrons in the nonconductive substrate.

nanobars with a nominal size of 196 nm long and 50 nm wide, which resulted in fabricated nanobar dimension of approximately 205 long and 55 nm wide.

SEM imaging was always performed at this stage of sample preparation, as the next step involves deposition of a polymer film over the nanobars. This helped to avoid damaging this film with high energy electrons and to minimize imaging problems due to electrical charging of the sample. Even without the polymer film, charging was still an issue as the sample was fabricated on quartz, which is not conductive. To completely eliminate charging, it would be necessary to coat the sample in metal to make it conductive, which would destroy the sample. Figure 4.3 shows SEM micrographs of the sample with twelve discrete phase levels in each subwavelength unit cell.

PFO Coating

PFO for spin coating was prepared from powder which is commercially available. Three mL of toluene was added to an amber vial containing 35 mg of PFO powder. The mixture was heated on a hot plate at 80° C for one hour to dissolve the polymer. The solution was

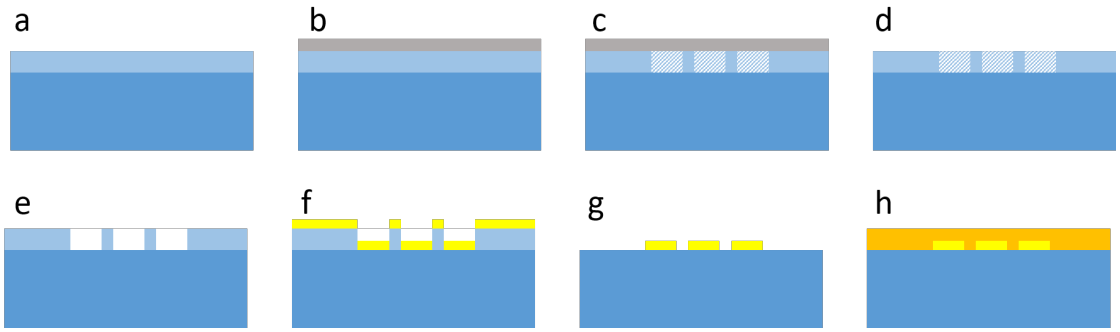

Figure 4.4: Steps for fabrication of nonlinear metasurface. a) Spin coat A2 PMMA. b) Deposit 5 nm chromium on top of PMMA by electron beam deposition. c) Expose metasurface pattern by electron beam lithography. d) Remove chromium layer by etching in CR-7 wet etchant. e) Develop PMMA resist in IPA-MIBK solution. f) Deposit 2 nm chromium (as an adhesion layer) followed by 30 nm gold by electron beam evaporation. g) Remove excess gold in liftoff process by dissolving PMMA in hot acetone. h) Spin PFO polymer on top of sample at 3000 rpm for 1 minute.

then placed in a 5 mL syringe. A 13 mm polytetrafluoroethylene syringe filter with 0.22 micron pores was attached to the tip and the solution was filtered through it into a clean 5 mL amber vial to remove any undissolved PFO.

Immediately before spin coating, the PFO solution was heated at 80° C on a hot plate for 30 minutes. A glass transfer pipette was used to coat the sample in the PFO solution, which was then spun at 3000 rpm for 60 seconds. The completed sample was stored in a vacuum desiccator before measurement.

4.4 Optical Measurements

The transmission spectra of the nanobar arrays were measured by Fourier transform infrared (FTIR) spectroscopy, shown in figure 4.5. PFO has a peak nonlinear efficiency at 1250 nm, so the absorption peak should be close to that for maximum nonlinear signal. According to theoretical calculations, the nanobars should be 240 nm long to achieve this resonance. In practice though, nanobars of this size had a resonance peak at 1400 nm. In order to achieve the desired resonance, the size of the nanobars was reduced to 205 nm in length and 50 nm in width. This is most likely due to differences in the dielectric environment of the nanobars in the actual sample compared with the simulation, which can have a large effect on the resonance.

The nonlinear response of the PFO was measured by exciting a patch of the sample with no nanobars with a 1250 nm pump laser. The transmitted light passed through a 410 nm bandpass filter with a full width half maximum (FWHM) pass band of 10 nm. The third harmonic light could be easily collected with a CCD detector. Spectral information about

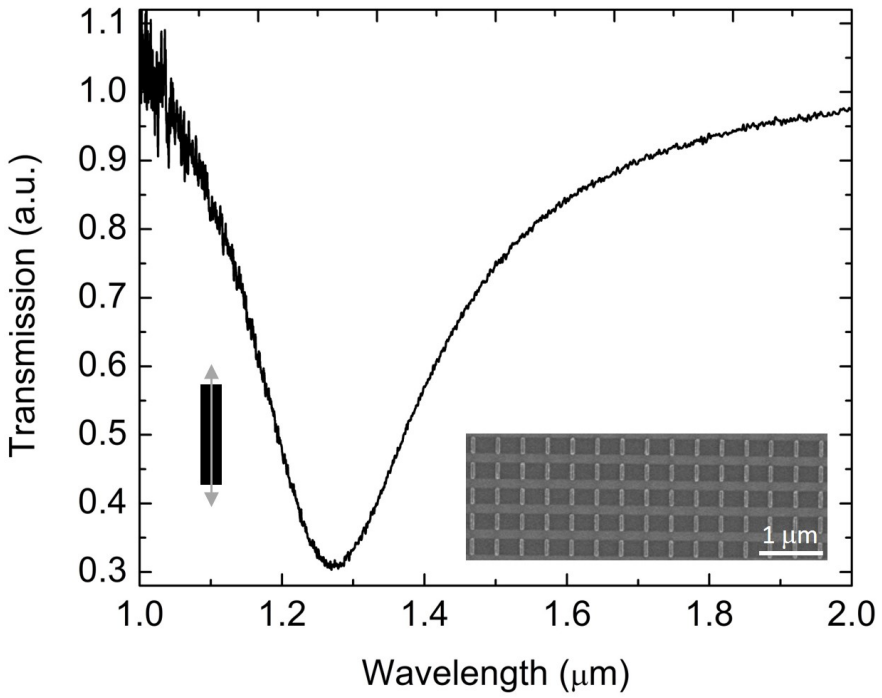

Figure 4.5: Transmission spectrum for array of vertically oriented nanobars 205 nm long and 55 nm wide measured by FTIR (Brüker). An integrated microscope and detector allowed focusing on a single 60 μm square sample Left inset shows orientation of linear polarization in relation to nanobars. Transmission for cross polarized light is 1 for this spectral range Right inset shows SEM micrograph of sample.

both the fundamental and the third harmonic was collected in a spectrometer. Both the CCD image of the third harmonic and the spectrum are shown in figure 4.6.

Measurements are taken using a 1230 nm laser at 20 mW. The sample used for all measurements has 12 discrete levels of phase delay, meaning the unit cell contains 12 nanobars at different orientations. The first measurement, a repetition of previous results, is necessary to ensure that the metasurface is working as intended for the fundamental frequency as well as the third harmonic. Because circularly polarized light undergoes a reversal of handedness due to reflections and phase delays, and the metasurface interacts differently with right-handed circularly polarized (RCP) light and left-handed circularly polarized (LCP) light, it is necessary to measure both polarizations independently. The total phase accumulated due to the metasurface depends on both the incident and transmitted polarization as well as the nonlinear harmonic according to equations 4.8 and 4.9.

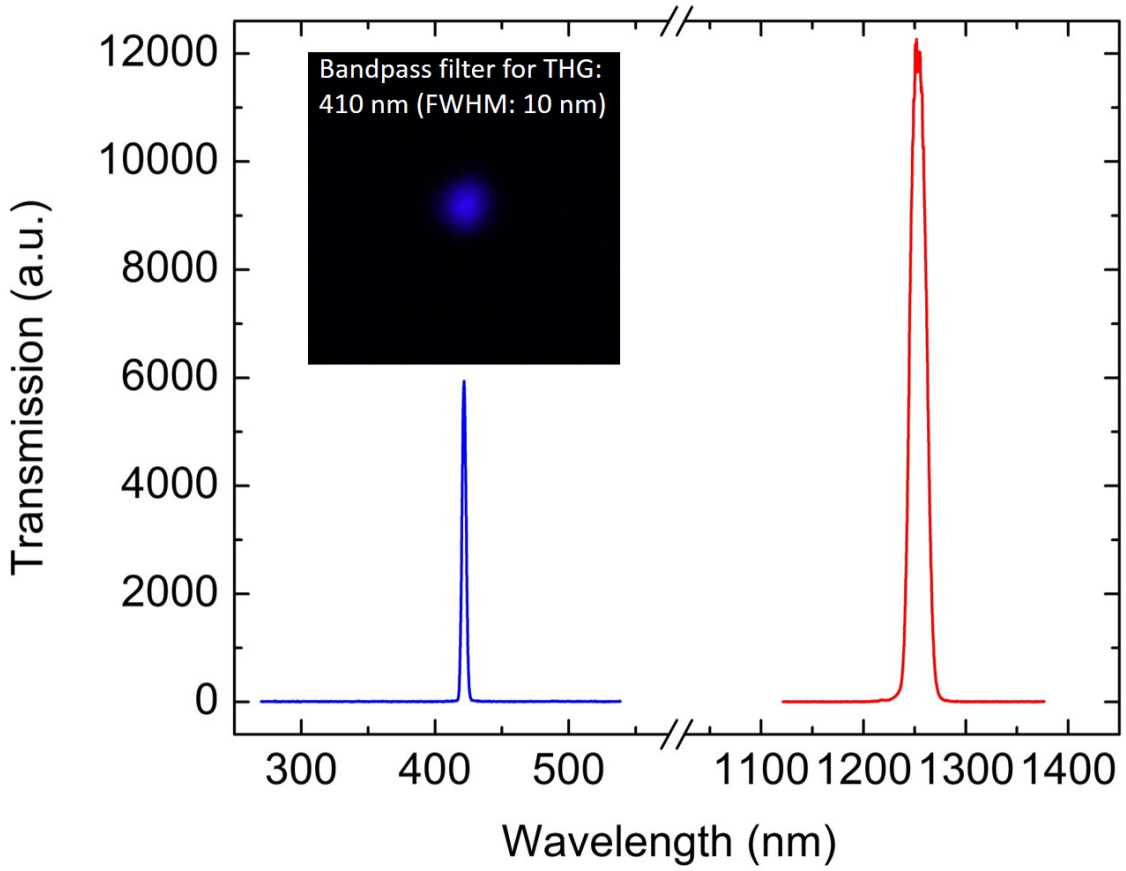

Figure 4.6: Spectrum of fundamental frequency and third harmonic generated by PFO film transmitted through the sample. The film is excited by a 1250 nm pump laser, and the fundamental and third harmonic are separated by a 410 nm bandpass filter. The inset shows the third harmonic light measured directly by a CCD detector.

For opposite incident and refracted polarization:

$$\phi_{g_{\sigma,-\sigma}} = (n+1)\sigma\theta \tag{4.8}$$

For the same incident and refracted polarization:

$$\phi_{g_{\sigma,\sigma}} = (n-1)\sigma\theta \tag{4.9}$$

Where ϕ_g is the geometric phase accumulated due to the metasurface, σ is the polarization, 1 for RCP and -1 for LCP, $n = \frac{\lambda_1}{\lambda_2}$, the nonlinear harmonic generated, and θ is the angle of the nanobar.

These equations give us some key information about how the metasurface affects light. First, we can see that for the fundamental frequency, ($n = 1$), only the polarization reversed light is affected. For light whose polarization stays the same, there is no additional phase accumulation and the light will not be deflected by the metasurface. For the polarization reversed light, there is additional phase accumulation, so the light ray will be deflected, and the direction of the phase gradient, and therefore the direction of deflection, will be opposite for RCP and LCP light. For all combinations of excitation and detected polarization, four measurements are required. Figure 4.7 shows the deflection of the fundamental frequency at normal incidence to the metasurface. As predicted by the theory, light detected with the same polarization as the excitation does not deflect at all, while light detected with the opposite polarization as the incident light deflects to one side or the other, depending on the initial polarization.

For the third harmonic light, both the reversed and nonreversed polarization see additional phase accumulation, but the accumulation is greater for the polarization reversed case. This means we should expect to see greater deflection of the light ray for the reversed polarization, but some deflection will occur in both cases. The results in figure 4.8 agree with the theory, showing deflection to the right for RCP incident light, with greater deflection of transmitted LCP than RCP, and deflection to the left for LCP incident light, with greater deflection of transmitted RCP than LCP.

Generalized Nonlinear Snell's Law

To observe the generalized Snell's law and asymmetric transport, it is necessary to be able to control the angle of of incidence of the light with the metasurface as well as determine the angle of refraction by measuring the deflection of the beam. To control the angle of incidence, the numerical aperture of the objective was used. The laser was demagnified so that its spot was much smaller than the aperture of the objective. A mirror was attached to a movable stage so that the laser spot could be deflected radially away from the central axis of the objective. As the spot was deflected further from this axis, the angle of incidence onto the sample increased. According to the geometry in figure 4.9, it is easy to calculate the angle as a function of the objective's focal length and the offset of the incident beam from the lens's central axis. This relation is shown in equation 4.10.

$$\theta = \arcsin \frac{s}{f} \tag{4.10}$$

Where θ is the incident angle, s is the radial offset distance of the incident beam, and f is the objective's focal length.

The angle of refraction could be calculated by measuring the deflection of the laser spot after passing through the sample to the imaging objective. The setup also contained various quarter wave plates, polarizers, and filters to obtain and measure the proper circular polarization and to separate the fundamental frequency from the third harmonic. A diagram and photograph of the setup are shown in figure 4.10.

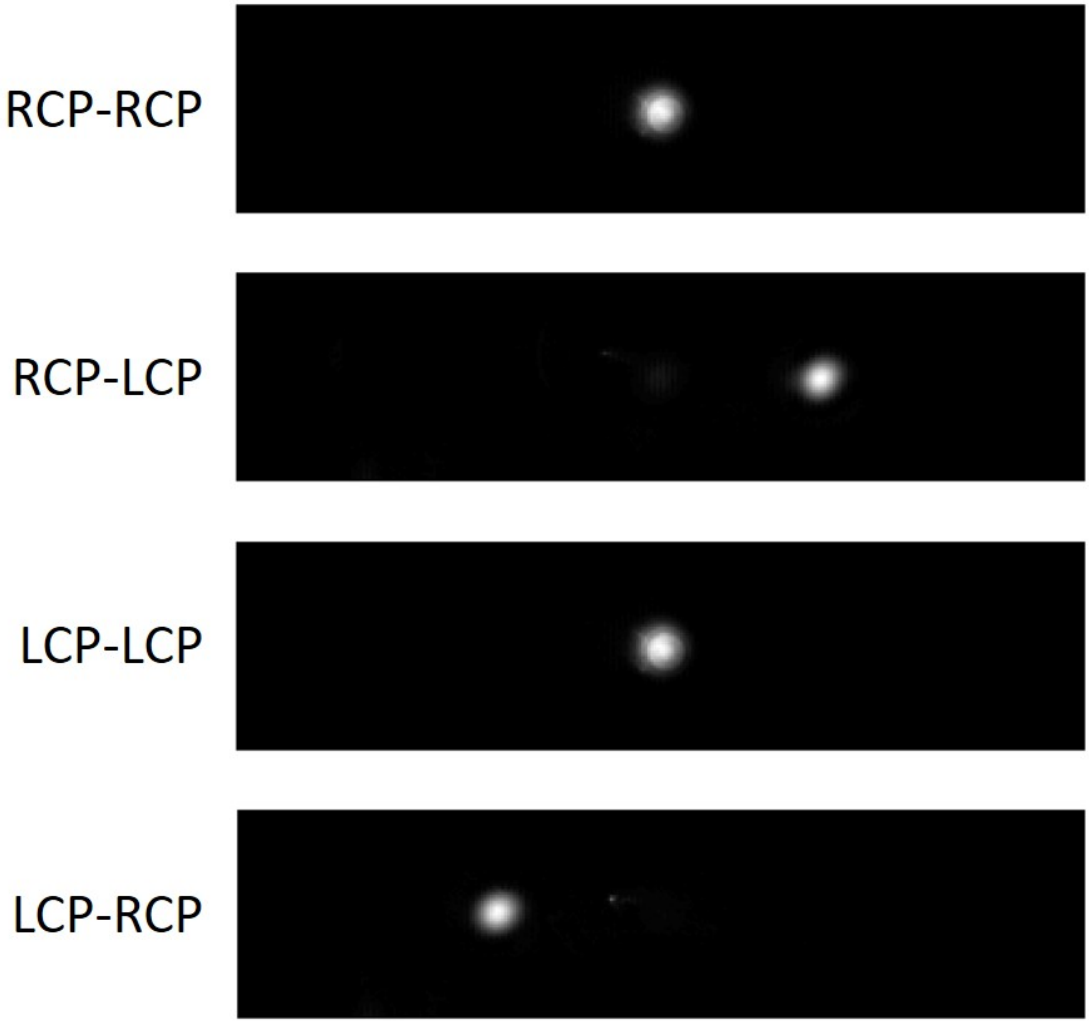

Figure 4.7: Deflection of transmitted light which passes through the metasurface at normal incidence. These results agree with the theory described by equations 4.8 and 4.9.

Figure 4.8: Deflection of third harmonic light generated by the metasurface with incident light at normal incidence. These results agree with the theory described by equations 4.8 and 4.9.

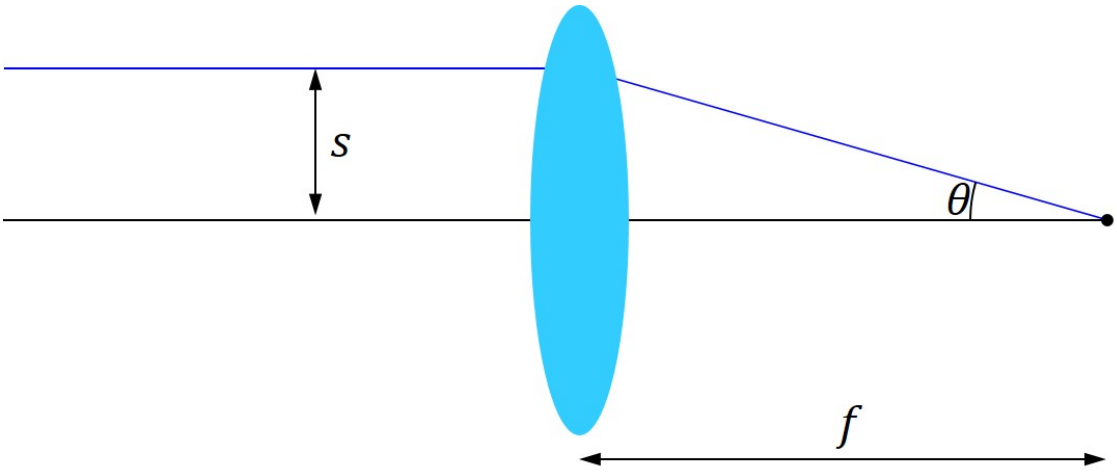

Figure 4.9: Controlling the incidence angle by offsetting the incident beam radially in the focusing objective. Offsetting the beam does not change the location focus spot, which is set by the focal length of the objective, so the metasurface can remain in focus as the angle is changed.

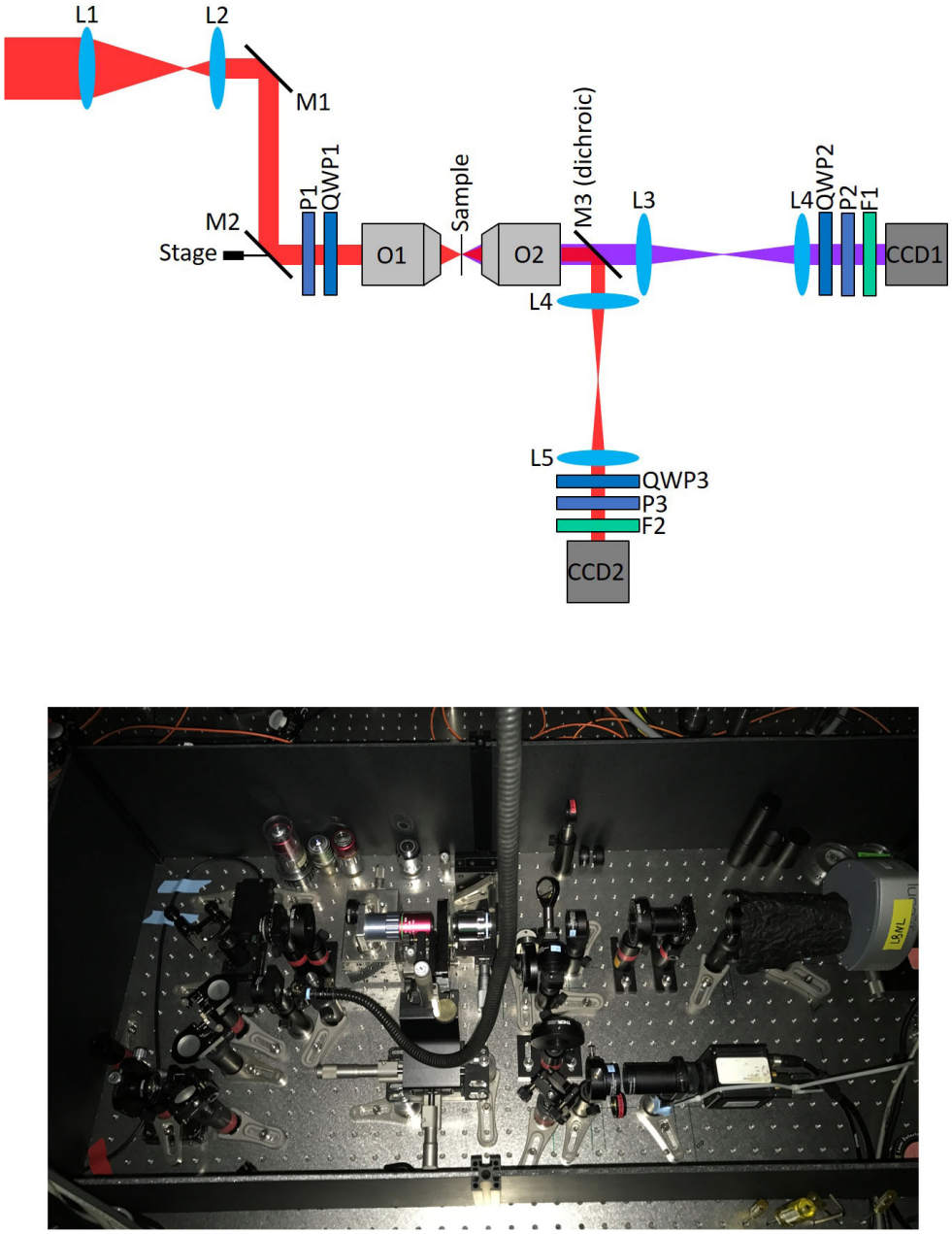

Figure 4.10: (Top) Schematic of optical setup for measuring angle of refraction of both fundamental and third harmonic frequency light as it passes through the metasurface sample. (Bottom) Photograph of setup.

To confirm the theoretical calculation of the generalized nonlinear Snell's law, the angle of refraction was measured for an incidence angle range of $\pm 17.5°$. The available range of incidence angles is determined by the numerical aperture of the focusing objective. This measurement was performed for each of four different combinations incidence and measured polarization for both the fundamental frequency and the third harmonic frequency, for a total of 8 measurements. The RCP→RCP and LCP→LCP measurements for the fundamental frequency are degenerate, so 7 sets of data with their accompanying theoretical calculations are included in figure 4.11. At first glance, it may seem counterintuitive that the angle of incidence and angle of refraction should be the same for both the RCP→RCP and LCP→LCP cases, as the light still exhibits refraction as it goes through the sample, whose refractive index is greater than air. However, the angle of refraction is not measured inside the sample, but after it exits the sample back to air, so even though light that enters the sample at an angle other than normal incidence will refract inside the sample and will therefore be offset upon leaving the sample, the refraction that occurs when it leaves the sample is opposite what occurs when it enters so the overall effect is that the angle of incidence and refraction are the same. This is not true for any of the other six cases, where the phase gradient imparted by the metasurface results in additional refraction that is not accounted for just by the index changes as the light passes through the sample.

Asymmetric Transport

To exhibit asymmetric transport, the propagation of light through the metasurface should not be the same as the time reversed propagation. Because it is not practical to actually reverse the direction of propagation through the optical setup, the time reversal operation requires three steps. First, the sample itself is flipped so that incident light hits the other side. Second, the refraction angle from the first case is used as the incident angle in the time reversed case. Third, the measured polarization in the first case is used as the incident polarization in the time reversed case. By plugging these transformations into equation 4.6 we can compare the incident angle in the first case to the refraction angle in the time reversed case. If the transport is symmetric, then these will be the same, while for asymmetric transport, they will not. For the fundamental frequency, symmetric transport is expected for all polarization cases. For the nonlinear case, transport is symmetric when the incident polarization and measured polarization are opposite (RCP→LCP and LCP→RCP). When the incident and measured polarization are the same (RCP→RCP and LCP→LCP), however, the lack of reversal of the sign of σ means that we are left with equation 4.11, which shows that we expect asymmetric transport.

$$\sin\theta_{t_2} = \sin\theta_{i_1} + \frac{\lambda_2}{\pi n_i}(n-1)\sigma_1\frac{d\theta}{dx} \tag{4.11}$$

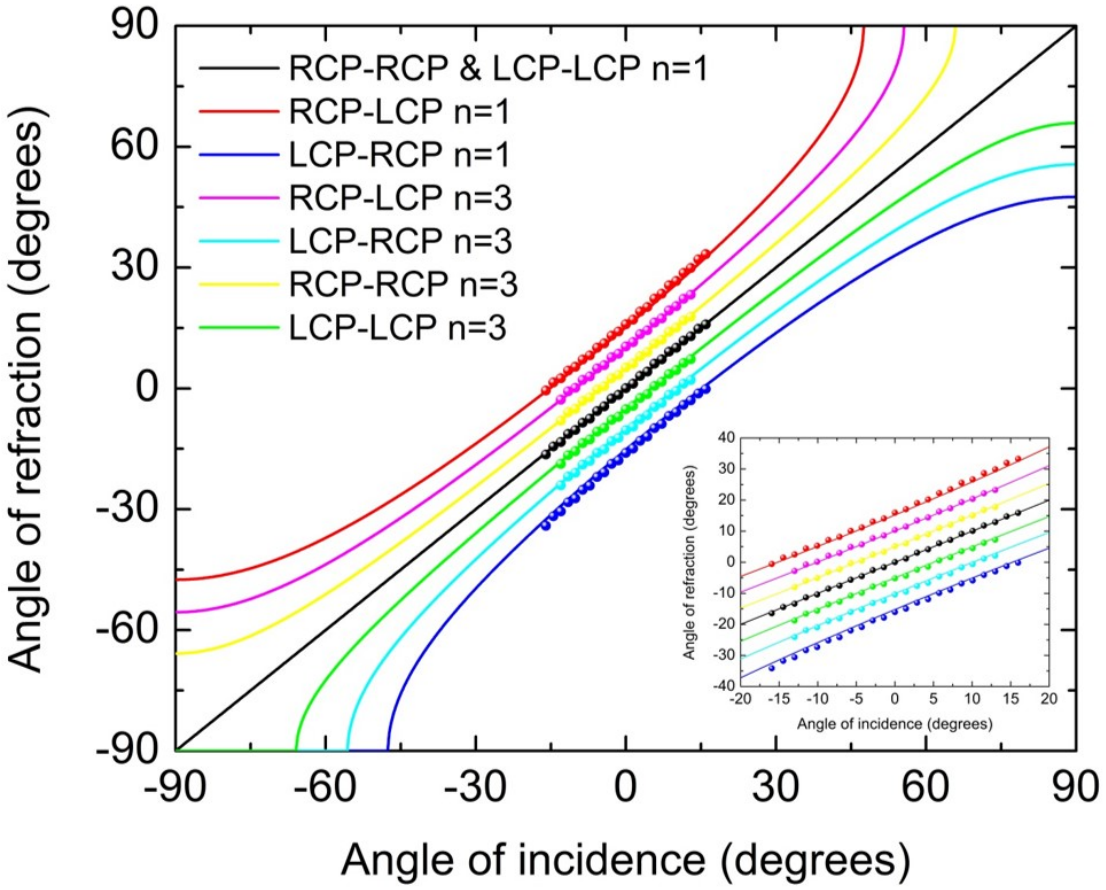

Figure 4.11: Experimental measurement of generalized nonlinear Snell's law showing strong agreement with theoretical calculations. Results are shown for all four combinations of incident and transmitted polarization for the fundamental and third harmonic frequencies. Solid lines show theoretical calculations, and dots show experimental measurements.

4.5 Conclusions and Outlook

In this chapter, we derived a generalized form of Snell's law of refraction that accounts for refraction of nonlinear light generated at an interface. We fabricated samples that use Pancharatnam-Berry phase to cause circularly polarized light to accumulate phase with a spatial gradient and measured light refraction through these samples to experimentally verify the derived refraction equation. We then used the same samples to demonstrate asymmetric transport for certain polarizations of light, which was predicted through mathematical time-reversal of the refraction equation. This was the first demonstration of asymmetric transport using a metasurface.

The demonstration of asymmetric transport has the potential for widespread application,

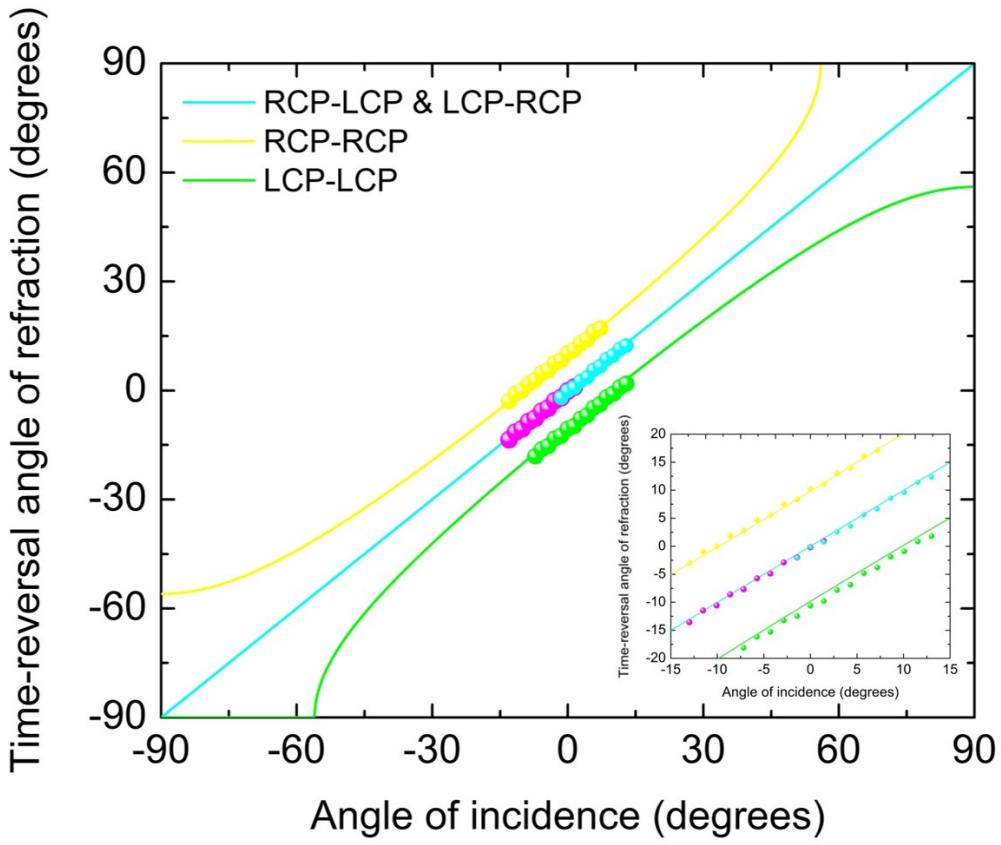

Figure 4.12: Time reversal of third harmonic frequency light generated by metasurface. The angle of incidence is compared with the angle of refraction for all four polarization scenarios. The solid blue line represents symmetric transport, where the angle of incidence and the time reversed angle of refraction are the same. Results agree closely with theory, showing that when the incident and measured polarization are opposite, symmetric transport occurs, but when they are the same asymmetric transport occurs. The full range of angles could not be measured for the polarization reversed cases due to asymmetry of the optical setup which limited the incidence angles that could be applied to the system more than the refracted angles that could be measured.

especially in integrated photonics. Asymmetric transport in electrical systems is the basis upon which all electronics work, and the difficulty in designing such systems has been a major limiting factor in photonics. Optical systems exhibiting asymmetric transport usually require large pieces of nonlinear crystals for light to pass through, which is expensive, incompatible with integrated photonics, and leads to phase matching problems which can limit the utility of the technique. The results shown here are an important step towards the practical application of on-chip optical elements such as diodes and modulators, which are necessary to bring the advantages of optics to areas previously confined to electronic systems.

Chapter 5

Patterning Colloidal Quantum Dots

5.1 Introduction

Quantum dots are semiconductor nanocrystals that are small enough that quantum confinement alters their electronic and optical properties, leading to properties that differ from bulk materials. Because the properties of the quantum dots are caused by this quantum confinement, the properties can be controlled by controlling the size of the particles. There are two broad categories of quantum dots based on their synthesis method. Epitaxial quantum dots a fabricated by epitaxially growing multilayer structures of different semiconductor materials, which, due to strain caused by lattice mismatch between the two materials, self-assemble into nanoscale islands, resulting in quantum confinement. These epitaxial quantum dots are permanently embedded in high index semiconductors. They tend to have high internal quantum efficiency due to the high purity and cleanliness of their constituent materials and ultra high vacuum epitaxial growth, which maintains the crystal structure of the substrate, but their external quantum efficiency is low due to the difficulty in extracting photons from the high index substrate. Colloidal quantum dots are synthesized in wet chemical processes, which allows them to be fabricated more quickly and cheaply than epitaxial quantum dots. Typically, colloidal quantum dots are less efficient than epitaxial ones due to surface effects and defects introduced by the synthesis or upon exposure to the environment. Recent work focusing on synthesizing cadmium selenide (CdSe) quantum dots with cadmium sulfide (CdS) shells to mitigate surface effects has resulted in colloidal quantum dots with quantum efficiency near unity [120].

Another type of quantum dot that has been the subject of much recent attention is cesium lead halide perovskite quantum dots [121–123]. By using chlorine, bromine, and iodine in different ratios as the halide, the emission can be continuously tuned across the entire visible spectrum. These materials are also much more robust to surface defects than more common compound semiconductor quantum dots. Perovskites have shown promise in photovoltaics [124] and as light emitters [125]. They are limited mainly by their poor environmental stability; their optical performance degrades rapidly in air.

Due to their optical properties, quantum dots have been used extensively in biological imaging, sensing [126], photovoltaics [120], and optoelectronics [127–132]. Because they can serve as single photon emitters, they have also been researched for use in quantum communication and computing [133, 134].

5.2 Quantum dots as a single photon source

In order to realize functional systems utilizing quantum emitters, a system capable of emitting single photons at room temperature on demand with high efficiency and indistinguishability that can also be integrated with standard semiconductor fabrication is necessary. No current systems are capable of meeting all of these criteria simultaneously. Although the physics of such two level light-emitting systems is well understood, the complex environments in which they reside leads to many practical issues which limits the integration of such emitters into functional devices. Epitaxial quantum dots yield high quality and pure single photons, but their efficiency is very low due to the difficulty in extracting the photons, and the devices can not easily be integrated with optical systems [135, 136].

Colloidal quantum dots are an attractive system for generation of single photons [137–140]. Recent work in perovskite quantum dots has shown them to be promising as single photon emitters in addition to other advantageous properties such as easy emission tunability and surface defect tolerance. However, the difficulty in controlling the location of individual quantum dots and integrating them into further processing steps, as well as their tendency to degrade over time, has limited their use in such systems.

Here, a simple method for controlling the location of quantum dots, which improves their optical stability and is compatible with further microprocessing steps, is demonstrated. This technique is applicable to any quantum dots, including more complicated structures such as quantum rods and tetrapods. We demonstrate it with highly efficient CdSe/CdS core shell quantum dots and $CsPbBr_3$ perovskites. In this method, quantum dots are dispersed in PMMA electron beam resist and then spin coated onto a sample. The PMMA film containing the quantum dots is then patterned by electron beam lithography in order to isolate quantum dots at the desired location on the sample. By controlling the density of quantum dots dispersed in the resist as well as the size of the patterned region, it is possible to fabricate samples with quantum dots optimized for a variety of applications. It is also possible to apply this method to samples that already have structures on them. The high precision of electron beam lithography allows placement of the quantum dots in alignment with features, such as antennas or cavities, on the sample.

5.3 Sample Preparation

Fabrication of these samples involves two steps. First the quantum dots are dispersed into PMMA. Then the PMMA films with embedded quantum dots are patterned by electron beam

lithography. Commercial A2 PMMA (Microchem) was used. A2 PMMA coatings typically has a thickness between 80 and 120 nm. In order to more precisely control the location of the quantum dots, the PMMA was diluted with anisole (methoxybenzene) at at a 1:1 ratio, reducing the viscosity and giving a layer thickness of 30 nm when spun onto a sample at 2000 rpm. This diluted PMMA was then mixed with various quantum dots, particularly CdSe/CdS core shell quantum dots with emission peaks at 620 nm and inorganic lead halide perovskite quantum dots with emission peaks at 500 nm. Perovskite quantum dots were fabricated according to a process reported in the literature [121, 141], which involves injecting hot cesium oleate solution into a 3-neck flask containing $PbBr_2$. The quantum dots were then purified and isolated by adding hexane and centrifuging. A postsynthetic surface treatment of thiocyanate was used to remove excess ligands to improve optical performance. CdSe/CdS quantum dots were synthesized following published procedures [120, 142].

The quantum dots were diluted to various degrees in toluene before being mixed into the PMMA. The PMMA containing quantum dots was spun onto silicon wafers at 2000 rpm and then baked at 180° C to evaporate any remaining solvent. To further control the position of the quantum dots as well as to improve the quality of the patterning, a layer of this diluted PMMA without quantum dots was often spun onto the samples before the layer containing quantum dots. The emission of these embedded quantum dots was then measured by confocal microscopy for comparison with emission after patterning.

The doped films were then patterned by electron beam lithography. For patterns larger than 500 nm, a Quanta 200 SEM (FEI) with an electromagnetic beam blanker installed in the column and with the NPGS software for controlling the stage and beam was used. For higher resolution patterning, a 50 kV electron beam lithography tool (Crestec) was used. Typical patterns consisted of 500 nm square pillars of PMMA containing quantum dots with concentrations from hundreds of quantum dots in each pillar to a single quantum dot depending on the dilution.

5.4 Optical Measurements

Photoluminescence of the quantum dot samples was measured in a confocal scanning microscope (Wytek) both before and after patterning. Minimal degradation of luminescence was seen due to patterning or time. Patterned regions can be seen clearly in the photoluminescence measurements.

For samples without an additional undoped spacer layer of PMMA, the contrast between the pattern and background was smaller and quantum dots could still occasionally be seen sticking to the substrate. For very thin layers of PMMA, this effect was more pronounced, indicating that quantum dots in direct contact with the substrate are not removed even after the PMMA in which they are embedded has been removed. Even a thin spacer layer prevents direct contact between the quantum dots and the silicon substrate, so they will not stick after the PMMA is removed.

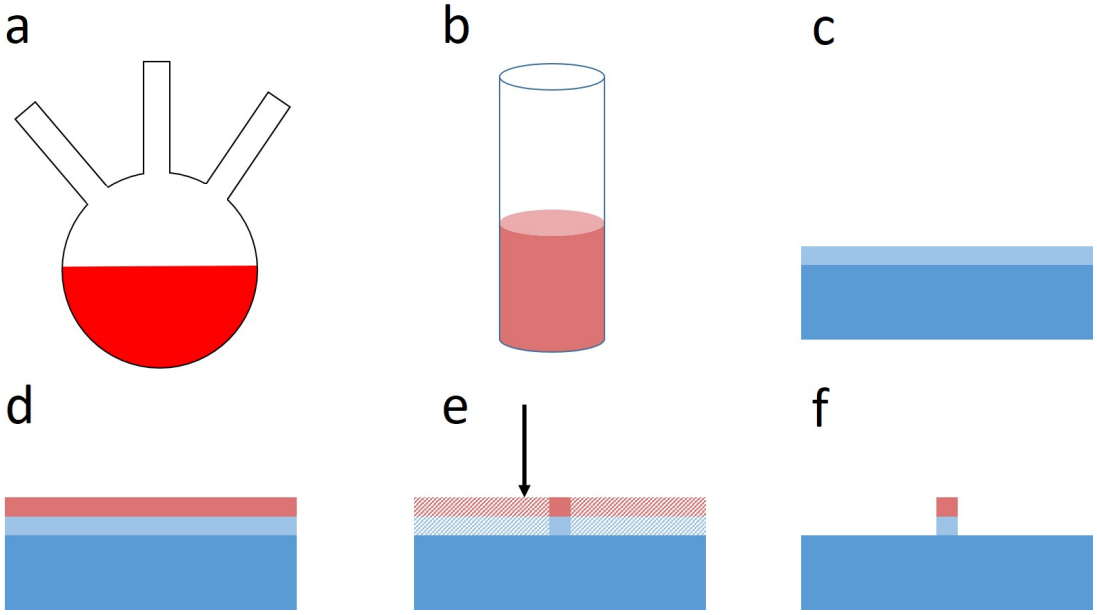

Figure 5.1: Fabrication process for patterning and isolating quantum dots. a) Synthesize quantum dots by standard method in literature. b) Add quantum dots to electron beam resist in desired concentration. c) Spin undoped resist on substrate as spacer layer. d) Spin resist with quantum dots. e) Pattern resist with electron beam lithography. f) Develop pattern to leave structure containing quantum dots.

For CdSe/CdS quantum dots, single photon emission from quantum dots isolated in pillars was confirmed. This was done using a Hanbury Brown and Twiss type correlation measurement setup to measure the $g^{(2)}$ correlation of photons emitted by the sample. In this setup, light from the photon source enters a beamsplitter and is divided into two equal paths. At the end of each path is an avalanche photodiode (APD) detector, which allows detection of even extremely weak signals. These two detectors are connected to electronics which measure the delay between the detection at one detector and the other. To determine the purity of single photons, the probability of detecting a photon at the second detector is plotted as a function of delay time after a photon is detected at the first detector. For single photon emission, there should be a sharp dip at a delay time of zero, as the quantum emitter should not emit two photons at the same time. In figure 5.4. the sharp dip at $\tau = 0$ shows that photons do not arrive with very short delay times, meaning that the sample emits single photons. The other oscillations on the order of 10 ns are caused by the pulsed laser excitation, and indicates that the photoluminescence lifetime is shorter than the pulse frequency of the laser. Experiments are ongoing to measure single photon emission from patterned perovskite quantum dots.

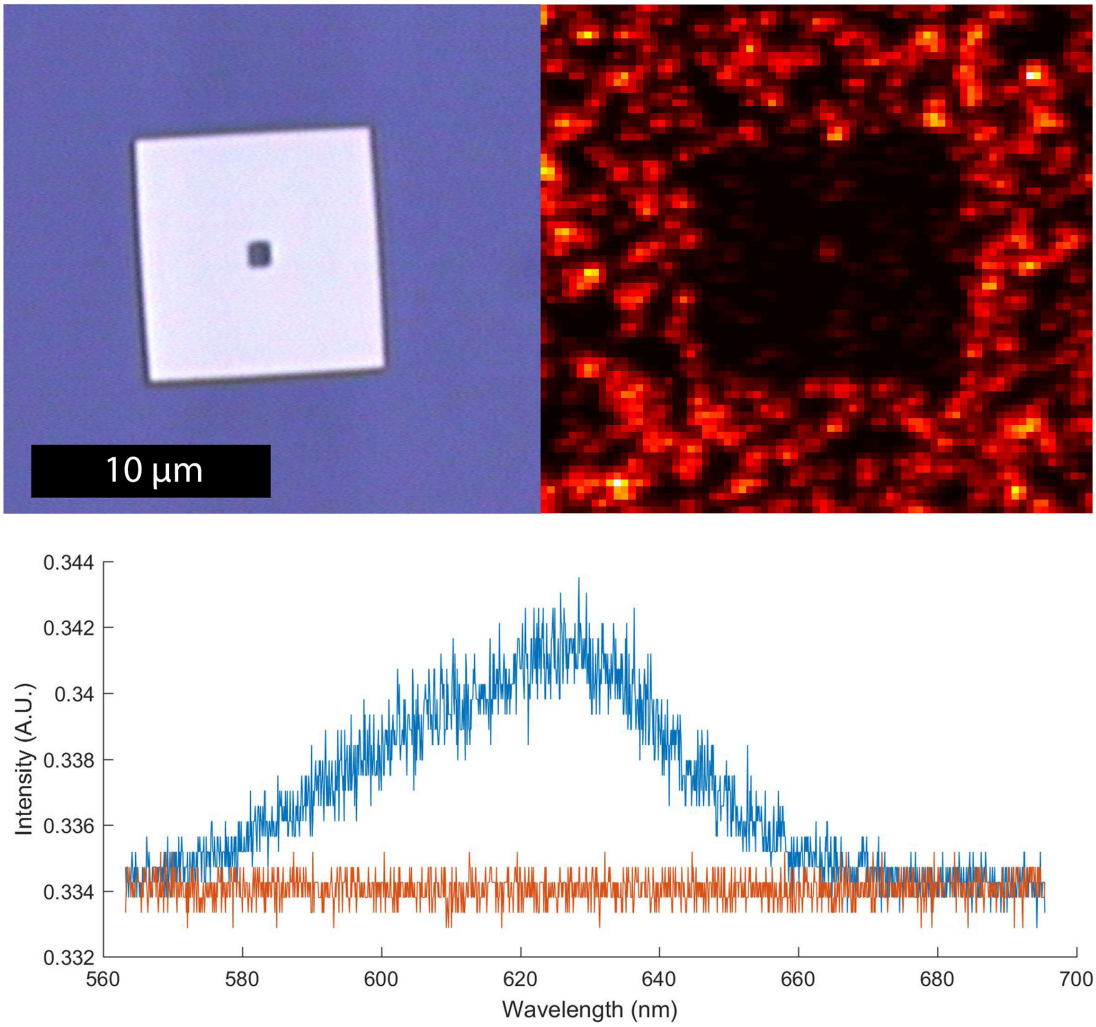

Figure 5.2: Bright field microscope image and confocal scanning fluorescence image of patterned PMMA with embedded CdSe quantum dots. The pattern consists of a square patch 10 μm on a side with the PMMA and quantum dots removed, with a 1 μm square in the center where the PMMA and quantum dots remain. The spectrum shows the strong contrast between the area containing quantum dots and the background, where no characteristic emission at 620 nm can be seen.

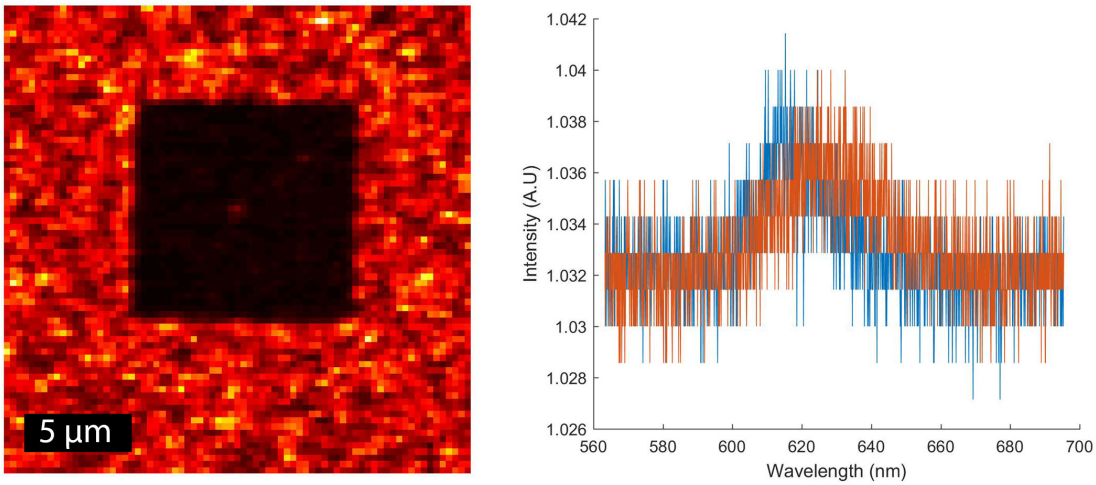

Figure 5.3: Fluorescence image of patterned quantum dot film with photoluminescence spectra of several points. The blue curve in the spectrum is taken from the patterned pillar, and the red curve is from a spot in the background where there should be no quantum dots. Identical emission at 620 nm characteristic of the quantum dots can be seen in both, indicating that quantum dots are sticking to the background after patterning. This was prevented in other samples by including a spacer layer between the substrate and the PMMA layer with quantum dots.

5.5 Conclusion and Outlook

Using this technique, we were able to clearly select areas on a sample to contain quantum dots or to be clear of quantum dots using electron beam lithography. By controlling the density of quantum dots and the pattern size, we could isolate individual or small groups of quantum dots. This technique can be used by isolating a single quantum dot for quantum optical devices, or it can be used with clusters of dots for more classical integrated photonics applications.

This method can be used for integrated photonic devices in several ways. The simplest is to first design and fabricate a device that requires quantum dots at a particular location and use this patterning technique to place the light emitters only where they are required. This could be easily used to couple quantum dots to antennas or cavities for enhancement of spontaneous emission [143] or directional control of emission, both of which have important applications in integrated photonics [144–152].

To use this technique for more complicated devices in which the quantum dot is first isolated on the substrate and the device is then fabricated around it, some modifications to the described technique would be required. One way to enable such processing would be to embed the quantum dots in a crosslinking negative resist such as hydrogen silsesquioxane (HSQ). HSQ is an electron beam and extreme UV resist, which, after exposure, has a compo-

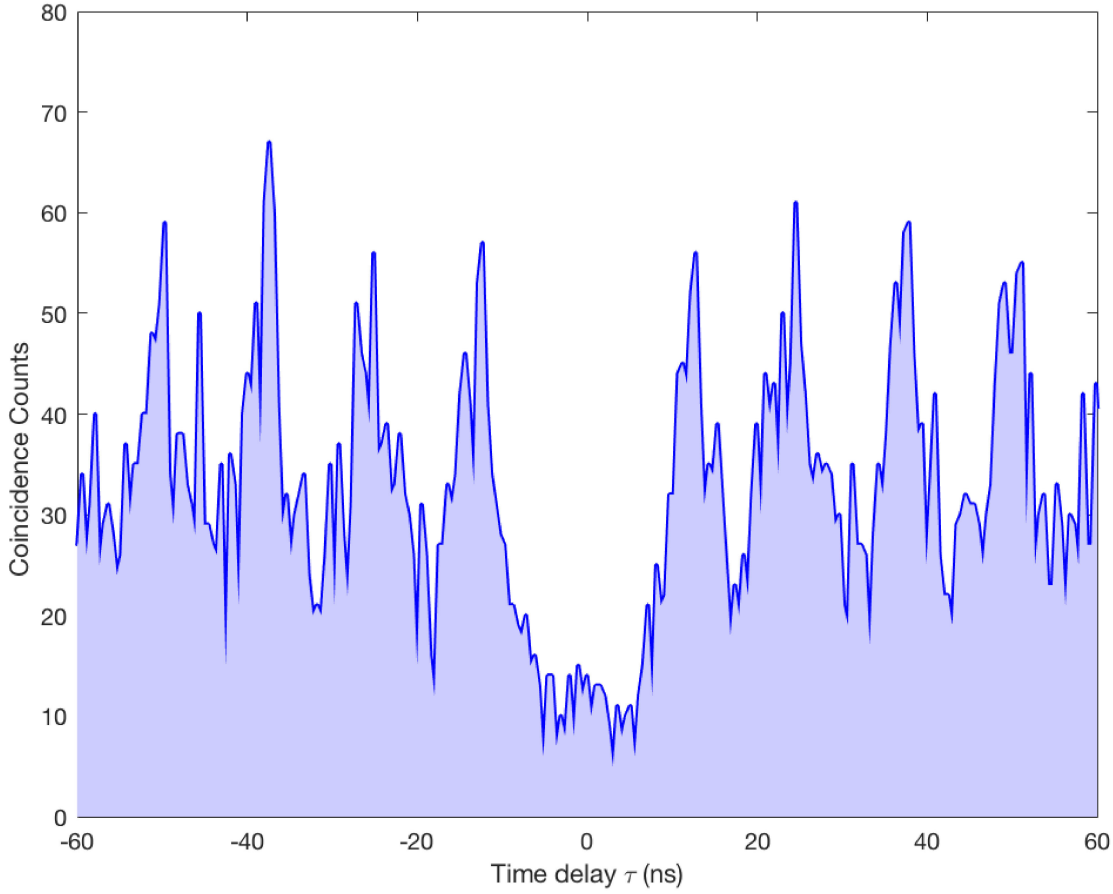

Figure 5.4: Photon correlation measurement from patterned CdSe quantum dot. The characteristic single photon emission, which can be seen by the dip at $\tau = 0$ indicates that the fabrication method isolates single quantum dots.

sition similar to silicon dioxide, making it compatible with a large variety of nanofabrication processes.

For photonic devices that work by manipulating the phase of light in order achieve the desired effects, such as metasurfaces, it is necessary to control the orientation of each quantum dot in relation to the device it is coupled to in addition to just the location. This introduces many further complications to device fabrication, but this technique of patterning the polymer film in which the emitters are embedded offers solutions to this issue that are not available for emitters placed by other techniques such as chemical functionalization.

Chapter 6

Conclusion

6.1 Summary

In this dissertation, we discussed the growing field of integrated photonics and introduced several techniques and devices that can be used to address major areas of need. Integrated photonics could lead to advances in computing, with photonic elements replacing or complementing electronic components, and in medicine, where on-chip devices could replace complicated diagnostic equipment. This could lead to greater access to medical care as well as improved medical care with individually tailored diagnostics and treatment. To realize such integrated systems, photon sources, photon control optical elements, and photon detectors that are nanoscale and compatible with electronics fabrication techniques are required. Here we demonstrate novel photon control elements that manipulate phase and refractive index for various applications and a technique for integrating photon sources with any of a large variety of optical elements.

After a brief background of integrated photonics and metamaterials along with the fundamental basis in optics upon which the rest of the work stands, we introduce the concept of transformation optics as a design method for optics with a high degree of control and flexibility. We show how such devices can be realized using gradient index optical materials. The difficulty in fabricating large scale gradient index materials with large Δn has limited the practical application of such devices. The photoelectrochemical etching method that we developed is a large-scale and high-throughput method for fabricating arbitrary gradient index devices with $\Delta n \approx 1$ from porous silicon. This is the first demonstration of photopatterning in p-type porous silicon. We use this method to fabricate gradient index waveguides, ideal optical concentrators, and phase masks.

The next two sections focus on using optical nonlinearity to manipulate light. First, we apply the concept of dynamic self-assembly, which uses thermodynamic non-equilibrium to create order, to optics. We use this method to design a distributed Bragg reflector with thermally isolated layers that dynamically adjusts the index of each layer by the thermo-optic effect in response to excitation in order to tune its bandgap and heal defects. We fabricate

this device in silicon by etching fins perpendicular to the substrate, with air in between, to get maximum index and absorption contrast as well as thermal isolation between the layers of the Bragg reflector.

Next, generalized laws of nonlinear reflection and refraction are derived and demonstrated using a metasurface to manipulate the phase of the third harmonic frequency of the incident light. Metasurfaces, subwavelength arrays of resonant optical antennas which directly impart phase gradients to incident light, have recently been used to replace conventional optical elements such as objective lenses, as phase masks for holography, as an ultrathin invisibility cloak, and for many other applications. Here, we use the additional effects of nonlinearity to demonstrate asymmetric transport of light through a metasurface. Asymmetric transport is critical to electronics, and is necessary in photonics if such electronic elements are to be replaced with photonic ones.

In the final section, we address the issue of nanoscale integrable photon sources. Quantum dots have excellent properties as emitters, but their integration has been a challenge. Epitaxial quantum dots require special compound semiconductor substrates with multiple quantum wells, restricting any other components to these same substrates, making integration impractical. Colloidal quantum dots, synthesized in solution, have more potential for integration. In most cases, though, they are just spin-cast onto a surface or require chemical functionalization, which can limit its use in complicated structures requiring many prior and subsequent steps. The method demonstrated here involves embedding the quantum dots at a controlled density in electron beam resist material, spinning the resist with controlled thickness, and patterning using electron beam lithography. This method offers precise control of the location of quantum dots, can be used with any variety of colloidal quantum dots with different properties, and can be integrated on any substrate with most standard fabrication techniques. Clusters of quantum dots can be used as a classical light source, and individual quantum dots can be isolated for use as single photon emitters for quantum optics applications.

6.2 Future Research Directions

There are many opportunities for further work on the topics discussed here. We demonstrated two dimensional gradient index devices with porous silicon by projecting a pattern on the surface of the silicon during the electrochemical etching. The etching conditions were then kept constant. By varying the etching conditions temporally in addition to the spatial variation, three dimensional gradient index devices could be fabricated, which have not been demonstrated by any other technique. Further exploration of the use of porous silicon as a phase mask is also warranted. Demonstrations of computer generated holography use a single layer phase mask, which can be fabricated in a number of ways. Porous silicon can be used to make multilayer CGH phase masks, which could improve the hologram efficiency. It could also be used for rapid fabrication of aspherical optical components.

We demonstrated control of the position of quantum dots using electron beam lithography

and quantum dots embedded in PMMA polymer resist. In order to make this process compatible with further processing steps including wet chemistry processing, a different resist is required. Using HSQ resist, the quantum dots could not only be localized with better precision, but could be then used in most standard nanofabrication processes.

We have demonstrated several techniques and devices that lend themselves to integrated photonic devices, but we did not actually integrate any of them. One particularly interesting example of how these elements might be integrated is to pattern quantum dots on a metasurface, which could interact with the light from the quantum dot in a number of ways. Quantum dots could also be integrated with nanocavities to enhance their spontaneous emission, with nanoantennas to control the direction and polarization of their emission, or with waveguide structures, including gradient waveguides.

Bibliography

[1] Bo Lojek, ed. *History of Semiconductor Engineering*. New York: Springer, 2007.

[2] Gines Lifante. *Integrated Photonics Fundamentals*. San Francisco: Wiley, 2003.

[3] Jennifer A. Dionne, Luke A. Sweatlock, Matthew T. Sheldon, A. Paul Alivisatos, and Harry A. Atwater. "Silicon-based plasmonics for on-chip photonics". In: *IEEE Journal of Selected Topics in Quantum Electronics* 16.1 (2010), pp. 295–306.

[4] David Thomson, Aaron Zilkie, John E. Bowers, Tin Komljenovic, Graham T. Reed, Laurent Vivien, Delphine Marris-Morini, Eric Cassan, Elopold Virot, Jean-Marc Fedeli, Jean-Michel Hartmann, Jens H. Schmid, Dan-Xia Xu, Frederic Boeuf, Peter O'Brien, Goran Z Mashanovich, and M. Nedeljkovic. "Roadmap on silicon photonics". In: *Journal of Optics* 18 (2016).

[5] R.F. Oulton, V.J. Sorger, D.A. Genov, D.F.P. Pile, and X. Zhang. "A hybrid plasmonic waveguide for subwavelength confinement and long-range propagation". In: *Nature Photonics* 2 (2008), pp. 496–500.

[6] Mark I. Stockman. "Nanofocusing of optical energy in tapered plasmonic waveguides". In: *Physical Review Letters* 93.13 (2004).

[7] Daoxin Dai and Sailing He. "A silicon-based hybrid plasmonic waveguide with a metal cap for a nano-scale light confinement". In: *Optics Express* 17.19 (2009), pp. 16646–16653.

[8] Ren-Min Ma, Xiaobo Yin, Rupert F. Oulton, Volker J. Sorger, and Xiang Zhang. "Multiplexed and electrically modulated plasmon laser circuit". In: *Nanoletters* 12 (2012), pp. 5396–5402.

[9] Jacob S. Levy, Alexander Gondarenko, Mark A. Foster, Amy C. Turner-Foster, Alexander L. Gaeta, and Michal Lipson. "CMOS-compatible multiple-wavelength oscillator for on-chip optical interconnects". In: *Nature Photonics* 4 (2009), pp. 37–40.

[10] Ming Liu, Xiaobo Yin, Erick Ulin-Avila, Baisong Geng, Thomas Zentgraf, Long Ju, Feng Wang, and Xiang Zhang. "A graphene-based broadband optical modulator". In: *Nature* 474 (2011), pp. 64–68.

[11] Qianfan Xu, Bradley Schmidt, Sameer Pradhan, and Michal Lipson. "Micrometre-scale silicon electro-optic modulator". In: *Nature* 435 (2005), pp. 325–327.

[12] Lian-Wee Luo, Noam Ophir, Christine P. Chen, Lucas H. Gabrielli, Carl B. Poitras, Keren Bergmen, and Michal Lipson. "WDM-compatible mode-division multiplexing on a silicon chip". In: *Nature Communications* 5 (2014).

[13] Daoxin Dai, Jian Wang, and Yaocheng Shi. "Silicon mode (de)multiplexer enabling high capacity photonic networks-on-chip with a single-wavelength-carrier light". In: *Optics Letters* 38.9 (2013), pp. 1422–1424.

[14] Yunhong Ding, Jing Xu, Francesco Da Ros, Bo Huang, Haiyan Ou, and Christophe Peucheret. "On-chip two-mode division multiplexing using tapered directional coupler-based mode multiplexer and demultiplexer". In: *Optics Express* 21.8 (2013), pp. 10376–10382.

[15] Serdar Kocaman, Mehmet S. Aras, Nicolae C. Panoiu, Ming Lu, and Chee Wei Wong. "On-chip optical filters with designable characteristics based on an interferometer with embedded silicon photonic structures". In: *Optics Letters* 37.4 (2012), pp. 665–667.

[16] Eugene Hecht, ed. *Optical Properties of Solids*. New York: Oxford University Press, 2002.

[17] John Weiner and Frederico Nunes. *Light-Matter Interaction*. New York: Oxford University Press, 2017.

[18] Mark Fox, ed. *Optical Properties of Solids*. San Francisco: Addison Wesley, 2001.

[19] V. G. Veselago. "The electromagnetics of substances with simultaneously negative ϵ and μ". In: *Soviet Physics Uspekhi* 10.509 (1968).

[20] A.V. Kildishev, W.S. Cai, U.K. Chettier, J.K. Yuan, A.K. Sarychev, V.P. Drachev, and V.M. Shalaev. "Negative refractive index in optics of metal-dielectric composites". In: *Journal of the Optical Society of America B* 23 (2006), p. 423.

[21] R.A. Shelby, D.R. Smith, and S. Schultz. "Experimental verification of a negative index of refraction". In: *Science* 292.77 (2001).

[22] J. Valentine, S. Zhang, T. Zentgraf, E. Ulin-Avila, D.A. Genov, G. Bartal, and X. Zhang. "Three-dimensional optical metamaterial with a negative refractive index". In: *Nature* 455 (2008), pp. 376–380.

[23] J.B. Pendry. "Negative refraction makes a perfect lens". In: *Physical Review Letters* 85.3966 (2000).

[24] N. Fang, H. Lee, C. Sun, and X. Zhang. "Sub-diffraction-limited optical imaging with a silver superlens". In: *Science* 308.534 (2005).

[25] Z. Liu, H. Lee, Y. Xiong, C. Sun, and X. Zhang. "Far-field optical hyperlens magnifying sub-diffraction-limited objects". In: *Science* 313 (2007), p. 1686.

[26] J. B. Pendry, D. Schurig, and D. R. Smith. "Controlling Electromagnetic Fields". In: *Science* 312.5781 (2006), pp. 1780–1782.

[27] Huanyang Chen, C. T. Chan, and Ping Sheng. "Transformation Optics and Metamaterials". In: *Nature Materials* 9 (2010), pp. 387–396.

[28] A.J. Ward and J.B. Pendry. "Refraction and geometry in Maxwell's equations". In: *Journal of Modern Optics* 43.4 (1996).

[29] J.B Pendry, Yu Luo, and Rongkuo Zhao. "Transforming the optical landscape". In: *Science* 348.6234 (2015), pp. 521–524.

[30] D. Schurig, J.J. Mock, B.J. Justice, S.A. Cummer, A.F. Starr, and D.R. Smith. "Metamaterial electromagnetic cloak at microwave frequencies". In: *Science* 314.5801 (2006), pp. 977–980.

[31] Wenshan Cai, Uday K. Chettiar, Alexander V. Kildishev, and Vladimir M. Shalaev. "Optical cloaking with metamaterials". In: *Nature Photonics* 1 (2007), pp. 224–227.

[32] Lin Xu and Huanyang Chen. "Conformal transformation optics". In: *Nature Photonics* 9 (2015), pp. 15–23.

[33] Ulf Leonhardt. "Optical conformal mapping". In: *Science* 312.5781 (2006), pp. 1777–1780.

[34] J.B. Pendry, A.I Fernandez-Dominguez, Yu Luo, and Rongkuo Zhao. "Capturing photons with transformation optics". In: *Nature Physics* 9 (2013), pp. 518–522.

[35] Jensen Li and J.B. Pendry. "Hiding under the carpet: A new strategy for cloaking". In: *Physical Review Letters* 101.20 (2008).

[36] Jason Valentine, Jensen Li, Thomas Zentgraf, Guy Bartal, and Xiang Zhang. "An optical cloak made of dielectrics". In: *Nature Materials* 8 (2009), pp. 568–571.

[37] Majid Gharghi, Christopher Gladden, Thomas Zentgraph, Yongmin Liu, Xiaobo Yin, Jason Valentine, and Xiang Zhang. "A carpet cloak for visible light". In: *Nanoletters* 11.7 (2011), pp. 2825–2828.

[38] T. Ergin, N. Stenger, P. Brenner, J.B. Pendry, and M. Wegener. "Three-dimensional invisibility cloak at optical wavelengths". In: *Science* 328.5976 (2010), pp. 337–339.

[39] Joachim Fischer, Tolga Ergin, and Martin Wegener. "Three-dimensional polarization-independent visible-frequency carpet invisibility cloak". In: *Optics Letters* 36.11 (2011), pp. 2059–2061.

[40] T. Zentgraf, J. Valentine, N. Tapia, J. Li, and X. Zhang. "An optical Janus device for integrated photonics". In: *Advanced Materials* 22.23 (2010), pp. 2561–2564.

[41] Nathan Kuntz and David R. Smith. "Extreme-angle broadband metamaterial lens". In: *Nature Materials* 9 (2010), pp. 129–132.

[42] John Hunt, Talmage Tyler, Sulochana Dhar, Yu-Ju Tsai, Patrick Bowen Stephane Larouche, Nan M. Jokerst, and David R. Smith. "Planar, flattened Luneburg lens at infrared wavelengths". In: *Optics Express* 20.2 (2012), pp. 1706–1713.

[43] R.V. Ramaswamy and R. Srivastava. "Ion-exchanged glass waveguides: a review". In: *Journal of Lightwave Technology* 6.6 (1988), pp. 984–1000.

[44] Lisa C. Klein, ed. *Sol-gel optics: processing and applications*. New York: Springer, 1994.

[45] K. Shingyouchi and S. Konishi. "Gradient-index doped silica rod lenses produced by a solgel method". In: *Applied Optics* 29.28 (1990), pp. 4061–4063.

[46] S.N. Houde-Walter and B.L. McIntyre. "Dependence of refractive index on silver concentration in gradient-index glass". In: *Journal of Non-Crystalline Solids* 2 (1989), pp. 316–322.

[47] A.C. Urness, K. Anderson, C. Ye, W.L. Wilson, and R.R. McLeod. "Arbitrary GRIN component fabrication in optically driven diffusive photopolymers". In: *Optics Express* 23.1 (1989), pp. 264–273.

[48] Ivan Divliansky, Theresa S. Mayer, Kito S. Holliday, and Vincent H. Crespi. "Fabrication of three-dimensional polymer photonic crystal structures using single diffraction element interference lithography". In: *Applied Physics Letters* 82.11 (2003).

[49] Joachim Fischer, Georg von Freymann, and Martin Wegener. "The materials challenge in diffraction-unlimited direct-laser-writing optical lithography". In: *Applied Physics Letters* 22 (2010), pp. 3578–3582.

[50] H. Foll, M. Christophersen, J. Carstensen, and G. Hasse. "Formation and application of porous silicon". In: *Materials Science and Engineering R* 280 (2002), pp. 1–49.

[51] S. Matthias, F. Muller, C. Jamois, R.B. Wehrspohn, and U. Gosele. "Large-area three-dimensional structuring by electrochemical etching and lithography". In: *Advanced Materials* 16.23-24 (2004), pp. 2166–2170.

[52] G.A. Niklasson, C.G. Granqvist, and O. Hunderi. "Effectie medium models for the optical properties of inhomogeneous materials". In: *Applied Optics* 20.1 (1981), pp. 26–30.

[53] V. Agarwal and J.A. del Rio. "Tailoring the photonic band gap of a porous silicon dielectric mirror". In: *Applied Physics Letters* 82.10 (2003).

[54] A. Loni, L.T. Canham, M.G. Berger, R. Arens-Fischer, H. Munder, H. Luth, H.F. Arrand, and T.M. Benson. "Porous silicon multilayer optical waveguides". In: *Thin Solid Films* 276.1-2 (1996), pp. 143–146.

[55] C. Mazzoleni and L. Pavesi. "Application to optical components of dielectric porous silicon multilayers". In: *Applied Physics Letters* 67.20 (1995).

[56] S. Ilyas and M. Gal. "Gradient refractive index planar microlens in Si using porous silicon". In: *Applied Physics Letters* 89.21 (2006).

[57] Neil A. Krueger, Aaron L. Holsteen, Seung-Kyun Kang, Christian R. Ocier, Weijun Zhao, Glennys Mensing, John A. Rogers, Mark L. Brongersma, and Paul V. Braun. "Porous silicon gradient refractive index micro-optics". In: *Nanoletters* 16 (2016), pp. 7402–7407.

[58] David S. Barth, Christopher Gladden, Alessandro Salandrino, Kevin O'Brien, Ziliang Ye, Michael Mrejen, Yuan Wang, and Xiang Zhang. "Macroscale transformation optics enabled by photoelectrochemical etching". In: *Advanced Materials* 27.40 (2015), pp. 6131–6136.

[59] Vincent V. Doan and Michael J. Sailor. "Luminescent color image generation on porous silicon". In: *Science* 256.5065 (1992), pp. 1791–1792.

[60] V. Lehmann. "Porous silicon formation and other photoelectrochemical effects at silicon electrodes anodized in hydrofluoric acid". In: *Applied Surface Science* 106 (1996), pp. 402–405.

[61] A.G. Cullis and L.T. Canham. "The structural and luminescence properties of porous silicon". In: *Journal of Applied Physics* 82.3 (1997), pp. 909–965.

[62] C.C. Striemer and P.M. Fauchet. "Dynamic etching of silicon for broadband antireflection applications". In: *Applied Physics Letters* 81.16 (2002), pp. 2980–2982.

[63] Sri Rama Prasanna Pavani, Michael A. Thompson, Julie S. Biteen, Samuel J. Lord, Na Liu, Robert J. Twieg, Rafael Piestun, and W.E. Moerner. "Three-dimensional, single-molecule fluorescence imaging beyond the diffraction limit by using a double-helix point spread function". In: *Proceedings of the National Academy of Sciences* 106.9 (2009), pp. 2995–2999.

[64] D. Gabor. "A new microscopic principle". In: *Nature* 4098 (1948), pp. 777–778.

[65] Shahid Raza and Sharad Sharma. "Holography: a review". In: *International Journal of Applied Physics and Mathematics* 2.3 (2012), pp. 184–186.

[66] Myung K. Kim. "Principles and techniques of digital holographic microscopy". In: *SPIE Reviews* 1 (2010).

[67] Patrice Genevet and Federico Capasso. "Holographic optical metasurfaces: a review of current progress". In: *Reports on Progress in Physics* 78 (2015).

[68] Jae Hun Seol, David Barth, Jia Zhu, Dusan Coso, Kedar Hippalgaonkar, Jongwoo Lim, Junkyu Han, Xiang Zhang, and Arun Majumdar. "Unusually large reduction of thermal conductivity in mesoporous silicon due to slight porosity increase". In: *Applied Physics Letters* (In Press).

[69] S.E. Foss, P.Y.Y. Kan, and T.G. Finstad. "Single beam determination of porosity and etch rate in situ during etching of porous silicon". In: *Journal of Applied Physics* 97.11 (2005).

[70] M. Thonissen, S. Billat, M. Kruger, H Luth, M.G. Berger, U. Frotscher, and U. Rossow. "Depth inhomogeneity of porous silicon layers". In: *Journal of Applied Physics* 80.5 (1996), pp. 2990–2993.

[71] David G. Cahill. "Thermal conductivity measurement from 30 to 750 K: the 3ω method". In: *Review of scientific instruments* 61.2 (1990), pp. 802–808.

[72] Cristian R. Ocier, Neil A. Krueger, Weijun Zhao, and Paul V. Braun. "Tunable visibly transparent optics derived from porous silicon". In: *ACS Photonics* 4 (2017), pp. 909–914.

[73] Erik Winfree, Furong Liu, Lisa A. Wenzler, and Nadrian C. Seeman. "Design and self-assembly of two-dimensional DNA crystals". In: *Nature* 394 (1998), pp. 539–544.

[74] Shawn M. Douglas, Hendrik Dietz, Tim Liedl, Bjorn Hogberg, Franziska Graf, and William M. Shih. "Self-assembly of DNA into nanoscale three-dimensional shapes". In: *Nature* 459 (2009), pp. 414–418.

[75] Zeyu Xiao, Changwei Ji, Jinjun Shi, Eric M. Prigden, Jillian Frieder, Jun Wu, and Omid C. Farokhzad. "DNA self-assembly of targeted near-infrared-responsive gold nanoparticles for cancer thermo-chemotherapy". In: *Angewandte Chemie* 124 (2012), pp. 12023–12027.

[76] Chengde Mao, Thomas H. LaBean, John H. Reif, and Nadrian C. Seeman. "Logical computation using algorithmic self-assembly of DNA triple-crossover molecules". In: *Nature* 407 (2000), pp. 493–496.

[77] Dongran Han, Suchetan Pal, Jeanette Nangreave, Zhengtao Deng, Yan Liu, and Hao Yan. "DNA origami with complex curvatures in three-dimensional space". In: *Science* 332 (2011), pp. 342–348.

[78] Hareem T. Maune, Si-ping Han, Robert D. Barish, Marc Bockrath, William A. Goddard III, Paul W.K. Rothemund, and Erik Winfree. "Self-assembly of carbon nanotubes into two-dimensional geometries using DNA origami templates". In: *Nature Nanotechnology* 5 (2009), pp. 61–67.

[79] Thomas Torring, Niels V. Voigt, Jeanette Nangreave, Hao Yan, and Kurt V. Gothelf. "DNA origami: a quantum leap for self-assembly of complex structures". In: *Chemical Society Reviews* 540 (2011), pp. 5636–65646.

[80] Joshua I. Cutler, Evelyn Auyeung, and Chad A. Mirkin. "Spherical nucleic acids". In: *Journal of the American Chemical Society* 134 (2012), pp. 1376–1391.

[81] Stephen Mann. "Life as a nanoscale phenomenon". In: *Angewandte Chemie* 47 (2008), pp. 5306–5320.

[82] Bartosz A. Grzybowski and Wilhelm T.S. Huck. "The nanotechnology of life-inspired systems". In: *Nature Nanotechnology* 11 (2016), pp. 585–592.

[83] Marcin Fialkowski, Kyle J.M. Bishop, Rafal Klajn, Stoyan K. Smoukov, Christopher J. Campbell, and Bartosz A. Grzybowski. "Principles and implementations of dissipative (dynamic) self-assembly". In: *Journal of Physical Chemistry B* 110 (2006), pp. 2482–2496.

[84] Jeremy L. England. "Dissipative adaptation in driven self-assembly". In: *Nature Nanotechnology* 16.10 (2015), pp. 919–923.

[85] R. Dean Astumian. "Microscopic reversibility as the organizing principle of molecular machines". In: *Nature Nanotechnology* 7 (2012), pp. 684–689.

[86] Elio Mattia and Sijbren Otto. "Supramolecular systems chemistry". In: *Nature Nanotechnology* 10 (2015), pp. 111–120.

[87] Bartosz A. Grzybowski, Howard A. Stone, and George M. Whitesides. "Dynamic self-assembly of magnetized, millimetre-sized objects rotating at a liquid-air interface". In: *Nature* 405 (2000), pp. 1033–1036.

[88] Siowling Soh, Kyle J.M. Bishop, and Bartosz A. Grzybowski. "Dynamic self-assembly in ensembles of camphor boats". In: *Journal of Physical Chemistry B* 112 (2008), pp. 10848–10853.

[89] Nicolas Bachelard, Chad Ropp, Marc Dubois, Rongkuo Zhao, Yuan Wang, and Xiang Zhang. "Emergence of an enslaved phononic bandgap in a non-equilibrium pseudocrystal". In: *Nature Materials* 16 (2017), pp. 808–813.

[90] Serge M. Melle, A. Tino Alavie, Shawn Karr, Trent Coroy, Kexing Liu, and Raymond M. Measures. "A Bragg grating-tuned fiber laser strain sensor system". In: *IEEE Photonics Technology Letters* 5.2 (1993), pp. 263–266.

[91] Sung-Sik Yun and Jong-Hyun Lee. "A micromachined in-plane tunable optical filter using the thermo-optic effect of crystalline silicon". In: *Journal of Micromechanics and Microengineering* 13 (2003), pp. 721–725.

[92] V. Mulloni and L. Pavesi. "Porous silicon microcavities as optical chemical sensors". In: *Applied Physics Letters* 76.18 (2000), pp. 2523–2525.

[93] Ilaria Rea, Mario Iodice, Giuseppe Coppola, Ivo Rendina, Antigone Marino, and Luca De Stefano. "A porous silicon-based Bragg grating waveguide sensor for chemical monitoring". In: *Sensors and Actuators B* 139 (2008), pp. 39–43.

[94] Han-Jung Kim, Yong-You Kim, Ki-Won Lee, and Seon-Hwa Park. "A distributed Bragg reflector porous silicon layer for optical interferometric sensing of organic vapor". In: *Sensors and Actuators B* 155 (2011), pp. 673–678.

[95] Victor S.-Y. Lin, Kianoush Motesharei, Keiki-Pua S. Dancil, Michael J. Sailor, and M. Reza Ghadiri. "A porous silicon-based optical interferometric biosensor". In: *Science* 278 (1997), pp. 840–843.

[96] Erez Hasman, Gabriel Biener, Avi Niv, and Vladimir Kleiner. "Space-variant polarization manipulation". In: *Progress in Optics* 47 (2005), pp. 215–289.

[97] Nanfang Yu and Federico Capasso. "Flat optics with designer metasurfaces". In: *Nature Materials* 13 (2014), pp. 139–150.

[98] Dianmin Lin, Pengyu Fan, Erez Hasman, and Mark L. Brongersma. "Dielectric gradient metasurface optical elements". In: *Science* 345.6194 (2014), pp. 298–302.

[99] Ebrahim Karimi, Sebastian A. Schulz, Israel De Leon, Hamman Qassim, Jeremy Upham, and Robert W. Boyd. "Generating optical orbital angular momentum at visible wavelengths using a plasmonic metasurface". In: *Light: Science and Applications* 3 (2014).

[100] Nanfang Yu, Patrice Genevet, Mikhail A. Kats, Francesco Aieta, Jean-Philippe Tetienne, Federico Capasso, and Zeno Gaburro. "Light propagation with phase discontinuities: generalized laws of reflection and refraction". In: *Science* 334.6054 (2011), pp. 333–337.

[101] Xingjie Ni, Zi Jing Wong, Michael Mrejen, Yuan Wang, and Xiang Zhang. "An ultrathin invisibility skin cloak for visible light". In: *Science* 349.6254 (2015), pp. 1310–1314.

[102] Guoxing Zheng, Holger Muhlenbernd, Mitchell Kenney, Guixin Li, and Thomas Zentgraf. "Metasurface holograms reaching 80% efficiency". In: *Nature Nanotechnology* 10 (2015), pp. 308–312.

[103] Weimin Ye, Franziska Zeuner, Xin Li, Bernhard Reineke, Shan He, Cheng-Wei Qiu, Juan Liu, Yongtian Wang, Shuang Zhang, and Thomas Zentgraf. "Spin and wavelength multiplexed nonlinear metasurface holography". In: *Nature Communications* 7 (2016).

[104] Luyao Xu, Christopher A. Curwen, Philip W.C. Hon, Qi-Sheng Chen, Tatasuo Itoh, and Benjamin S. Williams. "Metasurface external cavity laser". In: *Applied Physics Letters* 107.22 (2015).

[105] Didier Felbacq. "Weak and strong coupling of a quantum emitter with a metasurface". In: *Superlattices and Microstructures* 78 (2015), pp. 79–87.

[106] Shumei Chen, Guixin Li, Franziska Zeuner, Wing Han Wong, Edwin Yue Bun Pun, Thomas Zentgraf, Kok Wai Cheah, and Shuang Zhang. "Symmetry-selective third-harmonic generation from plasmonic metacrystals". In: *Physical Review Letters* 113.3 (2014).

[107] Guixin Li, Shuang Zhang, and Thomas Zentgraf. "Nonlinear photonic metasurfaces". In: *Nature Reviews* 2 (2017).

[108] Nishant Nookala, Jongwan Le, Mykhailo Tymchenko, J. Sebastian Gomez-Diaz, Frederic Demmerle, Gerhard Boehm, Kueifu Lai, Gennady Shvets, Marcus-Christian Amann, Andrea Alu, and Mikhail Belkin. "Ultrathin gradient nonlinear metasurface with a giant nonlinear response". In: *Optica* 3.3 (2016), pp. 283–288.

[109] J. Lee, C. Argyropoulos, P.-Y. Chen, M. Tymchenko, F. Lu, F. Demmerle, G. Boehm, M.-C. Amann, A. Alu, and M.A. Belkin. "Giant nonlinear response from plasmonic metasurfaces coupled to intersubband transitions". In: *CLEO* (2014).

[110] Guixin Li, Shumei Chen, Nitipat Pholchai, Bernhard Reineke, Polis Wing Han Wong, Edwin Yue Bun Pun, Kok Wai Cheah, Thomas Zentgraf, and Shuang Zhang. "Continuous control of the nonlinear phase for harmonic generations". In: *Nature Materials* 14 (2015), pp. 607–612.

[111] Wenjiang Nie. "Optical nonlinearity: phenomena, applications, and materials". In: *Advanced Materials* 5.7-8 (1993), pp. 520–545.

[112] Zin Lin, Hamidreza Ramezani, Toni Eichelkraut, Tsampikos Kottos, Hui Cao, and Demetrios N. Christodoulides. "Unidirectional invisibility induced by PT-symmetric periodic structure". In: *Physical Review Letters* 106 (2011).

[113] F. Nazari, N. Bender, H. Ramezani, M.K. Moravvej-Farshi, D.N. Christodoulides, and T. Kottos. "Optical isolation via PT-symmetric nonlinear Fano resonances". In: *Optics Express* 22.8 (2014).

[114] Lei Bi, Juejun Hu, Peng Jiang, Dong Hun Kim, Gerald F. Dionne, Lionel C. Kimerling, and C.A. Ross. "On-chip optical isolation in monolithically integrated non-reciprocal optical resonators". In: *Nature Photonics* 5 (2011), pp. 758–762.

[115] Andrey E. Miroshnickenko, Etienne Brasselet, and Yuri S. Kivshar. "Reversible optical nonreciprocity in periodic structures with liquid crystals". In: *Applied Physics Letters* 96.6 (2010).

[116] Yannis Kominis, Tassos Bountis, and Sergej Flach. "The asymmetric active coupler: stable nonlinear supermodes and directed transport". In: *Scientific Reports* 6 (2016).

[117] N. Bender, S. Factor, J.D. Bodyfelt, H. Ramezani, D.N. Christodoulides, F.M. Ellis, and T. Kottos. "Observation of asymmetric transport in structures with active nonlinearities". In: *Physical Review Letters* 110.23 (2013).

[118] Li Fan, Jian Wang, Leo T. Varghese, Hao Shen, Ben Niu, Yi Xuan, Andrew M. Weiner, and Minghao Qi. "An all-optical silicon passive optical diode". In: *Science* 335.6067 (2012), pp. 447–450.

[119] B. Liang, X.S. Guo, J. Tu, D. Zhang, and J.C. Cheng. "An acoustic rectifier". In: *Nature Materials* 9 (2010), pp. 989–993.

[120] Noah D. Bronstein, Yuan Yao, Lu Xu, Erin O'Brien, Alexander S. Powers, Vivian E. Ferry, A. Paul Alivisatos, and Ralph G. Nuzzo. "Quantum dot luminescent concentrator cavity exhibiting 30-fold concentration". In: *ACS Photonics* 2 (2015), pp. 1576–1583.

[121] Young-Shin Park, Shaojun Guo, Nikolay S. Makarov, and Victor I. Klimov. "Room temperature single-photon emission from individual perovskite quantum dots". In: *ACS Nano* 9.10 (2015), pp. 10386–10393.

[122] Yuxi Tian, Aboma Merdasa, Eva Unger, Mohamed Abdellah, Kaibo Zheng, Sarah McKibbin, Anders Mikkelsen, Tonu Pullerits, Arkady Yartsev, Villy Sundstrom, and Ivan G. Scheblykin. "Enhanced organo-metal halide perovskite photoluminescence from nanosized defect-free crystallites and emitting sites". In: *Journal of Physical Chemistry Letters* 6 (2015), pp. 4171–4177.

[123] Fengrui Hu, Huichao Zhang, Chun Sun, Chunyang Yin, Bihu Lv, Chunfeng Zhang, William W. Yu, Xiaoyong Wang, Yu Zhang, and Min Xiao. "Superior optical properties of perovskite nanocrystals as single photon emitters". In: *ACS Nano* 9.12 (2015), pp. 12410–12416.

[124] James M. Ball, Michael M. Lee, Andrew Hey, and Henry J. Snaith. "Low-temperature processed meso-superstructured to thin-film perovskite solar cells". In: *Energy and Environmental Science* 6 (2013), pp. 1739–1743.

[125] Haiming Zhu, Yongping Fu, Fei Meng, Xiaoxi Wu, Zizhou Gong, Qi Ding, Martin V. Gustafsson, M. Tuan Trinh, Song Jin, and X-Y. Zhu. "Lead halide perovskite nanowire lasers with low lasing thresholds and high quality factors". In: *Naure Materials* 14 (2015), pp. 636–643.

[126] Igor L. Medintz, H. Tetsuo Uyeda, Ellen R. Goldman, and Hedi Mattoussi. "Quantum dot bioconjugates for imaging, labelling and sensing". In: *Nature Materials* 4 (2005), pp. 435–446.

[127] Yasuhiro Shirasaki, Geoffrey J. Supran, Moungi G. Bawendi, and Vladimir Bulovic. "Emergence of colloidal quantum-dot light-emitting technologies". In: *Nature Photonics* 7 (2012), pp. 13–23.

[128] Harald Giessen and Markus Lippitz. "Directing light emission from quantum dots". In: *Science* 329.5994 (2010), pp. 910–911.

[129] Bryan Ellis, Marie A. Mayer, Gary Shambat, Tomas Sarmiento, James Harris, Eugene E. Haller, and Jelena Vuckovic. "Ultralow-threshold electrically pumped quantum-dot photonic-crystal nanocavity laser". In: *Nature Photonics* 5 (2011), pp. 297–300.

[130] Hilmi Volkan Demir, Sedat Nizamoglu, Talhi Erdem, Evren Mutlugun, Nikkolai Gaponik, and Alexander Eychmuller. "Quantum dot integrated LEDs using photonic and excitonic color conversion". In: *Nano Today* 6 (2011), pp. 632–647.

[131] Kiyoshi Asakawa, Yoshimasa Sugimoto, Yoshinori Watanabe, Nobuhiko Ozaki, Akio Mizutani, Yoshiaki Takata, Yoshinori Kitagawa, Hiroshi Ishikawa, Naoki Ikeda, Koichi Awazu, Xiaoming Wang, Akira Watanabe, Shigeru Nakamura, Shunsuke Ohkouchi, Kuon Inoue, Martin Kristensen, Ole Sigmund, Peter Ingo Borel, and Roel Baets. "Photonic crystal and quantum dot technologies for all-optical switch and logic device". In: *New Journal of Physics* 8.208 (2006).

[132] Ethan D. Minot, Freek Kelkensberg, Maarten van Kouwen, Jorden A. van Dam, Leo P. Kouwenhoven, Valery Zwiller, Magnus T. Borgstrom, Olaf Wunnicke, Marcel A. Verheijen, and Erik P.A.M. Bakkers. "Single quantum dot nanowire LEDs". In: *Nanoletters* 7.2 (2007), pp. 367–371.

[133] Charles Santori, Matthew Pelton, Glenn Solomon, Yseulte Dale, and Yoshihisa Yamamoto. "Triggered single photons from a quantum dot". In: *Physical Review Letters* 86.8 (2001), pp. 1502–1505.

[134] Igor Aharonovich, Dirk Englund, and Milos Toth. "Solid-state single-photon emitters". In: *Nature Photonics* 10 (2016), pp. 631–641.

[135] Julien Claudon, Joel Bleuse, Nitin Singh Malik, Maela Bazin, Perine Jaffrennou, Niels Gregersen, Christophe Sauvan, Philippe Lalanne, and Jean-Michel Gerard. "A highly efficient single-photon source based on a quantum dot in a photonic nanowire". In: *Nature Photonics* 4 (2010), pp. 174–177.

[136] Matthew Pelton, Charles Santori, Jelena Vuckovic, Bingyang Zhang, Glenn S. Solomon, Jocelyn Plant, and Yoshihisa Yamamoto. "Efficient source of single photons: a single quantum dot in a micropost cavity". In: *Physical Review Letters* 89.23 (2002).

[137] P. Michler, A. Imamoglu, M.D. Mason, P.J. Carson, G.F. Strouse, and S.K. Buratto. "Quantum correlation among photons from a single quantum dot at room temperature". In: *Nature* 406 (2000), pp. 968–971.

[138] Seth Coe-Sullivan. "Quantum dot developments". In: *Nature Photonics* 3 (2009), pp. 315–316.

[139] Gabriele Raino, Georgian Nedelcu, Loredana Protesescu, Maryna I. Bodnarchuk, Maksym V. Kovalenko, Rainer F. Mahrt, and Thilo Stoferle. "Single cesium lead halide perovskite nanocrystals at low temperature: fast single-photon emission, reduced blinking, and exciton fine structure". In: *ACS Nano* 10 (2016), pp. 2485–2490.

[140] Sonia Buckley, Kelley Rivoire, and Jelena Vuckovic. "Engineered quantum dot single photon sources". In: *Reports on Progress in Physics* 75 (2012).

[141] Brent A. Koscher, Joseph K. Swabeck, Noah D. Bronstein, and A. Paul Alivisatos. "Essentially trap-free $CsPbBr_3$ colloidal nanocrystals by postsynthetic thiocyanate surface treatment". In: *Journal of the American Chemical Society* 139 (2017), pp. 6566–6569.

[142] Ou Chen, Jing Zhao, Vikash P. Chauham, Jian Cui, Cliff Wong, Daniel K. Harris, He Wei, Hee-Sun Han, Dai Fukumura, Rakesh K. Jain, and Moungi G. Bawendi. "Compact high-quality CdSe-CdS core-shell nanocrystals with narrow emission linewidths and suppressed blinking". In: *Nature Materials* 12 (2013), pp. 445–451.

[143] Alexey V. Kavokin, Jeremy J. Baumberg, Guillaume Malpuech, and Fabrice P. Laussy. *Microcavities*. New York: Oxford University Press, 2011.

[144] V.S.C Manga Rao and S. Hughes. "Single quantum-dot Purcell factor and β factor in a photonic crystal waveguide". In: *Physical Review B* 75.20 (2007).

[145] Alberto G. Curto, Giorgio Volpe, Tim H. Taminiau, Mark P. Kreuzer, Romain Quidant, and Niek F. van Hulst. "Unidirectional emission of a quantum dot coupled to a nanoantenna". In: *Science* 329.5994 (2010), pp. 930–933.

[146] Jingjing Li, Alessandro Salandrino, and Nader Engheta. "Shaping light beams in the nanometer scale: a Yagi-Uda nanoantenna in the optical domain". In: *Physical Review B* 76.24 (2007).

[147] Weiqiang Xie, Yunpeng Zhu, Tangi Aubert, Steven Verstuyft, Zeger Hens, and Dries Van Thourhout. "Low-loss silicon nitride waveguide hybridly integrated with colloidal quantum dots". In: *Optics Express* 23.9 (2015).

[148] Andre Schwagmann, Sokratis Kalliakos, Ian Farrer, Jonathan P. Griffiths, Geb A.C. Jones, David A. Ritchie, and Andrew J. Shields. "On-chip single photon emission from an integrated semiconductor quantum dot into a photonic crystal waveguide". In: *Applied Physics Letters* 99 (2011).

[149] T. Yoshie, A. Scherer, J. Hendrickson, G. Khitrova, H.M. Gibbs, G. Rupper, C. Ell, O.B. Shchekin, and D.G. Deppe. "Vacuum Rabi splitting with a single quantum dot in a photonic crystal nanocavity". In: *Nature* 432 (2004), pp. 200–203.

[150] Dirk Englund, Arka Majumdar, Andrei Faraon, Mitsuru Toishi, Nick Stoltz, Pierre Petroff, and Jelena Vuckovic. "Resonant excitation of a quantum dot strongly coupled to a photonic crystal nanocavity". In: *Nature* 432 (2004), pp. 200–203.

[151] Peter Lodahl, A. Floris van Driel, Ivan S. Nikolaev, Arie Irman, Karin Overgaag, Daniel Vanmaekelbergh, and Willem L. Vos. "Controlling the dynamics of spontaneous emission from quantum dots by photonic crystals". In: *Nature* 430 (2004), pp. 654–657.

[152] Lukas Novotny and Niek van Hulst. "Antennas for light". In: *Nature Photonics* 5 (2011), pp. 83–90.